

VARIATIONAL ADIABATIC HYPERSPHERICAL  
TREATMENT OF FEW AND MANY PARTICLES

by

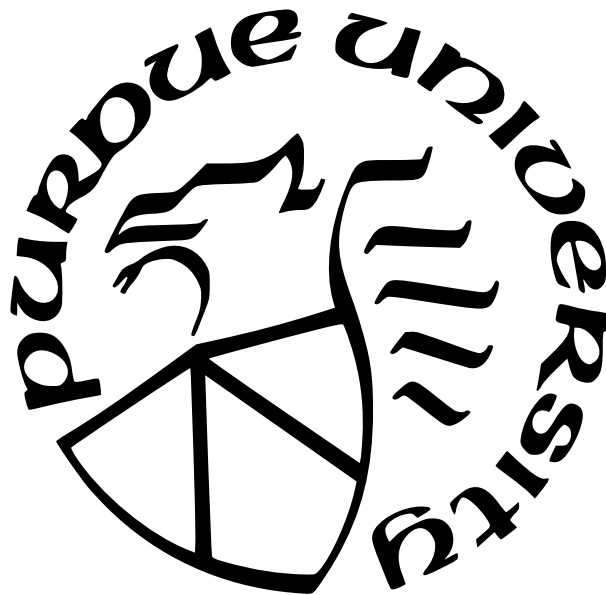
Hyunwoo Lee

A Dissertation

*Submitted to the Faculty of Purdue University*

*In Partial Fulfillment of the Requirements for the degree of*

Doctor of Philosophy



Department of Physics and Astronomy

West Lafayette, Indiana

December 2021

**THE PURDUE UNIVERSITY GRADUATE SCHOOL  
STATEMENT OF COMMITTEE APPROVAL**

**Dr. Chris H. Greene, Chair**

Department of Physics and Astronomy

**Dr. Chen-Lung Hung**

Department of Physics and Astronomy

**Dr. Francis Robicheaux**

Department of Physics and Astronomy

**Dr. Andrew Weiner**

School of Electrical and Computer Engineering

**Approved by:**

Dr. Gabor A. Csathy

He told them another parable: “The kingdom of heaven is like a mustard seed, which a man took and planted in his field. Though it is the smallest of all your seeds, yet when it grows, it is the largest of garden plants and becomes a tree, so that the birds of the air come and perch in its branches.”

Matthew 13:31-32

## ACKNOWLEDGMENTS

Many, many people and organizations made this work possible, too numerous for me to name them all (forgive me if I left you out). I thank Purdue University and the National Science Foundation for funding my work. I acknowledge all former and current members of the Greene and Robicheaux groups I've interacted with: in particular, I thank Matt Eiles, Panos Giannakeas, and Michael Higgins for the numerous enlightening discussions, help with calculations, and overall mentorship. I thank Doerte Blume for stimulating discussions about the Monte Carlo problem in the context of hyperspherical calculations, and I thank Jose D'Incao for sending me helpful data.

I thank the committee members, Prof. Hung, Prof. Robicheaux, and Prof. Weiner for their willingness to examine my work. I particularly thank Prof. Robicheaux for the many times he rescued me whenever I suffered from difficult numerical pathologies. And, of course, I am so very, very thankful to Prof. Greene, not only for his guidance through the tricky landscape of atomic physics I knew almost nothing about initially, but also for his incredible patience as I navigated through a bout of cancer early on, a coronavirus pandemic near the end, and two episodes of failed research projects in between. He trusted me and encouraged me to keep going.

Of course, my heart goes to my family, who gave me much-needed emotional refuge these last 6 years.

I dedicate this work to all other graduate students who had rough times. Just don't give up.

# TABLE OF CONTENTS

LIST OF TABLES . . . . .	7
LIST OF FIGURES . . . . .	8
ABSTRACT . . . . .	12
1 INTRODUCTION TO VARIATIONAL HYPERSPHERICAL FORMALISM . . .	13
1.1 Summary of Works in this Dissertation . . . . .	13
1.2 Review of Two-Body Physics . . . . .	14
2 ONE-BODY ANSATZ: INTRODUCTION AND METHOD . . . . .	20
2.1 Introduction to Physics of Many Bosons and Mean-Field Theory . . . . .	20
2.2 Method of One-Body Ansatz: Orbital Picture . . . . .	24
2.2.1 $N$ -Body Hamiltonian . . . . .	24
2.2.2 Choice of Independent-Particle Ansatz . . . . .	26
2.2.3 Extended Ansatz of Several Orbitals . . . . .	28
2.2.4 Dealing with Linear Dependence of Similar Orbitals . . . . .	31
2.3 Hyperangular Integration: Contour Deformation . . . . .	32
2.3.1 Matrix Elements as 1-D Complex Integrals . . . . .	32
2.3.2 Integration by Steepest Descent . . . . .	34
3 ONE-BODY ANSATZ: RESULTS AND DISCUSSION . . . . .	40
3.1 Potentials of Single Mean-Field Orbitals . . . . .	40
3.2 Excitation Frequencies from Single Mean-Field Orbitals . . . . .	44
3.3 Multi-Orbital Calculations, Repulsive Interaction . . . . .	47
3.4 Multi-Orbital Calculations, Attractive Interaction . . . . .	49
3.5 Summary and Outlook . . . . .	54
4 TWO-BODY ANSATZ: INTRODUCTION AND METHOD . . . . .	56
4.1 Introduction to Physics of Few Bosons . . . . .	56
4.2 Method of Two-Body Ansatz . . . . .	60

4.2.1	$N$ -Body Hamiltonian with Center-of-Mass Removed . . . . .	60
4.2.2	$J^\pi = 0^+$ Symmetrized Hyperspherical Harmonics . . . . .	63
4.2.3	Construction of Explicit Two-Body Ansatz . . . . .	65
4.2.4	Analysis of Two-Body Ansatz . . . . .	68
4.3	Direct Hyperangular Integration . . . . .	72
4.3.1	Product and Sum Symmetrization for $N = 3$ . . . . .	72
4.3.2	Sum Symmetrization for $N > 3$ . . . . .	74
	Two-Body Terms . . . . .	79
	Three-Body Terms . . . . .	80
	Four-Body Terms . . . . .	81
	Many-Body Terms . . . . .	82
5	TWO-BODY ANSATZ: RESULTS AND DISCUSSION . . . . .	83
5.1	Benchmark for $N = 3$ . . . . .	83
5.2	Potential Curves for $N > 3$ . . . . .	87
5.3	Comparison of Potentials for $N = 4$ . . . . .	90
5.4	Asymptotic Potentials of Unitary Bosons . . . . .	94
5.5	Summary and Outlook . . . . .	96
	REFERENCES . . . . .	98
A	JACOBI VECTORS OF $N$ PARTICLES . . . . .	110
B	DELVES HYPERANGLES . . . . .	113
C	SMITH-WHITTEN HYPERANGLES . . . . .	115
	C.1 Three Particles . . . . .	115
	C.2 More than Three Particles . . . . .	118
D	THREE-BODY HYPERSPHERICAL HARMONICS . . . . .	121
E	EVALUATION OF TWO-BODY ANSATZ . . . . .	123
	VITA . . . . .	126

## LIST OF TABLES

- 3.1 List of ground state  $E_0$  and excitation  $\Delta E$  (units of  $\hbar\omega$ ) from solving Eq. 2.11 with different  $U(R) - \frac{Q(R)}{2N}$ , for  $N = 10^4$  and  $a_s = 10^{-2} l_t$ .  $n$  is the number of coupled orbitals, and  $\delta = n - c$  is the number of eigenstates of  $\underline{Q}$  thrown away. The orbitals  $\phi_{N_0, a_s}$  are identified by values of  $N_0 = N_{0,1} + (i-1)\Delta N_0$ ,  $i = 1, \dots, n$ . 48
- D.1 Summary of Symmetrized Hyperspherical Harmonics for  $N = 3$ ,  $J^\pi = 0^+$ . . . . 122

## LIST OF FIGURES

1.1	Demonstration of negative and positive scattering lengths using gaussian potential $V(r) = \frac{\hbar^2}{mr_0^2}\alpha \exp\left(-\left(\frac{r}{r_0}\right)^2\right)$ . . . . .	16
1.2	Schematics of a Feshbach resonance. Image taken from [8]. . . . .	18
2.1	Comparison of different spherically symmetric solutions of mean-field equation and their approximations. . . . .	21
2.2	Typical values of imaginary part $\kappa_0$ of saddle point. . . . .	36
2.3	Typical values of $f(k) = -ikR^2 + \log I(k)$ , $\beta = N$ , at saddle point $k = i\kappa_0$ . . . . .	37
2.4	Example of hyperradial logarithmic derivative of normalization integral $\frac{C'(R)}{NC(R)}$ . . . . .	38
3.1	Adiabatic potentials with $Q$ included for $a_s = 0.01 l_t$ , calculated using $\phi^{GP}$ for $N = 9600$ (blue dashed), 9800 (red dotted), and 10000 (green solid). The black circles are the K-Harmonic potential for $N = 9600$ . . . . .	41
3.2	Numerically minimized mean-field energy $E_0(N)$ (black circles) compared with the minima of adiabatic potentials ( $Q$ included) calculated using $\phi^{GP}$ (blue solid) and using the K-Harmonic approximation (red dashed), for $a_s = 0.01 l_t$ . . . . .	42
3.3	Adiabatic potentials with $Q$ included for $a_s = -4.577 \times 10^{-4} l_t$ , calculated using $\phi^{GP}$ for $N = 1197$ (orange solid), 1227 (blue dotted), and 1257 (red dashed). The black circles are the K-Harmonic potential for $N = 1257$ . . . . .	43
3.4	Numerically minimized mean-field energy $E_0(N)$ (black circles) compared with the extrema of adiabatic potentials ( $Q$ included), for $a_s = -4.577 \times 10^{-4} l_t$ . Blue solid and dashed curves are minima and maxima from $\phi^{GP}$ . Orange dotted and dash-dotted curves are minima and maxima from K-Harmonic approximation. . . . .	44
3.5	The first 3 (red, blue, orange) excitation energies $E_i - E_0$ for $a_s = 0.01 l_t$ and varying $N$ . Solid, dotted, and dashed curves are the Bogoliubov predictions, while solid circles are from the K-Harmonic approximation. Open circles are the results of single- $\phi^{GP}$ calculations. . . . .	45
3.6	The first 3 (red, blue, orange) excitation energies $E_i - E_0$ for $a_s = -4.577 \times 10^{-4} l_t$ and varying $N$ . Dotted curves are the Bogoliubov predictions, while solid curves are from the K-Harmonic approximation. Circles are from single- $\phi^{GP}$ calculations. . . . .	46
3.7	Adiabatic potentials with $Q$ included for $10^4$ bosons with $a_s = 10^{-2} l_t$ . The orange triangles, black circles, and green squares are single $\phi_{N_0, a_s}$ results with $N_0 = 9600.04, 10^4$ , and 10399.96. The red solid curve is the lowest primitive eigenvalue from coupling 3 orbitals with $N_0 = 9800.02, 10^4$ , and 10199.98, with no eigenstate of $Q$ removed. The blue dashed curve is the lowest reduced eigenvalue from coupling 5 orbitals with $N_0 = 9600.04, 9800.02, \dots, 10399.96$ , with 1 eigenstate of $Q$ removed. . . . .	47

3.8	Adiabatic potentials with $Q$ included for $a_s = -4.577 \times 10^{-4} l_t$ and $N = 1220$ ; all are single-orbital results. Orange dashed, blue solid, and red dotted curves are from $\phi_{N_0, a_s}$ with $N_0 = 1112.41, 1220,$ and $1257.1$ . Purple squares, magenta triangles, and green circles are from $\phi_l^s$ with $l = 0.38, 0.43,$ and $0.64 l_t$ . . . . .	49
3.9	Adiabatic potentials with $Q$ included for $a_s = -4.577 \times 10^{-4} l_t$ and $N = 1300$ ; all are single-orbital results. Orange dashed, blue dotted, and red solid curves are from $\phi_{N_0, a_s}$ with $N_0 = 1149.27, 1203.19,$ and $1257.12$ . Magenta triangles, green circles, and purple squares are from $\phi_l^s$ with $l = 0.38, 0.43,$ and $0.48 l_t$ . . . . .	50
3.10	Adiabatic potentials for $N = 1257, a_s = -4.577 \times 10^{-4} l_t$ . Open brown circles and open blue triangles are $U$ with $Q$ included from single $\phi_{N_0, a_s}$ , with $N_0 = 1257$ and $1251.51$ . Red squares, purple filled circles, and orange filled triangles are $U$ with $Q$ included from single $\phi_l^s$ with $l = 0.39, 0.44,$ and $0.49 l_t$ . The 5 (green, red, blue, orange, and purple) dashed curves are the primitive generalized eigenvalues $U$ , <i>without</i> $Q$ , from coupling the above 5 orbitals. The dotted black curve <i>includes</i> $Q$ for the lowest eigenvalue. . . . .	51
3.11	Hyperradial eigenstates $F(R)$ for $N = 1257$ and $a_s = -4.577 \times 10^{-4} l_t$ from solving Eqn. 2.11. The potential, represented by black circles here, is the dotted black curve of Fig. 3.10. Boundary condition $F(R_c) = 0$ at $R_c = 0.75 l_t$ is chosen. Dotted lines denote the eigenenergies; solid and dashed curves are the corresponding wavefunctions $F(R)$ (scaled arbitrarily). Magenta denotes a collapsed state outside the minimum well; red denotes a metastable state, while green and orange denote rapidly decaying states. . . . .	53
4.1	Diagram of trimer binding energies, three-body continuum, and atom-dimer continuum thresholds in terms of inverse scattering length. Vertical axis is $\kappa = \text{sign}(E) \sqrt{\frac{m E }{\hbar^2}}$ . Figure taken from Ref. [70]. . . . .	57
4.2	Right-hand-sides of Eqns. 4.25 (solid) and 4.24 (dashed), as a function of $\tilde{\nu} = \nu + \frac{3N-5}{2} = \nu + 2$ , which is either positive real or positive imaginary. . . . .	69
4.3	$\epsilon = \tilde{\nu}^2 = \left(\nu + \frac{3N-5}{2}\right)^2$ and $C_m$ as functions of $\rho$ . . . . .	70
4.4	First and third $\phi_\nu(r_{1,2})$ at fixed $\rho$ . . . . .	71
4.5	$\frac{2Nm\rho^2}{\hbar^2} I_{3,4}$ for third sum-symmetrized ansatz $\phi_\nu$ . Blue curve computed using Sobol sequences, and red dots computed from Monte Carlo method. . . . .	77
4.6	5000 points (x,y) chosen randomly or from Sobol sequence. . . . .	78
5.1	Dimensionless coefficients of $\frac{\hbar^2}{2mN\rho^2}$ of the adiabatic potentials for 3 bosons, with soft-core Van der Waals interaction, $\sigma = 1.7180713 l_{vdw}$ , $a_s = -10 l_{vdw}$ . Black lines are from zero-range theory; blue lines are from B-spline diagonalization of $H_{ad}$ , courtesy of Yu-Hsin Chen. Red dots are from product symmetrization of $\phi_\nu$ with lowest value of $\nu$ ; brown dots are from sum symmetrization of $\phi_\nu$ with 3rd, 4th, and 5th values of $\nu$ . . . . .	83

5.2	Coefficient of $\frac{\hbar^2}{2mN\rho^2}$ of the lowest adiabatic potential for 3 bosons, with soft-core Van der Waals interaction, $\sigma = 1.7180713l_{vdw}$ , $a_s = -10l_{vdw}$ . Black dots are from zero-range theory; blue dots are from B-spline diagonalization of $H_{ad}$ , courtesy of Yu-Hsin Chen. Orange curve is from product symmetrization of $\phi_a$ . . . . .	84
5.3	Comparison between zero-range theory and product-symmetrized ansatz from different finite-range interactions for the coefficient of $\frac{\hbar^2}{2mN\rho^2}$ of the lowest hyperspherical potential, $N = 3$ , $a_s = -10,000l_{vdw}$ . . . . .	85
5.4	Comparison between zero-range theory and sum-symmetrized ansatz from different finite-range interactions for the coefficient of $\frac{\hbar^2}{2mN\rho^2}$ of the lowest hyperspherical potential, $N = 3$ , $a_s = -10,000l_{vdw}$ . . . . .	86
5.5	Variational adiabatic hyperspherical potentials for $N = 4$ , Van der Waals potential, $a_s = -300l_{vdw}$ . Dashed curves are non-interacting potentials with $\lambda = 0, 4, 6$ , and 8. . . . .	87
5.6	Lowest variational adiabatic hyperspherical potential for $N = 4$ , Van der Waals potential, $a_s = -300l_{vdw}$ . . . . .	88
5.7	Variational adiabatic hyperspherical potentials for $N = 10$ , Van der Waals potential, $a_s = -300l_{vdw}$ . Dashed curves are non-interacting potentials with $\lambda = 0, 4, 6$ , and 8. . . . .	89
5.8	Coefficient of $\frac{\hbar^2}{2mN\rho^2}$ of the lowest variational potential for $N = 4$ , for gaussian (blue) or soft-core Van der Waals (red) interaction with same $r_0 = l_{vdw}$ , with $a_s = -10,000l_{vdw}$ . Black dashed line is the non-interacting limit of 12. . . . .	90
5.9	Comparison of lowest 2 adiabatic potentials computed by correlated gaussian basis (solid color, diagonal $Q$ neglected, courtesy of M. Higgins) with sum symmetrized $\phi_\nu$ (dashed color), for $N = 4$ , using gaussian interaction with $a_s = -4r_0$ . Black dotted lines are non-interacting potentials with $\lambda = 0, 4$ . . . . .	91
5.10	Comparison of lowest adiabatic potential computed by correlated gaussian basis (solid, $Q$ neglected, courtesy of M. Higgins) with sum symmetrized $\phi_a$ (dashed), for $N = 4$ , using gaussian interaction with $a_s = -4r_0$ . . . . .	92
5.11	Comparison of lowest 2 adiabatic potentials computed by correlated gaussian basis (solid color, diagonal $Q$ neglected, courtesy of M. Higgins) with lowest sum symmetrized $\phi_\nu$ potential (dashed blue), for $N = 4$ , using gaussian interaction with $a_s = -5r_0$ . Black dotted line is non-interacting potential with $\lambda = 0$ . Black dashed line is the trimer threshold at $E = -0.01147\frac{\hbar^2}{mr_0^2}$ . . . . .	93
5.12	Asymptotic values of coefficients of $\frac{\hbar^2}{2mN\rho^2}$ for the lowest ansatz variational potential (red) near unitarity, compared with “mock” centrifugal non-interacting coefficient $\frac{(3N-4)(3N-6)}{4}$ (blue). . . . .	94
5.13	Difference between the two asymptotic coefficient values of Fig. 5.12, compared with a linear fit. . . . .	95

A.1	Illustration of the K-type and H-type Jacobi trees for 4 particles. . . . .	111
C.1	Illustration of the Euler angles $(\alpha, \beta, \gamma)$ . Taken from Figure 3.4 of Ref. [110]. . .	115
C.2	Illustration of Smith-Whitten coordinates $(\theta, \phi) = (0, 0)$ and $(\frac{\pi}{4}, 0)$ . . . . .	117

## ABSTRACT

This dissertation works out novel methodologies for approximately computing the adiabatic hyperspherical potential energies of more than 2 particles in terms of the variational principle. The first part uses the root-mean-square radius of a cloud of many atoms as a natural collective hyperradial coordinate, calculating the condensate energy by holding that radius fixed at discrete values. A new step beyond the constant-ansatz “K-Harmonic” approximation (in terms of orbital solutions of the mean-field equation) leads to great improvements in minimization of the ground condensate energy. Careful analysis using linear combinations of orbitals reveals a reduction in macroscopic potential barrier for attractive condensates as a partial description of many-body correlations in these ultracold atomic systems. The second part of this dissertation constructs a new ansatz that explicitly takes two-body correlation into account. Benchmark calculations are performed in comparison with well-known theory of Efimov physics for 3 bosons. New results on the variational potential energies of more than 3 bosons are obtained, revealing characteristic features of a deep minimum and a barrier at small values of hyperradii that are intimately connected to the lowest bound states of  $N$  bosons. Comparisons with numerical diagonalization for  $N = 4$  show that the variational potential accounts for the local minimum describing the lowest 4-body bound state but always diabatically converges to the scattering threshold (regardless of the presence of bound trimer thresholds). New results on the asymptotic behavior of unitary Bose gas are obtained for up to 10 particles.

# 1. INTRODUCTION TO VARIATIONAL HYPERSPHERICAL FORMALISM

## 1.1 Summary of Works in this Dissertation

This dissertation is concerned with the quantum behavior of identical bosons (with mostly cold atoms like Rb in mind) where the number of particles  $N$  varies as large as from 3 to 10,000. We formulate an alternative approach to the usual full diagonalization procedure found in the literature of adiabatic hyperspherical formalism, in which some hopefully suitable ansatz functions are found and variational calculations are performed in order to explore their consequences. The main aim is to extend the successes of adiabatic hyperspherical theory of 3 and 4 particles to more particles, for two different regimes: very large number of particles where comparisons with standard mean-field theory are possible, and modest number of particles where transition from few-body to many-body physics is expected but little is currently known.

The next part of this chapter summarizes key concepts of two-body physics that anyone who wishes to study the quantum problem of three or more particles must be familiar with. The rest of the dissertation is divided into two main parts. The first part, consisting of chapters 2 and 3, explores the problem of many-body physics of Bose-Einstein condensates by first reviewing the standard mean-field theory of Gross-Pitaevskii Equation and its key predictions, as well as important experimental observations. Then, staying within spherical symmetry, the root-mean-square radius  $R$  of the atomic cloud is taken to be an adiabatic parameter, the hyperradius of the problem. Potential energies  $U(R)$  of the collective system given each fixed  $R$  are computed by a one-body orbital type of ansatz inspired by mean-field theory. Various results on agreements and deviations between mean-field theory, variational hyperspherical calculations using orbitals, and previously known hyperspherical approximation scheme are developed.

The second part, made of chapters 4 and 5, explores more modest number of particles  $N$  from 3 to 10. As these chapters are more closely attuned to the few-body aspects of adiabatic hyperspherical formalism, important features of that few-body theory and milestone achievements, complemented by experimental results, will be reviewed first. Then, based

on what is already known in few-body physics, new kinds of ansatz functions that explicitly build in two-body correlations will be constructed. Methods regarding the required multi-dimensional integrals for variational calculations will be developed. Finally, results using the two-body ansatz will be discussed: both a series of benchmark with known results of few-body theory and some new predictions for more than 3 particles.

## 1.2 Review of Two-Body Physics

In order to develop and discuss a microscopic theory of more than 2 interacting particles, we must start with a review of the two-body formalism and introduce the concept of a pseudopotential, which is a useful tool for adding in the effect of two-body interactions into a theory involving more than 2 particles in an accessible manner. There are many excellent references that treat the quantum-mechanical two-body problem, bound and scattering (see for example Refs. [1] and [2]). Here we summarize some of the main relevant points.

For a spherically symmetric interaction in free space, one may treat the different partial waves separately by expanding  $\psi = \sum_{l,m} C_{l,m} \frac{u_{E,l}(r)}{r} Y_{l,m}(\theta, \phi)$  and solving the radial Schrödinger equation (for  $E > 0$ ,  $k = \sqrt{\frac{2\mu E}{\hbar^2}}$  with reduced mass  $\mu = \frac{m}{2}$ ):

$$-\frac{1}{2} \frac{d^2}{dr^2} u_{E,l}(r) + \left( V(r) + \frac{l(l+1)}{2r^2} \right) u_{E,l}(r) = \frac{1}{2} k^2 u_{E,l}(r). \quad (1.1)$$

The regular and irregular solutions for the case  $V = 0$  are the spherical Bessel functions:  $u_{E,l}^{(1)} = kr j_l(kr)$ ,  $u_{E,l}^{(2)} = kr n_l(kr)$ . Their asymptotic properties are as follows [3]:

$$(kr \gg l) u_{E,l}^{(1)} \rightarrow \sin\left(kr - \frac{l\pi}{2}\right), \quad u_{E,l}^{(2)} \rightarrow -\cos\left(kr - \frac{l\pi}{2}\right), \quad (1.2)$$

$$(kr \ll l) u_{E,l}^{(1)} \rightarrow \frac{(kr)^{l+1}}{(2l+1)!!} + \mathcal{O}((kr)^{l+3}), \quad u_{E,l}^{(2)} \rightarrow -\frac{(2l-1)!!}{(kr)^l} + \mathcal{O}((kr)^{-l+2}). \quad (1.3)$$

For a strictly finite-range potential with some range  $r_0$  ( $V(r \geq r_0) = 0$ ), the radial wave function at  $r \geq r_0$  takes the form  $u_{E,l} = C \left( u_{E,l}^{(1)} - \tan \delta_l u_{E,l}^{(2)} \right)$ . Once the radial Schrödinger equation is solved within the region of interaction, the phase shift  $\delta_l$  can be calculated by  $\tan \delta_l = \frac{W[u_{E,l}^{(1)}, u_{E,l}]}{W[u_{E,l}^{(2)}, u_{E,l}]}$  at  $r = r_0$ , where  $W[f, g] = fg' - f'g$  is the Wronskian. At low

energies, plugging in the small asymptotic forms of  $u^{(1)}, u^{(2)}$  into the expression for  $\tan \delta_l$ , one obtains the Wigner threshold laws:  $\tan \delta_l = k^{2l+1} (c_1 + c_2 k^2 + \dots)$ . Intuitively, this behavior originates from the centrifugal barrier  $\frac{l(l+1)}{2r^2}$  in the Schrödinger equation, so that at ultracold temperatures, s-wave scattering is the dominant contribution to the partial wave expansion (except in certain cases, such as spin-polarized fermions for which  $l = 0$  is forbidden by the Pauli exclusion principle). In particular, the s-wave scattering length is defined to be  $a_s = -\lim_{k \rightarrow 0} \frac{\tan \delta_0}{k}$  and is the most important parameter summarizing the strength of interparticle interaction in discussions of ultracold atomic gas; the scattering cross section is given by  $\sigma = 4\pi a_s^2$ , for instance.

The threshold laws hold as stated for any potential that falls off faster than any inverse power law, such as a Gaussian potential. They do not hold for the Coulomb potential, which requires a separate analysis using the Coulomb functions. A  $\frac{C}{r^2}$  potential is another anomaly; there exists a critical value of  $C$  at which the behavior of the wave function changes markedly, a subject that will be returned to later in discussions of the Efimov effect. For potentials  $\frac{1}{r^\alpha}$  with  $\alpha > 2$ , the threshold laws hold for  $l < \frac{\alpha-3}{2}$  and are replaced by  $k^{\alpha-2}$  for  $l > \frac{\alpha-3}{2}$  [2]. Therefore scattering length is well-defined for  $\alpha > 3$ .

Returning to finite-range potentials, notice that  $\frac{1}{k^{l+1}} u_{E,l}^{(1)}$ ,  $k^l u_{E,l}^{(2)}$ , and  $\frac{1}{k^{2l+1}} \tan \delta_l$  all are of order  $\mathcal{O}(k^0)$ . This allows us to analytically continue,  $k = i\kappa$ , to consider the bound spectrum. Examine  $u_{E,l} = \left(k^{l+1} C\right) \frac{1}{k^{l+1}} \left(u_{E,l}^{(1)} - \tan \delta_l u_{E,l}^{(2)}\right)$ , and recall that a bound state must not have asymptotic exponential divergence of form  $e^{\kappa r}$ . This gives a general energy-dependent condition for the bound state:  $i \tan \delta_l^0 = \frac{1}{k^{2l+1}}$  for an “energy-analytic” phase shift  $\tan \delta_l^0 = \frac{\tan \delta_l}{k^{2l+1}}$ . In particular, if there is a high-lying  $l = 0$  bound state very close to the threshold  $E = 0$ , its energy may be approximated by the *universal* dimer energy [4]:

$$E = -\frac{\hbar^2}{2\mu a_s^2}. \quad (1.4)$$

We emphasize the word “universal”, in that for *any* potential (regardless of whether it is an atomic, nuclear, or condensed-matter system), if it has finite range and the system is cold enough that the de Broglie wavelength vastly exceeds the range, this result is applicable.

Such universal regimes are where the inner details of the interaction are irrelevant, so that only the phase shift or, equivalently, the scattering length matters.

Let us examine this further. Note that at sufficiently low energy, the s-wave wave function outside the range of interaction becomes  $u_{E,0} = C \left( r + \frac{\tan \delta_0}{k} \right) = C(r - a_s)$ , or  $f = \frac{u}{r} = C \left( 1 - \frac{a_s}{r} \right)$ . In literature this is summarily represented by the Bethe-Peierls boundary condition [4]:  $\lim_{r \rightarrow 0} \frac{\partial}{\partial r} (rf) = \lim_{r \rightarrow 0} \frac{r^2}{a_s} \frac{\partial}{\partial r} f$ . Hence we get an intuitive interpretation for the scattering length: it is the zero-intercept of the radial wave function  $u_{E,0}$  at zero energy. Unitarity condition,  $a_s \rightarrow \pm\infty$ , is right where a dimer exists at threshold. A large, positive  $a_s$  indicates there is a weakly-bound dimer just below threshold, given by Eqn. 1.4; a large, negative  $a_s$ , on the other hand, indicates the dimer has been “pushed” above threshold and is no longer a bound state.

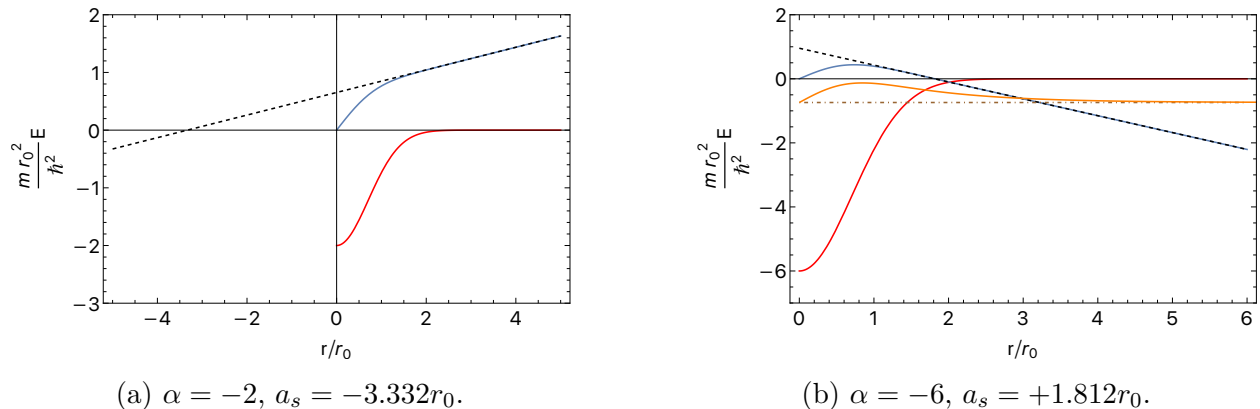


**Figure 1.1.** Demonstration of negative and positive scattering lengths using gaussian potential  $V(r) = \frac{\hbar^2}{mr_0^2} \alpha \exp \left( - \left( \frac{r}{r_0} \right)^2 \right)$ .

Fig. 1.1 shows an example of s-wave states calculated using a gaussian potential  $V(r) = \frac{\hbar^2}{mr_0^2} \alpha \exp \left( - \left( \frac{r}{r_0} \right)^2 \right)$ . When dimensionless  $\alpha = -2$ , the potential is too weak to support any dimer, and the scattering length is  $a_s = -3.332r_0$ , where the black dashed line crosses 0. Blue curve is the numerically solved zero-energy wave function. On the other hand, when  $\alpha = -6$ , there is one dimer at  $E = -0.74 \frac{\hbar^2}{mr_0^2}$ , while the black dashed line crosses 0 at  $a_s = 1.812r_0$ . Note that the zero-energy wave function (blue curve) and the bound-state

wave function (orange) look fairly similar when  $r < 2r_0$ . Eqn. 1.4 gives universal dimer energy  $E = -0.305 \frac{\hbar^2}{mr_0^2}$ , quite different from the correct binding energy because  $a_s$  is small.

Under the ultracold conditions we are interested in, the s-wave phase shift is, to a good approximation, all that matters in controlling the system physics, not the actual shape of the potential inside the range  $r_0$ . Therefore, assuming that the scattering length is known from experiment or theory, we replace the true interaction potential by the Fermi pseudopotential:

$$V(\vec{r}) = \frac{2\pi\hbar^2 a_s}{\mu} \delta(\vec{r}). \quad (1.5)$$

This pseudopotential was first derived by Fermi [5] in the context of the effect of surrounding neutral atoms (called *perturbers*) on the Rydberg spectra of alkali atoms, as a tool to describe the interaction between the highly excited electron and the perturbers. Substituted into the Schrödinger equation, the Fermi pseudopotential enforces the Bethe-Peierls boundary condition on the wave function; the true shape of the wave function for  $r < r_0$  is lost (see black dashed lines of Fig. 1.1) but is assumed irrelevant, hence it is referred to as a *zero-range* interaction. The pseudopotential assumes that only s-wave phase shift is nonzero, so there is no information regarding the p-wave and higher partial waves. Note in Fig. 1.1 that, with respect to the wave function when  $V = 0$ , the black dashed line appears to be “pulled inward” for  $a_s < 0$  and “pushed outward” for  $a_s > 0$ . In particular, for  $a_s > 0$ , it looks as if a hard-wall boundary condition is imposed at  $r = a_s$ . This is the intuitive interpretation behind the notion of strength of two-body interaction being proportional to  $a_s$  in Eqn. 1.5.

Sometimes the artificial  $\frac{1}{r}$  divergence of the wave function can cause problems. Note that in Fig. 1.1, dividing a black dashed line by  $r$  will cause a divergence, whereas dividing a blue curve by  $r$  does not. One can use a *regularized* pseudopotential [6], which only refers to the regular (non-divergent) part of the wave function:

$$V(\vec{r}) = \frac{2\pi\hbar^2 a_s}{\mu} \delta(\vec{r}) \frac{\partial}{\partial r} r. \quad (1.6)$$

The pseudopotential is too divergent to be directly diagonalized in a numerical computation as one would attempt with true potentials, but, used correctly, it greatly simplifies the

analysis of basic, universal properties of quantum systems. The regularized pseudopotential is often used in few-body theory [7]; the regularization is unnecessary for other applications as is the case of the one-body ansatz problem of Ch. 2 and 3.

Finally, for several atomic species, such as Rb and Cs, the scattering length can in fact be tuned via Feshbach resonances [8].

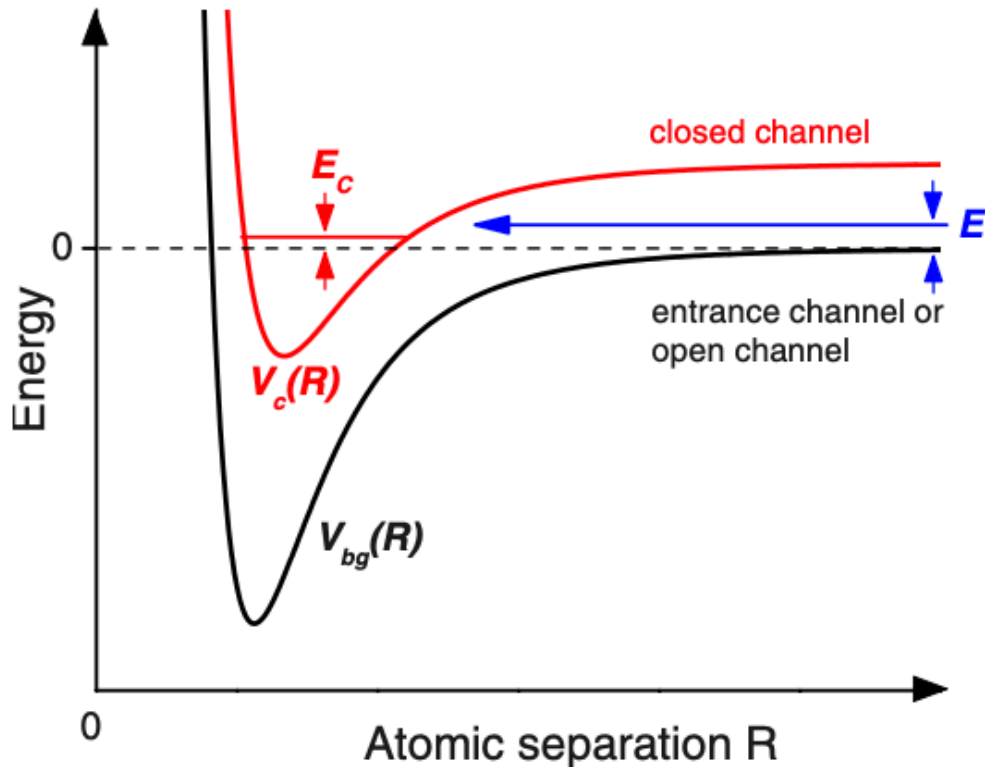


**Figure 1.2.** Schematics of a Feshbach resonance. Image taken from [8].

In a magnetic Feshbach resonance, two different channels corresponding to different hyperfine states of colliding atoms are coupled by a variable magnetic field; Zeeman splitting between the different hyperfine states controls the location of the closed channel threshold with respect to the open channel threshold. A bound state of a closed channel is a resonance since it can decay into the open channel; if that resonance energy is tuned to be close to threshold of open channel, scattering length becomes very large, well described by equation  $a(B) = a_{bg} \left(1 - \frac{\Delta}{B - B_0}\right)$ . The term  $a_{bg}$  refers to the background scattering length of the single open channel away from resonance, while  $\Delta$  and  $B_0$  refer to the width and position of

the resonance. Note that  $B = B_0 + \Delta$  is the position of effectively *zero* scattering length. Therefore, cold atomic systems provide an ideal venue to study few and many-body physics with widely tunable interaction strength.

## 2. ONE-BODY ANSATZ: INTRODUCTION AND METHOD

### 2.1 Introduction to Physics of Many Bosons and Mean-Field Theory

Ever since the early pioneering experimental works first demonstrated successful creation of Bose-Einstein condensates [9]–[11], in which bosons are cooled to  $nK$ -range temperatures such that classical statistical physics no longer applies and fundamental quantum mechanics of cold atoms could be studied rigorously, there has since been an explosion of interest in understanding the behavior of  $N$  bosons. There is truly a wide spectrum of topics. At the few-body side is, for instance, the study of three-body recombination, a process by which 3 atoms collide and exit energetically as a dimer and a free atom, providing the main pathway by which condensates decay in time [12], [13]. At the many-body side, for example, collective excitations of the condensate as a whole have been studied [14]–[16] in order to understand how the effect of s-wave interaction modifies the vibrational frequencies from the usual harmonic oscillator energy levels.

Consider, then, the following Hamiltonian of  $N$  spin-less (or spin-polarized) bosons with mutual two-body interaction within a spherical trap:

$$H = -\frac{\hbar^2}{2m} \sum_{i=1}^N \nabla_i^2 + \frac{1}{2} m \omega^2 \sum_{i=1}^N r_i^2 + \sum_{i < j}^N V(r_{i,j}). \quad (2.1)$$

In this chapter regarding single-particle orbital ansatz, we model the system by using Fermi pseudopotential  $V(r_{i,j}) = g\delta(\vec{r}_i - \vec{r}_j)$ , where  $g = \frac{4\pi\hbar^2 a_s}{m}$  effectively parametrizes the interaction in terms of scattering length while assuming that the microscopic details of  $V$  are irrelevant [17]. The most widely used theory [18], [19] is to assume an *ansatz* wave function of form  $\Psi = \prod_{i=1}^N \phi(\vec{r}_i)$  and variationally minimize the energy functional, which gives the well-known Gross-Pitaevskii (GP) Equation:

$$-\frac{\hbar^2}{2m} \nabla^2 \phi + \frac{1}{2} m \omega^2 r^2 \phi + g(N-1)|\phi|^2 \phi = \epsilon \phi. \quad (2.2)$$

The total energy is given by  $E = N\epsilon - \frac{1}{2} g N(N-1) \int |\phi|^4 d^3\vec{r}$ , where  $\epsilon$  is the orbital energy and chemical potential of the system, quantifying the amount of energy required to add an additional particle to the trap. Note that the total energy is not simply a multiple of  $\epsilon$ ; there

is a need to compensate for an over-counting of particle interaction terms. The solution to Eqn. 2.2 must obey the normalization condition  $\int |\phi|^2 d^3\vec{r} = 1$ . The above equation is a number-conserving form, with the non-linear term vanishing for  $N = 1$ ; one often finds  $N$  rather than  $N - 1$  in the literature. The Gross-Pitaevskii Equation is a non-linear mean-field equation, effectively describing the motion of one particle under the mutual influence of  $N - 1$  other particles through the non-linear term. Note that the coupling constant  $g$  is linearly proportional to  $a_s$ . The equation fails when  $n|a_s|^3 \gg 1$  (where  $n$  is the number density), or in other words when roughly  $N^{1/3}a_s \gg l_t$  (where  $l_t = \sqrt{\frac{\hbar}{m\omega}}$  is the trap length scale). A possible next step is to include a Lee-Huang-Yang correction [20] that gives the next-order term in  $\sqrt{na_s^3}$ , valid when  $a_s > 0$ ; an alternative is to replace the naive pseudopotential by a *regularized* pseudopotential [21], [22].

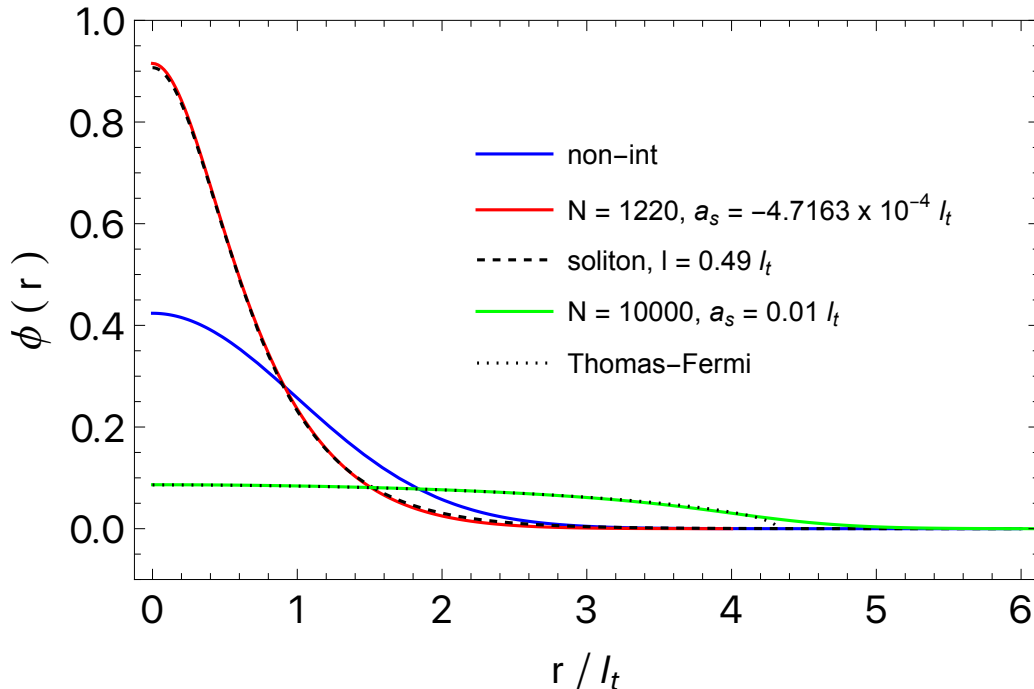


**Figure 2.1.** Comparison of different spherically symmetric solutions of mean-field equation and their approximations.

Fig. 2.1 shows spherically-symmetric solutions to the mean-field equation under three different scenarios as well as relevant approximations. The blue curve is the non-interacting limit, a pure gaussian. Then the chemical potential is  $\epsilon = \frac{3}{2}\hbar\omega$  and the total energy is

$E = \frac{3}{2}N\hbar\omega$  as usual. Red and green curves are numerical solutions to Eqn. 2.2 that we calculate using imaginary time propagation [23] in a finite-difference representation. Split-operator and Crank-Nicolson [24] methods were used in each time step; because function norm is not preserved in imaginary time, normalization condition  $\int |\phi|^2 d^3\vec{r} = 1$  was imposed at every time step.

The scenario for red curve is very close to the criticality of Eqn. 2.2; with just a few more particles or more negative  $a_s$ , the equation admits no solution. Chemical potential is  $\epsilon = 0.37\hbar\omega$ ; total energy is  $E = 1430\hbar\omega$ . Note that the solution is remarkably well approximated by a function  $\phi_l^s = \frac{1}{\sqrt{4\pi}}\sqrt{\frac{12}{\pi^2 l^3}} \operatorname{sech}\left(\frac{r}{l}\right)$ , with  $l = 0.49l_t$ .  $\phi_l^s$  is the functional form for a “bright soliton” in quasi-1D settings, explained later. On the other hand, the numerical solution that is the green curve gives  $\epsilon = 9.47\hbar\omega$  and  $E = 68,710\hbar\omega$ . The scenario for green curve is well within the regime where “Thomas-Fermi” approximation can be applied, in which the kinetic term of Eqn. 2.2 is neglected because the non-linear term dominates. The “Thomas-Fermi” solution exhibits a square-root cusp that is unphysical, in disagreement with the green curve for  $r > 4l_t$ .

A very large volume of literature exists on both theoretical and experimental studies of the mean-field equation, testing its predictions against real condensates in laboratories. Note that for negative  $a_s$ , one cannot arbitrarily increase the number of particles; there exists a threshold critical number of particles  $N_c$  above which the system becomes unstable and will quickly collapse, in a phenomenon known as a “Bosenova” [8], [25]. A gaussian variational treatment [26], [27] of Eqn. 2.2 gives an estimate of  $N_c$  by the relation  $N_c \frac{|a_s|}{l_t} \approx 0.671$ , while a numerical solution [28] of Eqn. 2.2 puts a lower estimate:  $N_c \frac{|a_s|}{l_t} \approx 0.575$ . Ref. [29] studies  $N_c$  beyond spherical symmetry, into the quasi-2D “pancake” and quasi-1D “cigar” configurations as well. Experiments [30], [31] are in reasonable agreement with these predictions, though they typically quote lower range of values for  $N_c$ ; due to the metastable nature of condensates with attractive interaction, and due to quantum fluctuations and tunneling, it may be rather difficult to have condensate atom number steadily approach  $N_c$  in an experiment.

The dynamics of collective excitations of Bose-Einstein condensates are often studied by complementing a time-dependent version of Eqn. 2.2 with the hallmark theory of Bogoliubov modes [32], [33]. In summary, in terms of ground-state solution  $\phi_0$  of Eqn. 2.2 and a set of

Hartree-Fock excited-state orbitals  $\phi_i$ , one solves for the excitation energies  $\hbar\Omega_\lambda = E_\lambda - E_0$  using the following matrix equation:

$$\begin{pmatrix} \underline{B} & \underline{C} \\ \underline{C} & \underline{B} \end{pmatrix} \begin{pmatrix} \vec{U}_\lambda \\ \vec{V}_\lambda \end{pmatrix} = \hbar\Omega_\lambda \begin{pmatrix} \underline{1} & \underline{0} \\ \underline{0} & \underline{-1} \end{pmatrix} \begin{pmatrix} \vec{U}_\lambda \\ \vec{V}_\lambda \end{pmatrix}, \quad (2.3)$$

$$B_{i,j} = (\epsilon_i - \epsilon_0)\delta_{i,j} + g(N-1) \int dV \phi_i^* |\phi_0|^2 \phi_j, \quad (2.4)$$

$$C_{i,j} = g(N-1) \int dV \phi_i^* |\phi_0|^2 \phi_j. \quad (2.5)$$

For  $a_s > 0$  indicating an effectively repulsive interaction amongst the particles, in the limit of large  $gN$ , a Thomas-Fermi approximation can be made; within that approximation, the collective monopole (total  $L = 0$ ) excitation frequencies are found [34] to be  $\Delta E_n = \hbar\omega\sqrt{2n^2 + 3n}$  (compare with the non-interacting result of frequencies  $2n\hbar\omega$  for zero angular momentum trap states). Multiple experiments [14], [35] on excitations agree quite reasonably with the above theories, as well as numerical solutions of the time-dependent version of Gross-Pitaevskii equation [36]–[38].

The non-linear Eqn. 2.2 is neither restricted to spherically symmetric trap nor to zero angular momentum. A large volume of literature (see [39] and [40] for example) studies non-zero angular momentum solutions of the mean-field equation to describe the quantized vortices of Bose-Einstein condensate. Another very interesting direction is to study a non-spherically-symmetric condensate, specifically using cylindrical trap configurations for quasi-1D and quasi-2D settings. It was shown [41] that a cylindrical trap plays a peculiar role, in which the effective one-dimensional scattering length is related to the original s-wave scattering length  $a_s$  by the following relation ( $a_t$  is transverse oscillator length):

$$\frac{a_{1D}}{a_t} = -\frac{1}{2} \frac{a_t}{a_s} \left( 1 - c \frac{a_s}{a_t} \right), \quad c \approx 1.4603. \quad (2.6)$$

Notice that at some finite positive value of  $a_s$ ,  $a_{1D}$  tends to 0 and hence the one-dimensional coupling strength  $g_{1D}$ , inversely proportional to  $a_{1D}$ , diverges; this is known as a “confinement-induced resonance”. By breaking spherical symmetry and reducing the ef-

fective dimension, other interesting phenomena are observed; one example is Ref. [42], which shows that it is possible to have certain out-of-equilibrium states of quasi-1D Bose gas that do not thermalize after thousands of collisions. Another phenomenon is the existence of “bright soliton”, well described by functional form  $\text{sech}(z)$  in the longitudinal direction that exactly solves the one-dimensional mean-field equation [43], [44]. In quasi-one-dimension, unlike in spherically symmetric system, metastable self-bound droplets can form due to attractive pair-wise interaction in the absence of longitudinal trap and can propagate with robust wave form, opening possibilities for manipulating many-body states and demonstrating matter optics and interferometry.

## 2.2 Method of One-Body Ansatz: Orbital Picture

### 2.2.1 $N$ -Body Hamiltonian

The following discussion of methods in this chapter, as well as results in Ch. 3, are originally published in Ref. [45]. Having reviewed the various fascinating many-body phenomena observed in cold Bosonic atomic gas and the successes (and limitations) of mean-field theory in describing them, one cannot help but wonder still about the nature of the non-linear term in Eqn. 2.2. As far as Schrödinger Equation continues to remain valid in non-relativistic quantum mechanics, the true underlying theory of many-particle systems should still be *linear*; the question is how well one can handle the formidable challenge posed by such a multi-dimensional partial differential equation.

In an attempt to move away from the non-linear approximation, one notices that, for spherically symmetric configurations, the root-mean-square radius of the cloud of atoms is a particularly relevant *collective* degree of freedom that does not appear to have been the subject of much attention. In fact, the root-mean-square radius is intimately related to the concept of *hyperradius*. With the hyperradius as a fixed parameter, one may hope to trace out the adiabatic potential energy of the system as a whole, not just a single particle in the mean-field sense. The tremendous success and usefulness of this adiabatic hyperspherical formalism in the realm of few-body physics will be explored in greater detail in Ch. 4. For now, simply take the hyperradius to be *the* root-mean-square radius:  $R^2 = \frac{1}{N} \sum_{i=1}^N r_i^2$ .

We work with a fundamental assumption that changes in this overall collective coordinate are far slower than changes in other degrees of freedom, related to different rearrangements of the particles. In a sense, this is a self-fulfilling prophecy; when calculations show that non-adiabatic corrections related to hyperradial derivatives are small, then the assumption is justified.

Return to the  $N$ -body Hamiltonian of Eqn. 2.1 with Fermi pseudopotential  $V(r_{i,j}) = g\delta(\vec{r}_i - \vec{r}_j)$ , and perform a transformation from Cartesian coordinates to a system of coordinates  $(R, \Omega)$ , where  $\Omega$  refers to the various  $3N - 1$  degrees of freedom other than  $R$ :

$$\sum_{i=1}^N \nabla_i^2 = \frac{1}{N} \left( \frac{1}{R^{3N-1}} \frac{\partial}{\partial R} \left( R^{3N-1} \frac{\partial}{\partial R} \right) - \frac{\Lambda^2}{R^2} \right), \quad (2.7)$$

$$H = -\frac{1}{2N} \frac{1}{R^{\frac{3N-1}{2}}} \frac{\partial^2}{\partial R^2} R^{\frac{3N-1}{2}} + H_A, \quad (2.8)$$

$$H_A = \frac{1}{2N} \left( \frac{(3N-1)(3N-3)}{4R^2} + \frac{\Lambda^2}{R^2} \right) + \frac{1}{2}NR^2 + 4\pi a_s \sum_{i<j} \delta(\vec{r}_i - \vec{r}_j). \quad (2.9)$$

Here and for the rest of this chapter and Ch. 3, we shall use dimensionless units with length in terms of oscillator length  $l_t = \sqrt{\frac{\hbar}{m\omega}}$  and energy in terms of oscillator units  $\hbar\omega$ . The external trap only depends on  $R$ ; this is one of the powerful appeals of using this collective coordinate. The Hamiltonian is split into a hyperradial kinetic term of second derivative and  $H_A$ , which contains all other terms for which  $R$  is regarded a constant. A repulsive term proportional to  $\frac{(3N-1)(3N-3)}{4R^2}$  is called a “mock” centrifugal potential, appearing as a result of removing a first-derivative in  $R$  for future convenience. The operator  $\Lambda^2$  is called a “grand angular momentum operator” (see Appendix B for more details in a different case when the center-of-mass is removed). In general, there exist eigenfunctions  $Y_{\lambda,\mu}$ , called “hyperspherical harmonics”, that satisfy equation  $\Lambda^2 Y_{\lambda,\mu} = \lambda(\lambda + 3N - 2)Y_{\lambda,\mu}$ , with integer  $\lambda = 0, 1, \dots$  and different quantum numbers  $\mu$  distinguishing degenerate states. The hyperspherical harmonics fully solve the problem when there is no interaction, and even

for problems with interactions, there are works that generally utilize some form of expansions in these functions [46]–[49].

Now, because of the sheer difficulty of attempting to diagonalize the full Hamiltonian, consider the following total *ansatz* wavefunction:

$$\Psi = \frac{F(R)}{R^{(3N-1)/2}} \frac{B(R, \Omega)}{\sqrt{C(R)}}. \quad (2.10)$$

Let bra-ket notation indicate a hyperangular integration with  $R$  held fixed:  $\langle \psi | \phi \rangle = \int \psi^* \phi \, d\Omega$ . Suppose there is some reasonable real ansatz function  $B$  that approximately describes the eigenfunction  $\Phi_0$  corresponding to the lowest adiabatic eigenvalue  $U_0(R)$  of  $H_A$ , which must exist in principle:  $H_A \Phi_0 = U_0(R) \Phi_0$ .  $C(R) = \langle B | B \rangle$  is the *a priori* unknown hyperangular normalization integral of  $B$  at each fixed  $R$ . Then compute  $\langle B | H | \Psi \rangle = E \langle B | \Psi \rangle$  to obtain the following effective one-dimensional Schrödinger Equation:

$$-\frac{1}{2N} F''(R) - \frac{Q(R)}{2N} F(R) + \frac{\langle B | H_A | B \rangle}{C} F(R) = E F(R), \quad (2.11)$$

$$Q(R) = \frac{\langle B | B'' \rangle}{C} + \frac{1}{4} \left( \frac{C'}{C} \right)^2 - \frac{1}{2} \frac{C''}{C}. \quad (2.12)$$

$Q$  is called a diagonal non-adiabatic correction, related to how quickly  $B$  changes with respect to  $R$ ; if  $Q = 0$ , one is completely justified in taking  $R$  as a slow, adiabatic parameter. Note that the variational principle holds here, in that the expectation value  $U(R)$  of adiabatic  $H_A$  must give an upper bound over true lowest adiabatic eigenvalue  $U_0$ :

$$U(R) = \frac{\langle B | H_A | B \rangle}{C} \geq U_0(R). \quad (2.13)$$

### 2.2.2 Choice of Independent-Particle Ansatz

What should the ansatz function  $B$  be? In the vein of hyperspherical harmonic expansion previously mentioned, perhaps the simplest approximation would be to take  $B$  to be a constant [50]. In fact, the lowest hyperspherical harmonics  $Y_{0,0}$  is a constant; indeed, for non-

interacting bosons, the total ground-state wave function is  $\prod_{i=1}^N e^{-\frac{1}{2}r_i^2} = e^{-\frac{1}{2}NR^2}$ , depending *only* on  $R$  with no other dependence. This is known as a “K-Harmonic” approximation, for which the non-adiabatic correction  $Q(R) = 0$  and the expectation value  $U(R)$  takes a simple analytical form that is easy to interpret. One highlight of that result is that, because of the dimensionality of the Dirac delta function, there is a  $R^{-3}$  term in  $U(R)$  whose sign is given by  $a_s$ ; with a sufficiently large value of  $Na_s$ ,  $U(R)$  ceases to support a local minimum, giving an intuitive picture of macroscopic collapse of attractive condensates.

The K-Harmonic approximation was extended to treat traps that are no longer spherically symmetric, in which case there is not one adiabatic parameter  $R$  but two or three parameters to calculate adiabatic surfaces for the condensates [51], [52]. The ideas are simple enough that even degenerate Fermi gas could be treated in a similar manner in terms of a Slater determinant of trap eigenstates, for spherically symmetric [53] and non-symmetric [54] systems. Quite recently, an interesting extension was presented that treated dipolar condensates within the K-Harmonic framework [55]. However, results [50] from the K-Harmonic approximation disagree significantly with known results of mean-field theory, not just for the collective excitation frequencies, but (more seriously) also the ground-state energies of condensates. It is interesting to note that for the K-Harmonic approximation, the largest value  $N_c$  that supports a local minimum in the potential in order for a metastable condensate to form is given approximately by  $N_c \frac{|a_s|}{t} \approx 0.671$ , in agreement with the gaussian variational treatment [27] in over-estimating the critical number of attractive condensate.

The great discrepancies between the predictions of mean-field theory and the K-Harmonic approximation can be understood by examining the shapes of typical solutions of the mean-field equation (see Fig. 2.1). It is clear that, for both attractive and repulsive two-body interaction, the solutions of Eqn. 2.2 deviate significantly from a gaussian, and hence there must be a wealth of information in the total orbital product wave function  $\Psi = \prod_{i=1}^N \phi(\vec{r}_i)$  that has not been explored in terms of the root-mean-square radius  $R$ . Therefore, we choose now the ansatz hyperangular function  $B$  to be the following functional form:

$$B(R, \Omega) = \prod_{i=1}^N \phi(\vec{r}_i) \tag{2.14}$$

Note that there is a great variety of different single-particle orbitals  $\phi$  that we may use in our calculations. Given experimental parameters  $(N, a_s, \omega)$ , the orbital  $\phi$  that enters the variational calculation in Eqn. 2.11 does not have to be the correct solution of Eqn. 2.2. We may choose to substitute  $N$  by some other  $N_0 \neq N$  in Eqn. 2.2 and obtain a different orbital  $\phi$  in order to explore its consequences. In other words, a set of several different  $N_0$  will lead to correspondingly different orbitals, and hence several different results for the expectation values  $U(R)$ . This idea is particularly useful for situations with  $a_s < 0$ , for which it may be possible that Eqn. 2.2 has no solution. On top of  $N_0 \neq N$ , we also explore the consequences of using as independent-particle orbital the *bright soliton* function  $\phi_l^s = \frac{1}{\sqrt{4\pi}} \sqrt{\frac{12}{\pi^2 l^3}} \operatorname{sech}\left(\frac{r}{l}\right)$ , which will give a series of different values  $U(R)$  for each choice of parameter  $l > 0$ . This choice is motivated by the observation in Fig. 2.1 that the bright soliton orbital does a remarkable job in approximating the correct numerical solution of the mean-field equation.

### 2.2.3 Extended Ansatz of Several Orbitals

It was noted that there are non-unique choices of single-particle orbitals  $\phi$  that one may use for the ansatz channel function in Eqn. 2.14. A general symmetrized wave function of form  $\hat{\mathcal{S}}[\phi_1(\vec{r}_1) \cdots \phi_N(\vec{r}_N)]$ , with symmetrization operator  $\hat{\mathcal{S}}$  and different orbitals  $\phi_1, \phi_2, \dots$ , is too complicated and beyond the scope of this dissertation, but a limited formalism using several different kinds of orbitals  $\phi$  is implemented as follows. To proceed, we choose an alternate form of ansatz hyperangular function  $B$  in the following manner, with some  $n > 1$ :

$$B(R, \Omega) = \sum_{\mu=1}^n D_{\mu}(R) \frac{B_{\mu}(R, \Omega)}{\sqrt{C_{\mu}(R)}}, \quad B_{\mu}(R, \Omega) = \prod_{i=1}^N \phi_{\mu}(\vec{r}_i). \quad (2.15)$$

First select  $n$  different orbitals  $\phi_1(\vec{r}), \dots, \phi_n(\vec{r})$ , and construct individual single-orbital functions  $B_{\mu}$ . Denote  $C_{\mu,\nu} = \langle B_{\mu} | B_{\nu} \rangle$  and  $C_{\mu,\mu} = C_{\mu}$ , where  $C_{\mu}$  is the hyperangular normalization integral of  $B_{\mu}$  to be computed. Column vector  $\vec{D} = (D_1(R), \dots, D_n(R))$  of expansion coefficients denotes the particular linear combination of  $B_{\mu}$  that constitutes the total ansatz, and it will be computed by a diagonalization procedure to be discussed soon. Be aware that individual  $C_{\mu}(R)$  is *not* the same as the total normalization integral  $C(R) = \langle B | B \rangle$ . This multi-orbital approach is quite similar in spirit to the configuration-interaction (CI)

methods routinely implemented in quantum chemistry [56], [57]. There are some similarities to a recently proposed method of “eigenvector continuation” [58], where eigenstates of certain model Hamiltonians are used to approximately diagonalize a different Hamiltonian. The limited diagonalization scheme here draws inspirations from the adiabatic hyperspherical problems of few-body physics, using basis sets such as correlated gaussians [59]–[61] to diagonalize the fixed-hyperradius adiabatic Hamiltonian.

The following five  $n$  by  $n$  matrices,  $\underline{O}$ ,  $\underline{H}$ ,  $\underline{P}$ ,  $\underline{Q}$  (not to be confused with the quantity  $Q(R)$ ), and  $\underline{P}^2$  (not  $\underline{P} \times \underline{P}$ ), are needed; their matrix elements are as follows:

$$O_{\mu,\nu} = \left\langle \frac{B_\mu}{\sqrt{C_\mu}} \left| \frac{B_\nu}{\sqrt{C_\nu}} \right. \right\rangle = \frac{C_{\mu,\nu}}{\sqrt{C_\mu C_\nu}}, \quad (2.16)$$

$$H_{\mu,\nu} = \left\langle \frac{B_\mu}{\sqrt{C_\mu}} \left| H_A \left| \frac{B_\nu}{\sqrt{C_\nu}} \right. \right. \right\rangle = \frac{\langle B_\mu | H_A | B_\nu \rangle}{\sqrt{C_\mu C_\nu}}, \quad (2.17)$$

$$P_{\mu,\nu} = \left\langle \frac{B_\mu}{\sqrt{C_\mu}} \left| \frac{\partial}{\partial R} \left| \frac{B_\nu}{\sqrt{C_\nu}} \right. \right. \right\rangle = \frac{\langle B_\mu | B'_\nu \rangle}{\sqrt{C_\mu C_\nu}} - \frac{C'_\nu}{2C_\nu} O_{\mu,\nu}, \quad (2.18)$$

$$Q_{\mu,\nu} = \left\langle \frac{B_\mu}{\sqrt{C_\mu}} \left| \frac{\partial^2}{\partial R^2} \left| \frac{B_\nu}{\sqrt{C_\nu}} \right. \right. \right\rangle = \frac{\langle B_\mu | B''_\nu \rangle}{\sqrt{C_\mu C_\nu}} - \frac{C'_\nu}{C_\nu} \frac{\langle B_\mu | B'_\nu \rangle}{\sqrt{C_\mu C_\nu}} + \left( \frac{3}{4} \left( \frac{C'_\nu}{C_\nu} \right)^2 - \frac{C''_\nu}{2C_\nu} \right) O_{\mu,\nu}, \quad (2.19)$$

$$P^2_{\mu,\nu} = \left\langle \frac{\partial}{\partial R} \left( \frac{B_\mu}{\sqrt{C_\mu}} \right) \left| \frac{\partial}{\partial R} \left( \frac{B_\nu}{\sqrt{C_\nu}} \right) \right. \right\rangle = \frac{\langle B'_\mu | B'_\nu \rangle}{\sqrt{C_\mu C_\nu}} - \frac{C'_\mu}{2C_\mu} \frac{\langle B_\mu | B'_\nu \rangle}{\sqrt{C_\mu C_\nu}} - \frac{C'_\nu}{2C_\nu} \frac{\langle B_\nu | B'_\mu \rangle}{\sqrt{C_\mu C_\nu}} + \frac{C'_\mu C'_\nu}{4C_\mu C_\nu} O_{\mu,\nu}. \quad (2.20)$$

Evaluate the matrix elements of the adiabatic Hamiltonian as follows:

$$\begin{aligned}
\langle B_\mu | H_A | B_\nu \rangle &= \frac{\langle B_\mu | \Lambda^2 | B_\nu \rangle}{2NR^2} \\
&+ \left( \frac{(3N-1)(3N-3)}{8NR^2} + \frac{1}{2}NR^2 \right) C_{\mu,\nu} \\
&+ 4\pi a_s \left( \frac{N(N-1)}{2} \right) \langle B_\mu | \delta(r_2 - r_1) | B_\nu \rangle, \tag{2.21}
\end{aligned}$$

$$\begin{aligned}
\langle B_\mu | \Lambda^2 | B_\nu \rangle &= R^2 \left( \langle B_\mu | B''_\nu \rangle + \frac{3N-1}{R} \langle B_\mu | B'_\nu \rangle \right. \\
&\left. - N^2 \langle B_\mu | \nabla_1^2 | B_\nu \rangle \right). \tag{2.22}
\end{aligned}$$

The matrices  $\underline{O}$ ,  $\underline{H}$ , and  $\underline{P}^2$  are symmetric, but  $\underline{P}$  and  $\underline{Q}$  are not.  $\underline{O}$  is the overlap matrix, with  $O_{\mu,\mu} = 1$ , but the off-diagonal elements do not generally vanish since the basis of orbitals was not initially chosen with guaranteed orthogonality. In principle  $\underline{O}' = \underline{P} + \underline{P}^T$  and  $\underline{O}'' = \underline{Q} + \underline{Q}^T + 2\underline{P}^2$ , with  $P_{\mu,\mu} = 0$  and  $Q_{\mu,\mu} = -P_{\mu,\mu}^2$ .

Note that the overall normalization integral is  $C(R) = \langle B | B \rangle = \vec{D}^T \underline{O} \vec{D}$ , while  $\langle B | H_A | B \rangle = \vec{D}^T \underline{H} \vec{D}$ . Now solve the generalized eigenvalue problem at each fixed value of  $R$ :

$$\underline{H} \vec{D} = U(R) \underline{O} \vec{D}. \tag{2.23}$$

An eigenvalue  $U(R)$  obtained here is precisely the quantity  $\frac{\langle B | H_A | B \rangle}{C}$  for the hyperradial Eqn. 2.11 concerning  $F(R)$ . Also, one writes the radial derivative of normalization as  $C' = 2\vec{D}^T \underline{O} \vec{D}' + \vec{D}^T \underline{O}' \vec{D}$ ,  $C'' = 2\vec{D}'^T \underline{O} \vec{D}' + 2\vec{D}^T \underline{O} \vec{D}'' + 4\vec{D}^T \underline{O}' \vec{D}' + \vec{D}^T \underline{O}'' \vec{D}$ , and  $\langle B | B'' \rangle = \vec{D}^T \underline{Q} \vec{D} + 2\vec{D}^T \underline{P} \vec{D}' + \vec{D}^T \underline{Q} \vec{D}''$ . First eliminate the term  $\vec{D}^T \underline{Q} \vec{D}''$  in  $Q(R)$ , and then impose the chosen normalization condition  $C(R) = \vec{D}^T \underline{O} \vec{D} = 1$  at each  $R$  for the eigenvector  $\vec{D}$ . The non-adiabatic correction  $Q(R)$  (Eqn. 2.12) for the corresponding  $B(R, \Omega)$  (Eqn. 2.15) can then be calculated as follows:

$$Q(R) = -\vec{D}'^T \underline{O} \vec{D}' - 2\vec{D}^T \underline{P} \vec{D}' + \vec{D}^T \left( \frac{1}{2}(\underline{Q} - \underline{Q}^T) - \underline{P}^2 \right) \vec{D}. \tag{2.24}$$

Finally, to compute  $\vec{D}'$ , follow the ideas of Ref. [62] and first differentiate both sides of the generalized eigenvalue Eqn. 2.23. Next, solve the system  $(\underline{H}-U\underline{Q})\vec{Y} = (-\underline{H}'+U'\underline{Q}+U\underline{Q}')\vec{D}$ , where  $\vec{Y} = \vec{D}' + c_D\vec{D}$  for some initially unknown coefficient  $c_D$ . Using the chosen condition  $\vec{D}^T\underline{Q}\vec{D} = 1$ , then  $c_D = \vec{D}^T\underline{Q}\vec{Y} + \frac{1}{2}\vec{D}^T\underline{Q}'\vec{D}$ . This type of method is also applied to find the derivative of any other vector as arises in the next section.

#### 2.2.4 Dealing with Linear Dependence of Similar Orbitals

When we attempt to implement the above multi-orbital formalism using different chosen orbitals  $\phi_\mu$  (such as those seen in Fig. 2.1), which all look fairly similar as nodeless functions, approximate linear dependence can arise between the different basis functions  $B_\mu(R, \Omega)$ . The linear dependence leads to numerical instability that can in turn produce unreasonable generalized eigenvalues  $U(R)$  of Eqn. 2.23. Similar linear dependence problems also arise in Ref. [59], for example, given a particular basis set of correlated gaussians used to compute few-body adiabatic hyperspherical potential curves. To deal with such pathologies, the generalized eigenvalue problem can be stabilized by a commonly-used procedure as follows. First, diagonalize the overlap matrix at each  $R$ :  $\underline{Q}\vec{X}_l = o_l\vec{X}_l$ . Sort the eigenvalues such that  $o_1 \geq \dots \geq o_n$ , and define the corresponding orthogonal eigenvector matrix  $\underline{X} = (\vec{X}_1, \dots, \vec{X}_n)$ .

Now examine the representation where  $\tilde{\underline{Q}} = \underline{X}^T\underline{Q}\underline{X}$  is diagonal. With  $\tilde{\underline{H}} = \underline{X}^T\underline{H}\underline{X}$  and  $\vec{D} = \underline{X}^T\vec{D}$ , the generalized eigenvalue problem in this new representation is  $\tilde{\underline{H}}\vec{D} = U(R)\tilde{\underline{Q}}\vec{D}$ . Everything is equivalent to Eqn. 2.23 at this point, but, empirically speaking, if at least one eigenvalue of  $\underline{Q}$  is smaller than some threshold value (typically  $10^{-4}$ ), the eigenvalues  $U$  quickly and unphysically collapse towards  $-\infty$ .

To fix this issue, choose some  $c < n$  and define a submatrix  $\underline{X}_c$  of  $\underline{X}$ :  $\underline{X}_c = (\vec{X}_1, \dots, \vec{X}_c)$ . Note that  $\underline{X}_c^T\underline{X}_c = \underline{1}_c$ , but  $\underline{X}_c\underline{X}_c^T \neq \underline{1}_n$ . One can systematically reduce the dimension of the basis set, so that  $B(R, \Omega)$  is composed of  $c$ , not  $n$ , basis functions, each of which is a suitable linear combination of  $B_\mu$ 's. Those linear combinations of  $B_\mu$ 's with very small corresponding eigenvalues of  $\underline{Q}$  mostly cancel themselves out, so they are thrown away.

To be concrete, define  $\underline{\tilde{O}}_c = \underline{X}_c^T \underline{O} \underline{X}_c$  and  $\underline{\tilde{H}}_c = \underline{X}_c^T \underline{H} \underline{X}_c$ , and solve instead the following generalized eigenvalue problem:

$$\underline{\tilde{H}}_c \vec{D} = \tilde{U}(R) \underline{\tilde{O}}_c \vec{D}. \quad (2.25)$$

This is referred to as the *reduced* representation throughout this chapter and Ch. 3. The  $c$  eigenvalues  $\tilde{U}$  are different from the  $n$  eigenvalues of Eqn. 2.23 in the *primitive* (original) representation, obeying the Hylleraas-Undheim theorem [63] as the basis dimension is reduced one-by-one. These  $\tilde{U}$  are then taken for  $\frac{\langle B|H_A|B \rangle}{C}$  of Eqn. 2.11 in the variational formulation.

Finally, the chosen normalization condition for the eigenvectors is now  $\vec{D}^T \underline{\tilde{O}}_c \vec{D} = 1$ . After a lengthy algebraic simplification, the corresponding expression for the non-adiabatic correction  $Q(R)$  of Eqn. 2.12 is as follows:

$$Q(R) = -\vec{Z}^T \underline{Q} \vec{Z}' - 2\vec{Z}^T \underline{P}^T \vec{Z}' + \vec{Z}^T \left( \frac{1}{2}(\underline{Q} - \underline{Q}^T) - \underline{P}^2 \right) \vec{Z} \quad (2.26)$$

Here  $\vec{Z} = \underline{X}_c \vec{D}$ . Of course, if  $c = n$  and no linear combination of  $B_\mu$ 's has been eliminated, this is completely equivalent to the expression for  $Q(R)$  (Eqn. 2.24) in the primitive representation of previous section.

## 2.3 Hyperangular Integration: Contour Deformation

### 2.3.1 Matrix Elements as 1-D Complex Integrals

Let spherically symmetric orbital  $\phi(\vec{r}_i) = \frac{1}{\sqrt{4\pi}}u(r_i)$ . Having discussed the formalism and the various required hyperangular integrals, we finally explain how the integrals are performed.

For the simplest example, consider  $C_{\mu,\nu} = \int d\Omega B_\mu B_\nu = \int d\Omega \prod_{i=1}^N \phi_\mu(\vec{r}_i) \phi_\nu(\vec{r}_i)$ . At a particular value of hyperradius  $R$ , write  $\int d\Omega = \int d\Omega dR' \delta(R-R') = N^{-3N/2} R^{-(3N-1)} \int \prod_{i=1}^N d^3 r_i' \delta(R-R')$ , where  $R' = \sqrt{\frac{1}{N} \sum_{i=1}^N r_i'^2}$ , meant to distinguish from  $R$  to avoid confusion. As in Ref. [60], we use the following representation of Dirac delta function:

$$\delta(R - R') = \frac{NR}{\pi} \int_{-\infty}^{\infty} dk e^{ikN(R'^2 - R^2)}. \quad (2.27)$$

After simplification,  $C_{\mu,\nu}$  becomes:

$$\begin{aligned} C_{\mu,\nu}(R) &= \frac{1}{N^{3N/2} R^{3N-1}} \int \prod_{i=1}^N d^3 \vec{r}_i' \delta(R - R') \prod_{j=1}^N \phi_{\mu}(\vec{r}_j') \phi_{\nu}(\vec{r}_j') \\ &= \frac{1}{N^{3N/2} R^{3N-1}} \left( \frac{NR}{\pi} \right) \int_{-\infty}^{\infty} dk e^{-ikNR^2} \left[ \int_0^{\infty} dr' r'^2 e^{ikr'^2} u_{\mu}(r') u_{\nu}(r') \right]^N. \end{aligned} \quad (2.28)$$

The delta function allows an evaluation of the hyperangular integral in terms of the individual particle coordinates  $\vec{r}_i$ , which is *much* easier than trying to express  $\phi$  in any hyperangular coordinate system (see Appendices B and C). For example, for a term in  $H_{\mu,\nu}$  coming from the Fermi pseudopotential, dropping primes ( $'$ ) for notational simplicity, we get the following:

$$\begin{aligned} &\langle B_{\mu} | \delta(\vec{r}_2 - \vec{r}_1) | B_{\nu} \rangle \\ &= \frac{1}{N^{3N/2} R^{3N-1}} \left( \frac{NR}{\pi} \right) \int_{-\infty}^{\infty} dk e^{-ikNR^2} \prod_{i=3}^N \left[ \int d^3 \vec{r}_i e^{ikr_i^2} \phi_{\mu}(\vec{r}_i) \phi_{\nu}(\vec{r}_i) \right] \\ &\times \left[ \int d^3 \vec{r}_1 \int d^3 \vec{r}_2 e^{ikr_1^2} \phi_{\mu}(\vec{r}_1) \phi_{\nu}(\vec{r}_1) \delta(\vec{r}_2 - \vec{r}_1) e^{ikr_2^2} \phi_{\mu}(\vec{r}_2) \phi_{\nu}(\vec{r}_2) \right] \\ &= \left( \frac{1}{4\pi} \right) \frac{1}{N^{3N/2} R^{3N-1}} \left( \frac{NR}{\pi} \right) \int_{-\infty}^{\infty} dk e^{-ikNR^2} \left[ \int_0^{\infty} dr r^2 e^{2ikr^2} (u_{\mu}(r) u_{\nu}(r))^2 \right] \\ &\times \left[ \int_0^{\infty} dr r^2 e^{ikr^2} u_{\mu}(r) u_{\nu}(r) \right]^{N-2}. \end{aligned} \quad (2.29)$$

The other integrals of interest are:  $\langle B_{\mu} | B'_{\nu} \rangle$ ,  $\langle B_{\mu} | B''_{\nu} \rangle$ ,  $\langle B'_{\mu} | B'_{\nu} \rangle$ , and  $\langle B_{\mu} | \nabla_1^2 | B_{\nu} \rangle$ , where prime denotes  $\frac{\partial}{\partial R}$  here. Using  $\frac{\partial}{\partial R} = \sum_{i=1}^N \frac{\partial r_i}{\partial R} \frac{\partial}{\partial r_i} = \sum_{i=1}^N \frac{r_i}{R} \frac{\partial}{\partial r_i}$  and  $\nabla^2 u(r) = \frac{1}{r^2} \frac{\partial}{\partial r} \left( r^2 \frac{\partial u}{\partial r} \right)$ , one can derive expressions such as an example here:

$$\begin{aligned}
\langle B_\mu | B'_\nu \rangle &= \left( \frac{N}{R} \right) \frac{1}{N^{3N/2} R^{3N-1}} \left( \frac{NR}{\pi} \right) \int_{-\infty}^{\infty} dk e^{-ikNR^2} \left[ \int_0^{\infty} dr r^3 e^{ikr^2} u_\mu(r) \frac{\partial u_\nu}{\partial r}(r) \right] \\
&\quad \times \left[ \int_0^{\infty} dr r^2 e^{ikr^2} u_\mu(r) u_\nu(r) \right]^{N-1}. \tag{2.30}
\end{aligned}$$

To close this subsection, the following expression can then be derived for the matrix element of  $\Lambda^2$ , verifying that  $\langle B_\mu | \Lambda^2 | B_\nu \rangle = \langle B_\nu | \Lambda^2 | B_\mu \rangle$ :

$$\begin{aligned}
\langle B_\mu | \Lambda^2 | B_\nu \rangle &= N(N-1) \frac{1}{N^{3N/2} R^{3N-1}} \left( \frac{NR}{\pi} \right) \int_{-\infty}^{\infty} dk e^{-ikNR^2} \left[ \int_0^{\infty} dr r^2 e^{ikr^2} u_\mu(r) u_\nu(r) \right]^{N-2} \\
&\quad \times \left( \left[ \int_0^{\infty} dr r^4 e^{ikr^2} u_\mu u_\nu \right] \times \left[ \int_0^{\infty} dr r^2 e^{ikr^2} \frac{\partial u_\mu}{\partial r} \frac{\partial u_\nu}{\partial r} \right] \right. \\
&\quad \left. - \left[ \int_0^{\infty} dr r^3 e^{ikr^2} u_\mu \frac{\partial u_\nu}{\partial r} \right] \times \left[ \int_0^{\infty} dr r^3 e^{ikr^2} u_\nu \frac{\partial u_\mu}{\partial r} \right] \right). \tag{2.31}
\end{aligned}$$

### 2.3.2 Integration by Steepest Descent

Note now that every integral of the previous section has the form  $\int_{-\infty}^{\infty} dk e^{-ikNR^2} g(k) [I(k)]^\beta$ . Factor  $g(k)$  is not being taken to power  $N$ , but  $I(k) = \int_0^{\infty} dr r^2 e^{ikr^2} u_\mu(r) u_\nu(r)$  is taken to power  $\beta = N, N-1$  or  $N-2$ . Because a factor is being powered to large values of  $N$ , the integrand oscillates extremely rapidly on the real line of  $k$ , making the original formulation of the integrals above nearly impossible. The way to solve this problem is by applying the *method of steepest descent* [64].

Start by writing  $e^{-ikNR^2} [I(k)]^\beta = e^{Nf(k)}$ , where  $f(k) = -ikR^2 + \frac{\beta}{N} \log I(k)$ . Notice that for  $k = i\kappa$ ,  $\kappa \in \mathbb{R}$ , assuming that  $I(k)$  converges, then  $I(k)$  is a real, positive quantity, so  $f(k)$  is also real. For example, if  $u(r) = \frac{2}{\pi^{1/4}} e^{-\frac{r^2}{2}}$ , then  $I(k) = (1 - ik)^{-3/2}$  if  $\text{Im } k > -1$ .

As a function of  $R$ , there exists a *saddle point*  $k = i\kappa_0$  where  $f(k)$  is a minimum on the imaginary axis. By the Cauchy-Riemann equations, with  $k = x + iy$ , the following conditions hold at  $k = i\kappa_0$ :  $\frac{\partial \text{Re}(f)}{\partial x} = 0$ ,  $\frac{\partial \text{Im}(f)}{\partial x} = 0$ ,  $\frac{\partial^2 \text{Re}(f)}{\partial x^2} < 0$ , and  $\frac{\partial^2 \text{Im}(f)}{\partial x^2} = 0$ .

Therefore, on the contour  $\Gamma$  where  $k = x + i\kappa_0$ ,  $x \in (-\infty, \infty)$ , the oscillations in  $e^{Nf(k)}$  are minimized as the amplitude rapidly decreases away from the saddle point. We deform the contour and evaluate the resulting smooth integral by the usual Gaussian quadrature rules [65]:

$$\int_{-\infty}^{\infty} dk g(k) e^{Nf(k)} = e^{Nf(i\kappa_0)} \int_{\Gamma} dk g(k) e^{N(f(k)-f(i\kappa_0))}. \quad (2.32)$$

To be more explicit, define the following set of even-parity off-centered gaussian fitting functions and their corresponding integral transforms, where  $l$  is some chosen length scale (do not confuse it with length scale of bright soliton orbital) and  $r_0$  is the distance between neighboring peaks:

$$\mathcal{B}_n(l, r_0, r) = \exp\left(-\left(\frac{r - nr_0}{l}\right)^2\right) + \exp\left(-\left(\frac{r + nr_0}{l}\right)^2\right), \quad (2.33)$$

$$\begin{aligned} & \mathcal{B}_m(\sqrt{2}l, 2r_0, r) \mathcal{B}_n(\sqrt{2}l, 2r_0, r) \\ &= \exp\left(-\frac{(m-n)^2 r_0^2}{l^2}\right) \mathcal{B}_{m+n}(l, r_0, r) + \exp\left(-\frac{(m+n)^2 r_0^2}{l^2}\right) \mathcal{B}_{|m-n|}(l, r_0, r), \end{aligned} \quad (2.34)$$

$$\begin{aligned} \tilde{\mathcal{B}}_n(l, r_0, k) &= \int_0^{\infty} dr e^{ikr^2} r^2 \mathcal{B}_n(l, r_0, r) = \exp\left(-\frac{(nr_0)^2}{l^2} \left(1 + \frac{1}{ikl^2 - 1}\right)\right) \\ &\times \left[ \frac{\sqrt{\pi}}{2} \left(\frac{1}{l^2} - ik\right)^{-3/2} + \sqrt{\pi} \frac{(nr_0)^2}{l^4} \left(\frac{1}{l^2} - ik\right)^{-5/2} \right]. \end{aligned} \quad (2.35)$$

To evaluate and analytically continue  $I(k)$  in the complex plane, we perform a least-squares fitting approximation with chosen maximum basis index  $n_m$  for  $\sqrt{u_\mu(r)u_\nu(r)}$  ( $u_\nu$  if  $\mu = \nu$ ) that is originally expressed in a discrete point grid:  $\sqrt{u_\mu(r)u_\nu(r)} \approx \sum_{n=0}^{n_m} \mathcal{C}_n \mathcal{B}_n(\sqrt{2}l, 2r_0, r)$ . We only deal with nodeless orbitals here, so  $\sqrt{u_\mu(r)u_\nu(r)} \geq 0$ , and also the orbitals are even functions of  $r$  so we choose to describe them with even functions  $\mathcal{B}_n(l, r_0, r)$ . Typically, when we choose  $l$  and  $r_0$  to be roughly the same value, at least an order of magnitude smaller than the overall length scale of the orbital, and choose  $n_m$  large enough to cover the decaying tail to some sufficiently large radius, this least-squares fitting works quite well in practice. Then the expansion is used to compute the following:

$$\begin{aligned}
I(k) &= \int_0^\infty dr r^2 e^{ikr^2} \left( \sqrt{u_\mu(r)u_\nu(r)} \right)^2 \\
&= \sum_{m=0}^{n_m} \sum_{n=0}^{n_m} \mathcal{C}_m \mathcal{C}_n \exp \left( -\frac{(m-n)^2 r_0^2}{l^2} \right) \tilde{\mathcal{B}}_{m+n}(l, r_0, k) \\
&\quad + \sum_{m=0}^{n_m} \sum_{n=0}^{n_m} \mathcal{C}_m \mathcal{C}_n \exp \left( -\frac{(m+n)^2 r_0^2}{l^2} \right) \tilde{\mathcal{B}}_{|m-n|}(l, r_0, k). \tag{2.36}
\end{aligned}$$

Expanding  $\sqrt{u_\mu(r)u_\nu(r)}$  and taking its square ensures that the resulting approximate  $I(k)$  is positive on the imaginary axis of  $k$  (where it converges). If, on the other hand, one expands  $u_\mu(r)u_\nu(r)$  with  $\mu \neq \nu$ , then least-squares fitting does not guarantee the positiveness of  $I(k)$ . We take the principal branch of  $\log I(k)$  and search for saddle point  $k = i\kappa_0$ ,  $\kappa_0 > -\frac{1}{l^2}$  at each fixed  $R$ ; again, with  $I(k) > 0$  on the imaginary axis, there will be no unphysical difficulty arising from the branch cut of  $\log I(k)$ . We emphasize that  $l$  should be far smaller than the size of the orbitals  $u_\mu$  and  $u_\nu$ , not only for good fitting but to ensure that the singularity  $k = -\frac{i}{l^2}$  in  $\tilde{\mathcal{B}}_n(l, r_0, k)$  does not hamper the search for  $\kappa_0$ .

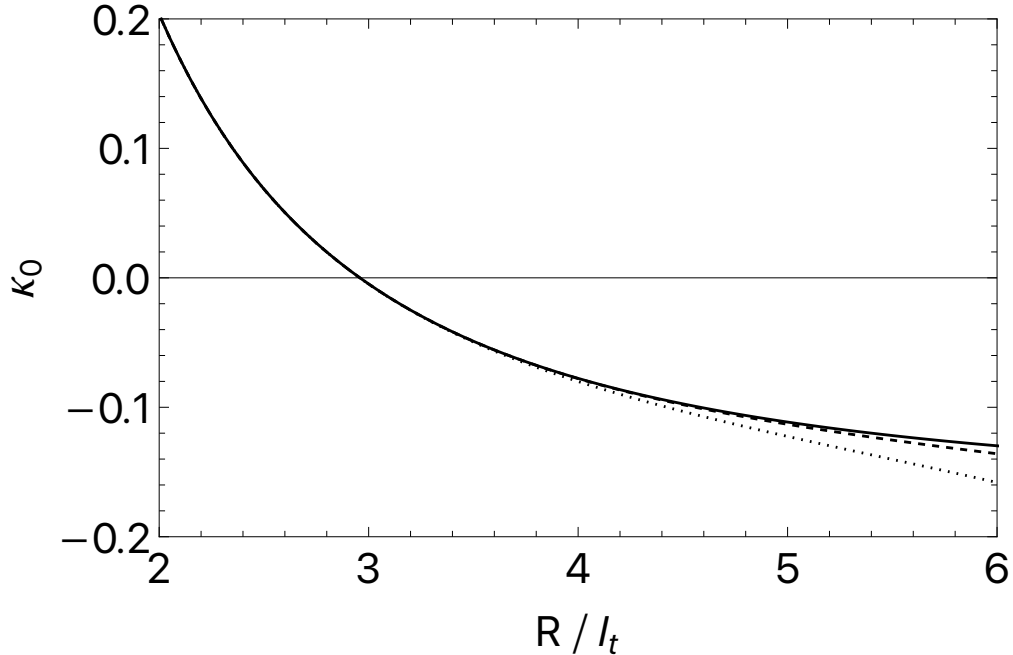


**Figure 2.2.** Typical values of imaginary part  $\kappa_0$  of saddle point.

Similar procedures are employed to express  $g(k)$  as well (for  $C_{\mu,\nu}$ ,  $g = 1$ ). As an example, consider  $\langle B_\mu | B'_\nu \rangle$ , for which  $g(k) = \int_0^\infty dr r^3 e^{ikr^2} u_\mu(r) \frac{\partial u_\nu}{\partial r}(r)$ . Here we approximately expand by least-squares fitting  $\sqrt{u_\mu\left(-\frac{1}{r}\right) \frac{\partial u_\nu}{\partial r}} = \sum_{n=0}^{n_m} C_n \mathcal{B}_n(\sqrt{2}l, 2r_0, r)$  for a different set of coefficients  $C_n$ . The function  $\sqrt{u_\mu\left(-\frac{1}{r}\right) \frac{\partial u_\nu}{\partial r}}$  was chosen because the quantity  $u_\mu\left(-\frac{1}{r}\right) \frac{\partial u_\nu}{\partial r}$  is positive and even. Then  $g(k) = -\int_0^\infty dr r^4 e^{ikr^2} \left(\sqrt{u_\mu\left(-\frac{1}{r}\right) \frac{\partial u_\nu}{\partial r}}\right)^2$ , and a separate analytic expression for  $\int_0^\infty dr e^{ikr^2} r^4 \mathcal{B}_n(l, r_0, r)$  is found and used. In the end, only the ratios of quantities such as  $\frac{C_{\mu\nu}}{\sqrt{C_\mu C_\nu}}$  are needed, so a lot of factors, such as the prefactor  $\frac{1}{N^{3N/2} R^{3N-1}} \left(\frac{NR}{\pi}\right)$ , drop out of the final results.

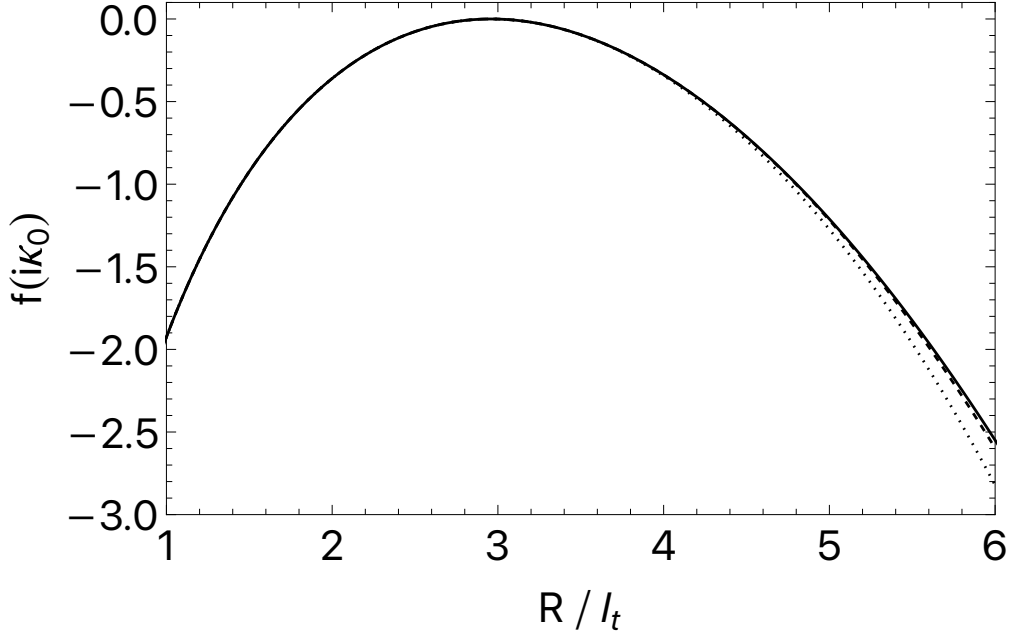


**Figure 2.3.** Typical values of  $f(k) = -ikR^2 + \log I(k)$ ,  $\beta = N$ , at saddle point  $k = i\kappa_0$ .

To illustrate the methods of this section, Figs. 2.2, 2.3, and 2.4, taken from Ref. [45], benchmark the method of steepest descent using a single gaussian orbital  $\frac{2}{\pi^{1/4} \alpha^{3/2}} \exp(-\frac{1}{2} (\frac{r}{\alpha})^2)$ , for which the functions  $I(k)$  and  $f(k)$  can be found analytically. Consider the conditions  $N = 10^4$  and  $a_s = 10^{-2} l_t$ , and take  $\alpha = 2.41529$ , which variationally minimizes the total energy of mean-field Eqn. 2.2. From Ref. [50], all integrals can be done exactly with a gaussian orbital, giving for example  $\frac{C'(R)}{C(R)} = -\frac{2NR}{\alpha^2}$ . Solid curves are the exact results without least-squares fitting. Dotted curves are the results of approximately fitting

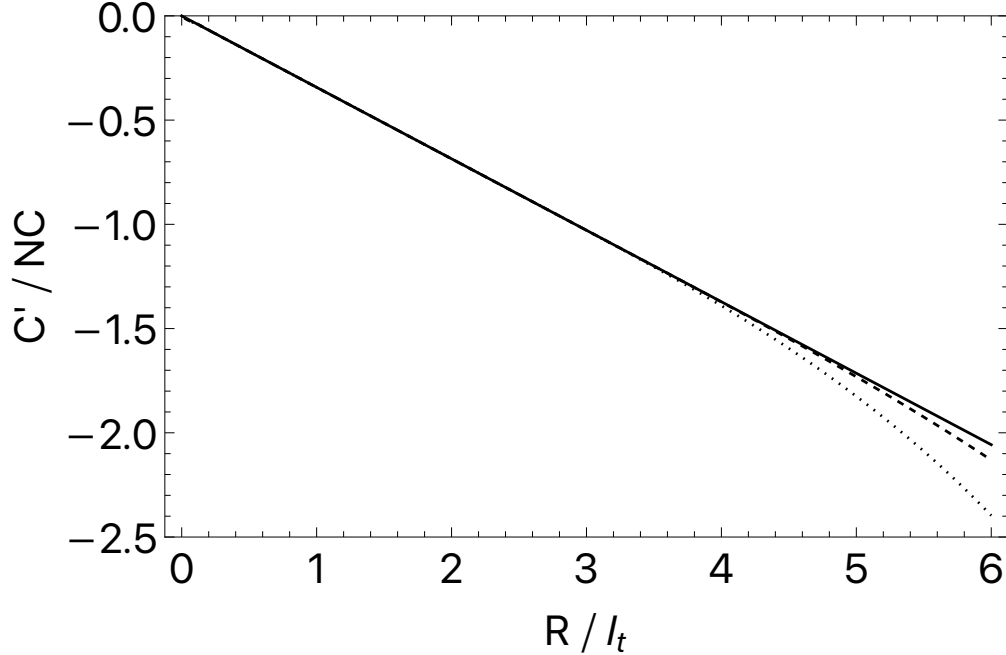


**Figure 2.4.** Example of hyperradial logarithmic derivative of normalization integral  $\frac{C'(R)}{NC(R)}$ .

$u = \sum_{n=0}^{n_m} C_n \mathcal{B}_n(\sqrt{2}l, 2r_0, r)$ , with  $n_m = 25$ ,  $r_0 = 0.16 l_t$ , and  $l = \sqrt{2}r_0$ . Dashed curves are with  $n_m = 50$ ,  $r_0 = 0.1 l_t$ , and  $l = \sqrt{2}r_0$ .

In the neighborhood of the local minimum of variational expectation values  $U(R)$ , which is located at  $R = 2.958 l_t$  for chosen parameters, excellent agreement between exact and approximate results are seen, as well as convergence in terms of the number of fitting functions. Note that  $\kappa_0 \rightarrow \infty$  as  $R \rightarrow 0$  and  $\kappa_0 \rightarrow -\frac{1}{\alpha^2}$  as  $R \rightarrow \infty$  for the exact result. Both  $\kappa_0$  and  $f(i\kappa_0)$  are nearly 0 in the vicinity of  $R = 2.958 l_t$ . As hinted by the shape of  $f(i\kappa_0)$ , plotting  $N^{3N/2} R^{3N-1} C$  (which integrates in  $R$  to 1) results in an extremely sharp peak at the local minimum  $R = 2.958 l_t$ , indicating that the system, in a state represented by the gaussian orbital, is localized at the minimum of K-Harmonic adiabatic potential  $U(R)$  in almost point-like manner.

Some deviations between exact and approximate results are observed at small  $R$ , and a more serious deviation is observed at large  $R$  away from  $2.958 l_t$ . If one wishes to accurately compute  $U(R)$  away from its minimum, more computational effort must be spent to satis-

factorily describe the far-lying tail of the orbital with fitting functions. Even then, since the different integrands in  $k$  are of the form  $e^{Nf(i\kappa_0)}g(k)e^{N(f(k)-f(i\kappa_0))}$ , serious questions remain regarding the accuracy of the method for large values of  $R$  (when  $Nf(i\kappa_0)$  deviates significantly from 0). However, since the method of this chapter can only be expected to describe the ground-state and perhaps a few of the lowest-lying breathing modes of the condensate, we shall remain pleased by the benchmark results of Figs. 2.2, 2.3, and 2.4, and explore the consequences of the formalism in detail in the next chapter.

### 3. ONE-BODY ANSATZ: RESULTS AND DISCUSSION

This chapter explains the results and consequences of the one-body orbital variational ansatz method that was developed in Ch. 2. All figures and tables are taken from Ref. [45], where they were originally published.

Of many possible examples, two prototypical laboratory conditions are explored in particular. The first is for values of  $N$  up to  $10^4$ , with scattering length set to  $a_s = 10^{-2}l_t$ , so that results may be compared naturally with the Thomas-Fermi approximation. The other condition simulates the parameters of Ref. [30], where  ${}^7\text{Li}$  has negative scattering length  $a_s = -27.3a_0$  and the trap is almost spherically symmetric with oscillator length  $l_t = 3.157\mu\text{m}$ , so  $a_s = -4.577 \times 10^{-4}l_t$ .  $N_c = 1257$  is the largest particle number for which Eq. 2.2 has a solution, while the K-Harmonic approximation predicts  $N_c = 1465$  to be the largest  $N$  that supports a local minimum in the adiabatic hyperspherical potential. Ref. [30] actually quotes a wide range of lower experimental estimates for  $N_c$  from 650 to 1300.

As for the notation regarding choice of orbitals,  $\phi_{N_0, a_s}$  is the solution of Eqn. 2.2 with interaction term  $g(N_0 - 1)|\phi|^2\phi$ , if auxiliary parameter  $N_0$  is different from the true physical  $N$ .  $\phi^{GP} = \phi_{N, a_s}$  is the correct Gross-Pitaevskii solution, if it exists. Finally, we also use the bright-soliton orbital  $\phi_l^s = \frac{1}{\sqrt{4\pi}}\sqrt{\frac{12}{\pi^2 l^3}}\text{sech}\left(\frac{r}{l}\right)$  where appropriate. They are relevant and particularly useful when  $a_s < 0$ , by which means we can compute potentials even when no solution of Eqn. 2.2 exists.

#### 3.1 Potentials of Single Mean-Field Orbitals

Fig. 3.1 shows the variational adiabatic potentials  $U(R) - \frac{Q(R)}{2N}$  with non-adiabatic corrections included (see Eqn. 2.11) for scattering length  $a_s = 0.01l_t$  and various values of  $N$ , using the correct numerical solution  $\phi^{GP}$  for each  $N$ . The blue dashed, red dotted, and green solid curves refer to results of single  $\phi^{GP}$  for  $N = 9600, 9800,$  and  $10000$ , respectively. The black circles are the potential for  $N = 9600$  using the K-Harmonic approximation. For the same scattering length, Fig. 3.2 shows the comparison between values of  $E$  obtained from solving the mean-field equation (black circles) and minima of potentials ( $Q$  included) from  $\phi^{GP}$  (blue solid) and from the K-Harmonic approximation (red dashed).

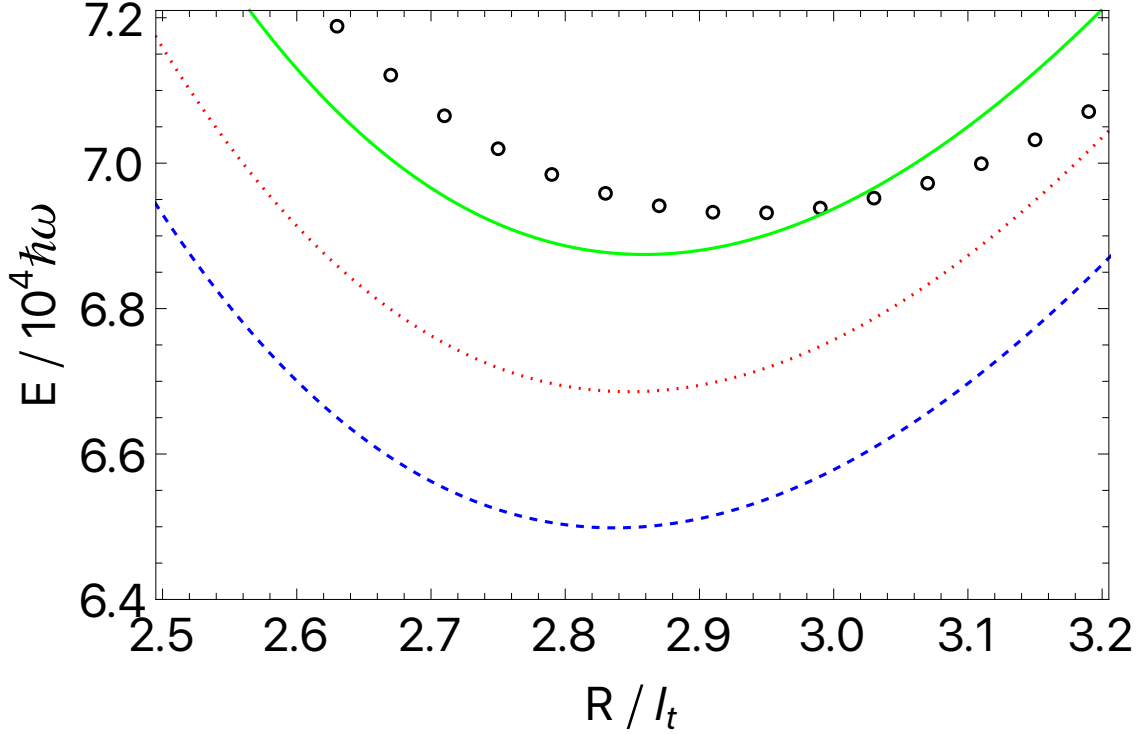


**Figure 3.1.** Adiabatic potentials with  $Q$  included for  $a_s = 0.01 l_t$ , calculated using  $\phi^{GP}$  for  $N = 9600$  (blue dashed), 9800 (red dotted), and 10000 (green solid). The black circles are the K-Harmonic potential for  $N = 9600$ .

Similarly, Fig. 3.3 shows the variational adiabatic potentials with non-adiabatic corrections included for scattering length  $a_s = -4.577 \times 10^{-4} l_t$  and various values of  $N$ . The orange solid, blue dotted, and red dashed curves are calculated using single  $\phi^{GP}$  for  $N = 1197, 1227$ , and 1257, respectively. The black circles are computed from the K-Harmonic approximation for  $N = 1257$ . For the same negative scattering length, Fig. 3.4 shows the comparison between values of  $E$  obtained from solving Eqn. 2.2 (black circles) with the extrema of variational hyperspherical potentials ( $Q$  included). Blue solid and dashed curves are minima and maxima obtained from single  $\phi^{GP}$ . Orange dotted and dash-dotted curves are minima and maxima obtained from the K-Harmonic approximation.

In all cases shown here, the non-adiabatic correction  $Q(R)$  was negligible, its contribution too small to be seen in the scales of figures, justifying the use of root-mean-square radius  $R$  as a slowly-varying parameter. At large  $R$ , the variational adiabatic potentials are dominated by the external trap scaling as  $R^2$ . At smaller  $R$ , the main contributions come from repulsive

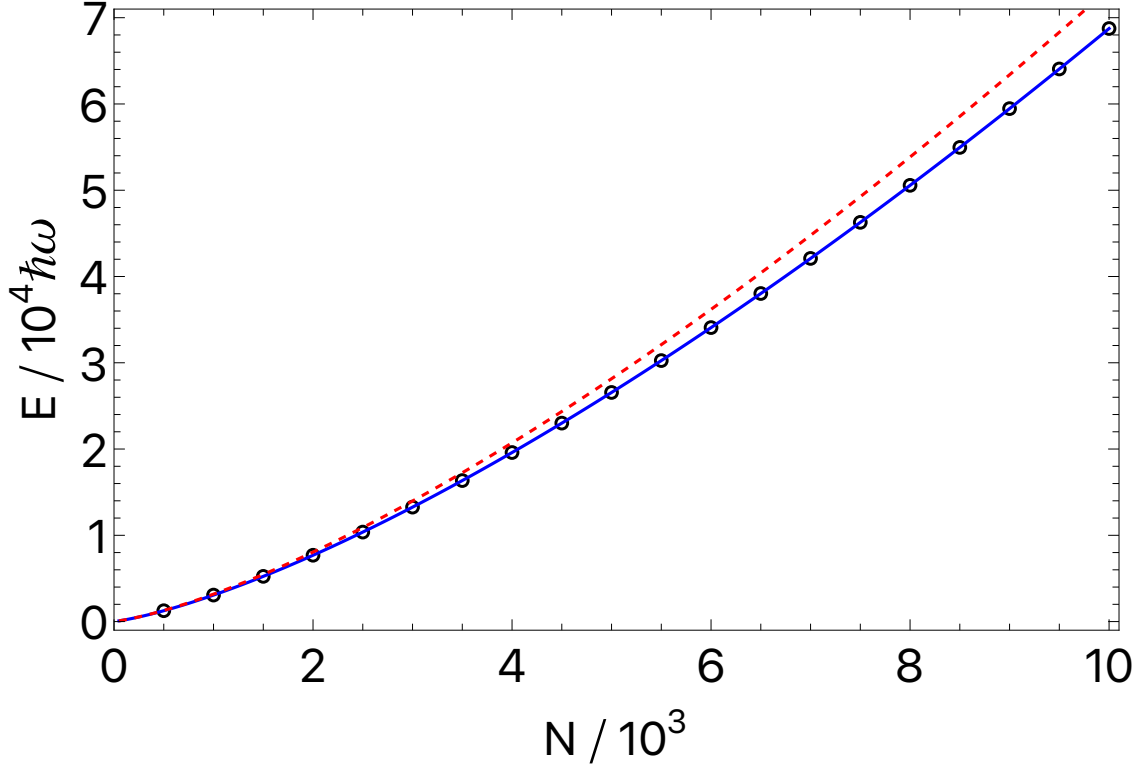


**Figure 3.2.** Numerically minimized mean-field energy  $E_0(N)$  (black circles) compared with the minima of adiabatic potentials (Q included) calculated using  $\phi^{GP}$  (blue solid) and using the K-Harmonic approximation (red dashed), for  $a_s = 0.01 l_t$ .

“mock” centrifugal term proportional to  $\frac{(3N-1)(3N-3)}{4R^2}$  and from the interaction term; in the K-Harmonic approximation, the interaction term is strictly proportional to  $R^{-3}$ . When  $a_s > 0$ , both centrifugal and interaction terms are repulsive; when  $a_s < 0$ , the two terms compete, with the interaction term winning at very small  $R$ .

Note in Figs. 3.1 and 3.3 how  $\phi^{GP}$  minimizes the local minimum of the variational hyperspherical potential far better than the K-Harmonic approximation does. As  $N$  increases, so does the value of the local minimum; consistent with the trend in changing shapes of mean-field orbital  $\phi^{GP}$ , the location of minimum is pushed outward with increasing  $N$  when  $a_s > 0$ , while it is pulled inward with increasing  $N$  when  $a_s < 0$ .

In Fig. 3.3, the height of the local maximum that temporarily protects the metastable condensate from collapse steadily decreases with increasing  $N$ . There is a great difference in barrier height between the K-Harmonic ( $\Delta E = 188.99 \hbar\omega$ ) and single- $\phi^{GP}$  ( $\Delta E = 47.87 \hbar\omega$ )

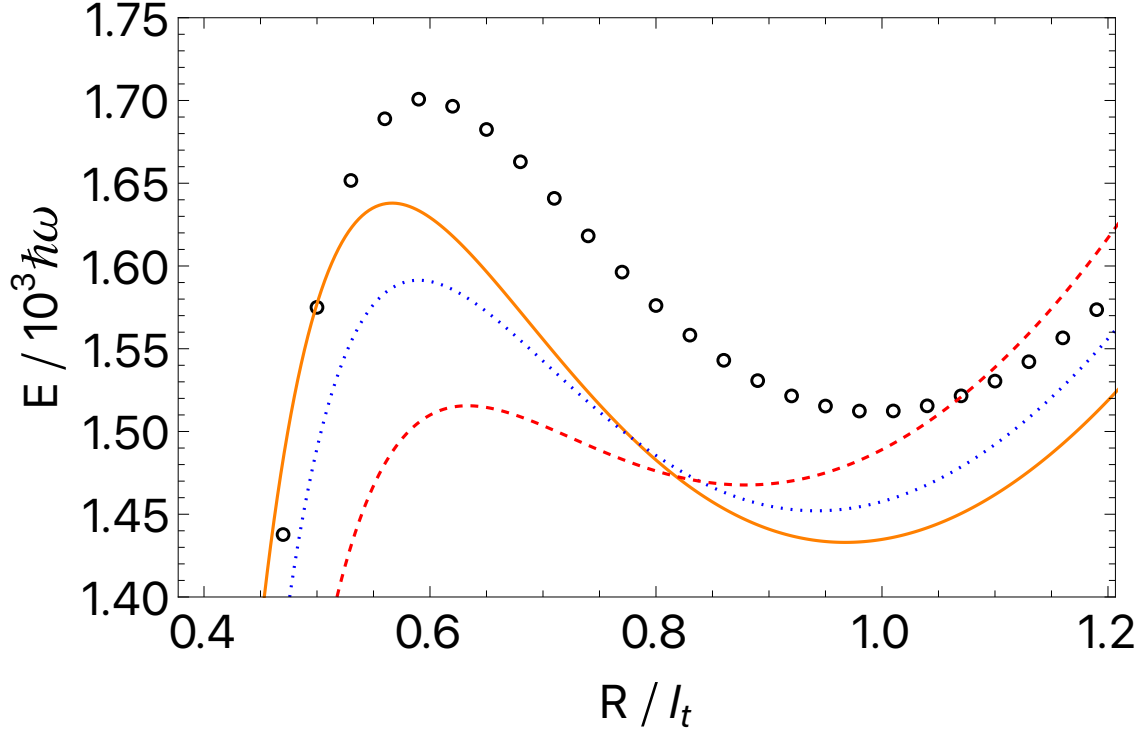


**Figure 3.3.** Adiabatic potentials with  $Q$  included for  $a_s = -4.577 \times 10^{-4} l_t$ , calculated using  $\phi^{GP}$  for  $N = 1197$  (orange solid), 1227 (blue dotted), and 1257 (red dashed). The black circles are the K-Harmonic potential for  $N = 1257$ .

models for  $N = 1257$ , consistent with the over-estimation of  $N_c$  by a gaussian orbital. However, quite surprisingly, there still is quite a large barrier in the potential computed from  $\phi^{GP}$  for  $N = 1257$ , even though criticality has been reached according to the mean-field equation so one would have expected the barrier vanish.

Figs. 3.2 and 3.4 show once again that K-Harmonic approximation significantly over-estimates the ground-state energy of the many-particle system, while results from  $\phi^{GP}$  are consistent with mean-field predictions. The minima of potentials from  $\phi^{GP}$  are slightly lower than mean-field energies; though the difference is too small to be seen in the scale of the figures, the discrepancy is consistent with the notion of vibrational zero-point energy that arises when the hyperradial equation 2.11 is solved. In Fig. 3.4, the maximum of potential obtained from  $\phi^{GP}$  has almost merged with the minimum at  $N = 1257$ , though not quite as discussed earlier.

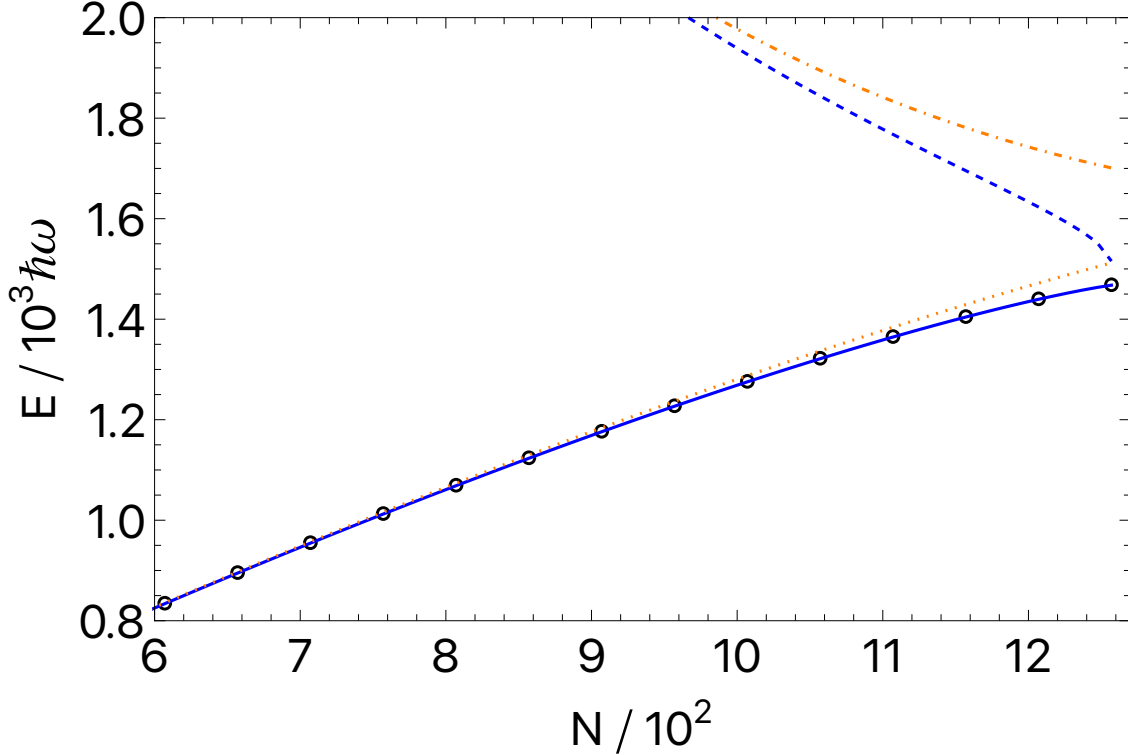


**Figure 3.4.** Numerically minimized mean-field energy  $E_0(N)$  (black circles) compared with the extrema of adiabatic potentials (Q included), for  $a_s = -4.577 \times 10^{-4} l_t$ . Blue solid and dashed curves are minima and maxima from  $\phi^{GP}$ . Orange dotted and dash-dotted curves are minima and maxima from K-Harmonic approximation.

### 3.2 Excitation Frequencies from Single Mean-Field Orbitals

Having observed the general topology of the variational potentials and the agreement with mean-field theory in terms of ground-state energies, we now investigate the lowest few excitation frequencies. The current hyperspherical formalism is only able to describe the monopole modes of zero angular momentum.

Figs. 3.5 and 3.6 show the comparison of results from Bogoliubov Equation 2.3, K-Harmonic approximation, and single  $\phi^{GP}$  calculations. In the limit of very small  $N$ , all results reduce to the non-interacting limit of  $\Delta E_n = 2n\hbar\omega$  for zero angular momentum trap states. In Fig. 3.5 concerning positive  $a_s$ , the Bogoliubov predictions converge at large  $N$  to the Thomas-Fermi limit [34] of  $\Delta E_n = \hbar\omega\sqrt{2n^2 + 3n}$ ; therefore the first excitation energy is predicted to be greater than the non-interacting limit, while higher excitation energies

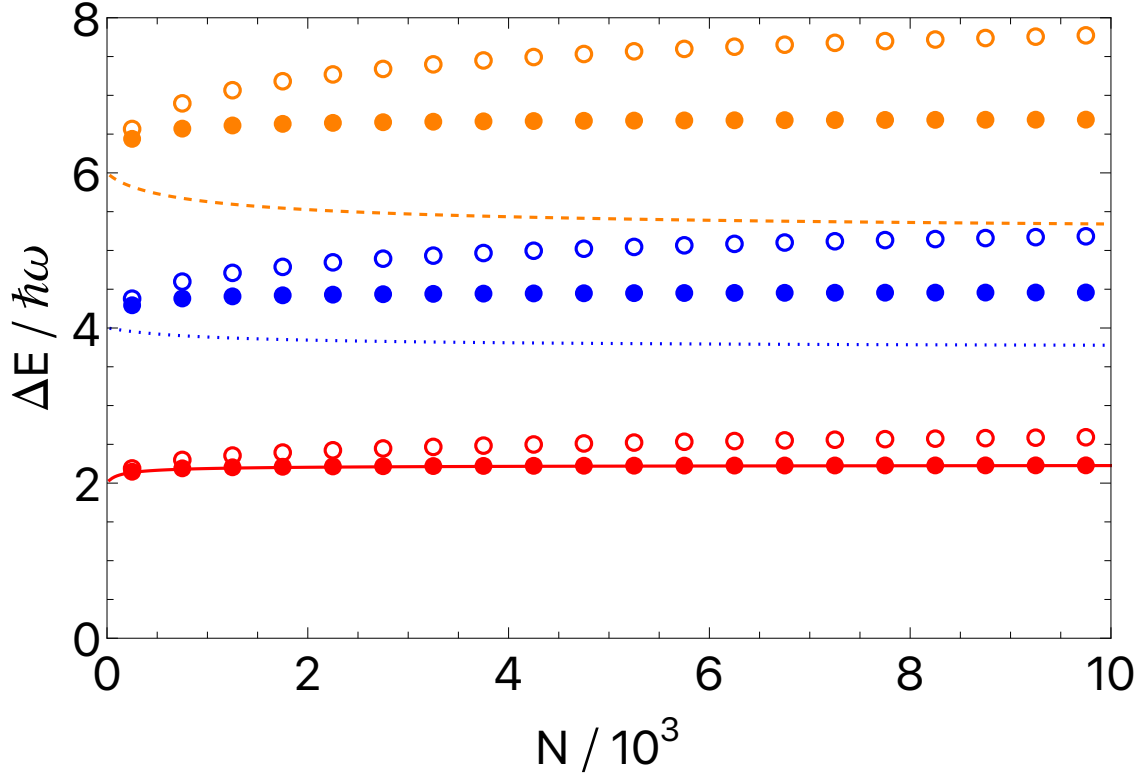


**Figure 3.5.** The first 3 (red, blue, orange) excitation energies  $E_i - E_0$  for  $a_s = 0.01 l_t$  and varying  $N$ . Solid, dotted, and dashed curves are the Bogoliubov predictions, while solid circles are from the K-Harmonic approximation. Open circles are the results of single- $\phi^{GP}$  calculations.

are supposed to be smaller than the non-interacting limit. The K-Harmonic approximation, obtained by solving Eqn. 2.11 with the potential of Ref. [50], predicts all excitation frequencies to increase with  $N$ , though it agrees quite well with the Bogoliubov theory for the first excited state. Somewhat surprisingly and disappointingly, the results of variational potential energies obtained using a single  $\phi^{GP}$  orbital are even worse than the predictions of K-Harmonic approximation. It indicates that, though the orbital  $\phi^{GP}$  minimizes the minimum of the adiabatic potential well, it performs poorly in minimizing the potential away from the minimum, resulting in a “tight” potential with overestimated excitation energies. Most likely,  $\phi^{GP}$  alone is not enough to sufficiently describe the many-body correlations and fluctuations.

In Fig. 3.6, both  $\phi^{GP}$  and the K-Harmonic approximation predict that the excitation frequencies decrease with increasing  $N$ . The frequencies from  $\phi^{GP}$  decay faster due to lower

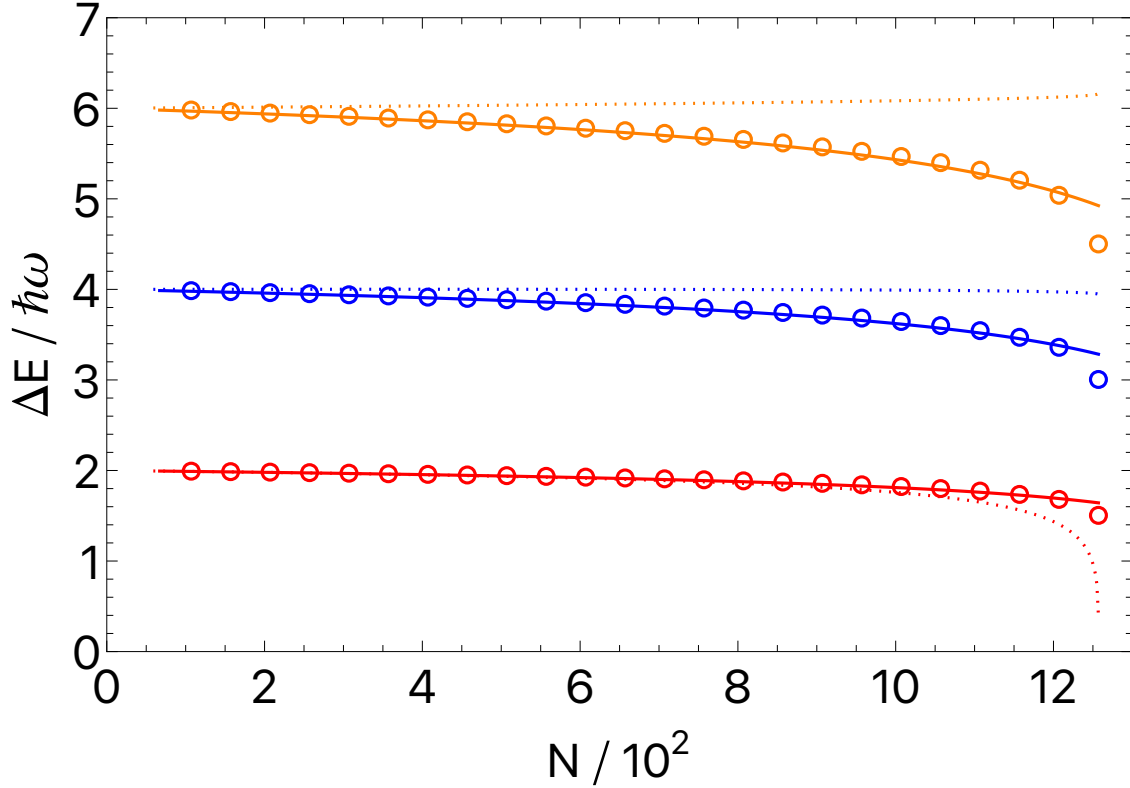


**Figure 3.6.** The first 3 (red, blue, orange) excitation energies  $E_i - E_0$  for  $a_s = -4.577 \times 10^{-4} l_t$  and varying  $N$ . Dotted curves are the Bogoliubov predictions, while solid curves are from the K-Harmonic approximation. Circles are from single- $\phi^{GP}$  calculations.

barrier height, as seen in Fig. 3.3. Note that higher excited states decay faster than the first excited state; given a sufficiently low barrier, there is a limit to the number of metastable wave functions that one can solve for using Eqn. 2.11. On the other hand, Bogoliubov theory predicts that only the first excitation energy decays as  $N$  approaches critical number  $N_c$ , while third and higher excitation energies actually *increase*. The first excitation energy of Bogoliubov theory decays faster than that from single  $\phi^{GP}$  calculation. It will be seen in a later section that by using multiple orbitals, the barrier height of potential seen in Fig. 3.3 will reduce tremendously, so there will be better agreement with the Bogoliubov prediction as a result.

### 3.3 Multi-Orbital Calculations, Repulsive Interaction

Fig. 3.7 shows results of implementing the multi-orbital ansatz formalism for 10,000 bosons with  $a_s = 10^{-2} l_t$ . Circles are calculated from only  $\phi^{GP}$ , while triangles and squares are obtained by single orbital calculations, with orbitals obtained for values of  $N_0$  lower and greater than the correct  $N$  in the mean-field equation. As expected,  $\phi^{GP}$  is superior to all other orbital in minimizing the minimum of the variational potential, but interestingly, other choices of orbitals do perform better in minimization away from the local minimum.

These observations provide strong motivation for coupling such different (yet similar-looking) orbitals together and performing a limited diagonalization procedure. Red solid curve is from coupling 3 different orbitals; no linear dependence between the orbitals was

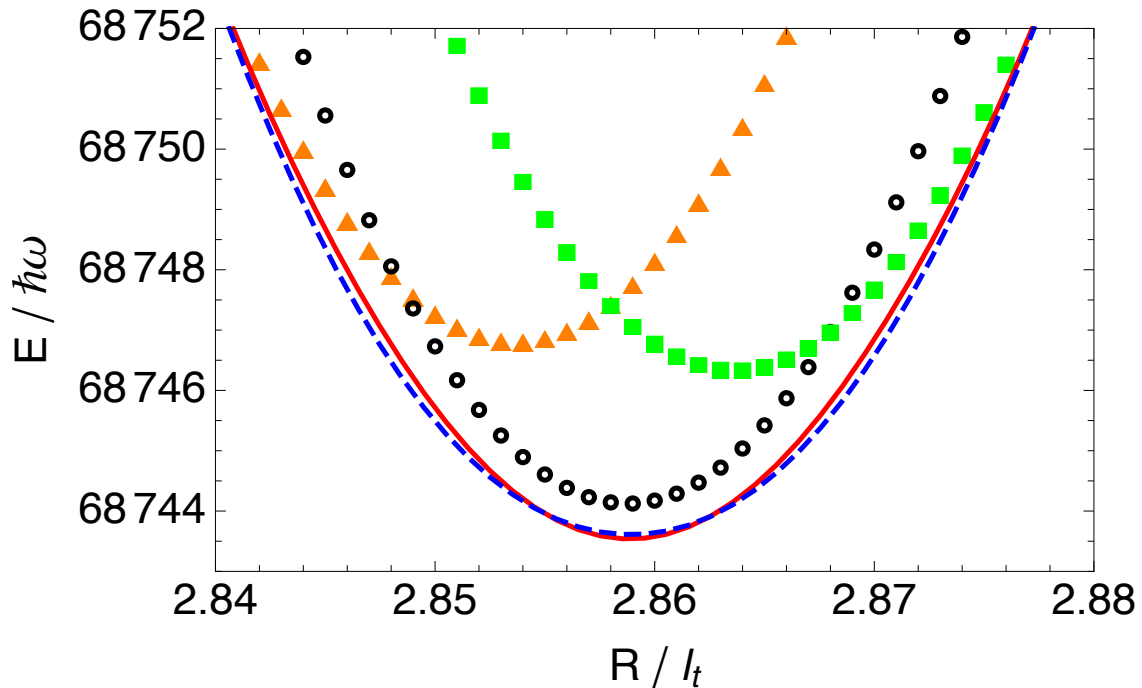


**Figure 3.7.** Adiabatic potentials with  $Q$  included for  $10^4$  bosons with  $a_s = 10^{-2} l_t$ . The orange triangles, black circles, and green squares are single  $\phi_{N_0, a_s}$  results with  $N_0 = 9600.04, 10^4$ , and  $10399.96$ . The red solid curve is the lowest primitive eigenvalue from coupling 3 orbitals with  $N_0 = 9800.02, 10^4$ , and  $10199.98$ , with no eigenstate of  $\underline{Q}$  removed. The blue dashed curve is the lowest reduced eigenvalue from coupling 5 orbitals with  $N_0 = 9600.04, 9800.02, \dots, 10399.96$ , with 1 eigenstate of  $\underline{Q}$  removed.

**Table 3.1.** List of ground state  $E_0$  and excitation  $\Delta E$  (units of  $\hbar\omega$ ) from solving Eq. 2.11 with different  $U(R) - \frac{Q(R)}{2N}$ , for  $N = 10^4$  and  $a_s = 10^{-2} l_t$ .  $n$  is the number of coupled orbitals, and  $\delta = n - c$  is the number of eigenstates of  $\underline{Q}$  thrown away. The orbitals  $\phi_{N_0, a_s}$  are identified by values of  $N_0 = N_{0,1} + (i - 1)\Delta N_0$ ,  $i = 1, \dots, n$ .

type	$(n, \delta)$	$(N_{0,1}, \Delta N_0)$	$E_0$	$\Delta E$
K-Har.	(1,0)	n.a.	73346.48	2.23, 4.46, 6.69
$\phi^{GP}$	(1,0)	n.a.	68745.42	2.59, 5.19, 7.78
$\phi_{N_0, a_s}$	(3,0)	(9800.02, 199.98)	68744.71	2.32, 4.60, 6.84
$\phi_{N_0, a_s}$	(5,0)	(9500.05, 249.975)	68744.52	2.30, 4.55, 6.77
$\phi_{N_0, a_s}$	(5,1)	(9600.04, 199.98)	68744.69	2.19, 4.43, 6.68
$\phi_{N_0, a_s}$	(5,2)	(9800.02, 99.99)	68744.71	2.32, 4.59, 6.83

observed. On the other hand, coupling 5 nodeless orbitals with similar shapes did lead to linear dependence; one of the eigenstates of the overlap matrix had to be removed, and the result is seen as a blue dashed curve. There is little difference between the two diagonalized results; it is of little avail to add more and more orbitals to the coupled calculations because linear dependence issues force us to remove more and more linear combinations, defeating the purpose. At any rate, the coupled orbital calculations do lead to lower minimum and broader curvature than single  $\phi^{GP}$  calculations.

Using Eqn. 2.11, we may now solve for hyperradial eigenstates on top of these coupled potentials, and Table 3.1 summarizes the result. Compared to only using  $\phi^{GP}$ , significant lowering of the hyperradial state energies is now observed from multi-orbital calculations, but the excitation frequencies are mostly still higher than what the Bogoliubov theory gives. Actually, for  $(n, \delta) = (5, 1)$  and  $(N_{0,1}, \Delta N_0) = (9600.04, 199.98)$ , the first excitation energy is lower than the corresponding Bogoliubov prediction. It is not fully understood how the variational minimization of  $U(R)$  tends to convergence with different  $B(R, \Omega)$ , or whether it even converges at all. In Ref. [66], standard configuration-interaction (CI) calculations (not fixing the hyperradius) using the pseudopotential have been shown to fail to converge in the absolute sense. In any case, the hyperspherical CI method assumes that each term of the wavefunction is a simple product of orbitals, which is a very strong limitation on

the subspace of Hilbert space that the many-body system occupies, possibly explaining the discrepancies with the Bogoliubov predictions.

### 3.4 Multi-Orbital Calculations, Attractive Interaction

We finally turn our attention to calculating with multiple orbitals when scattering length is negative.

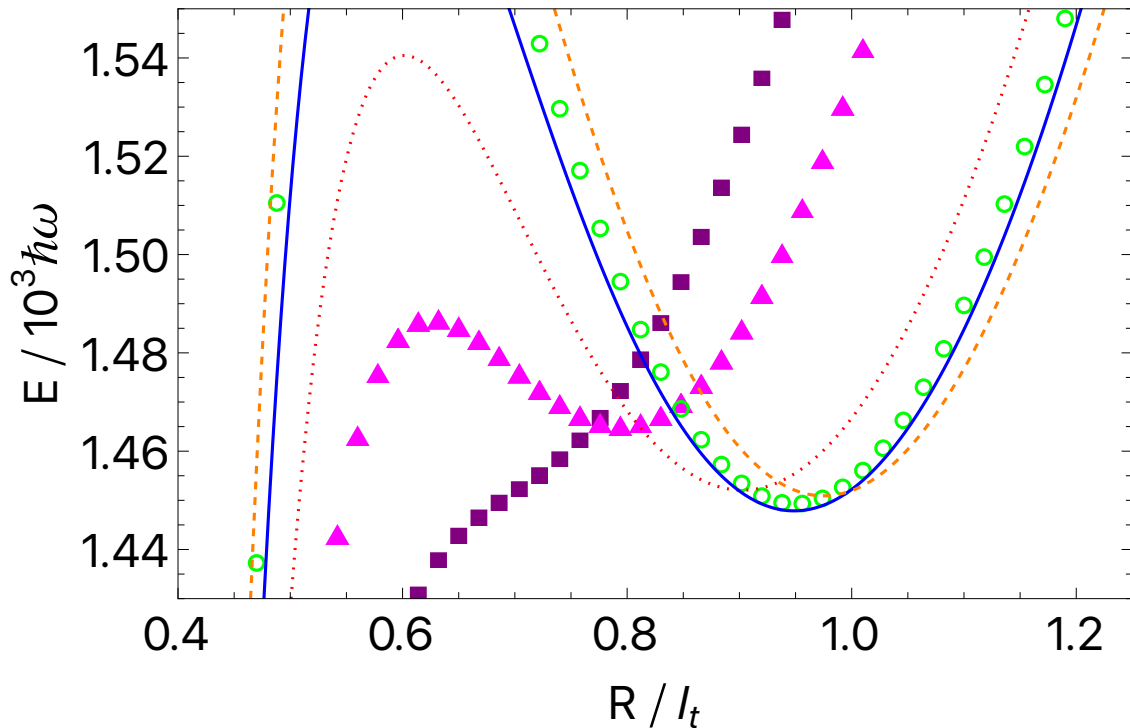


**Figure 3.8.** Adiabatic potentials with  $Q$  included for  $a_s = -4.577 \times 10^{-4} l_t$  and  $N = 1220$ ; all are single-orbital results. Orange dashed, blue solid, and red dotted curves are from  $\phi_{N_0, a_s}$  with  $N_0 = 1112.41, 1220,$  and  $1257.1$ . Purple squares, magenta triangles, and green circles are from  $\phi_l^s$  with  $l = 0.38, 0.43,$  and  $0.64 l_t$ .

Keeping in mind that for the situation of Ref. [30], the mean-field equation numerically predicts the critical number for  $a_s = -4.577 \times 10^{-4} l_t$  to be  $N_c = 1257$ , Figs. 3.8 and 3.9 show various single-orbital calculations using different types of orbitals for  $N = 1220$  and  $N = 1300$ , respectively. In Fig. 3.8, amongst the different kinds of numerical orbitals one can obtain from Eqn. 2.2 using different auxiliary parameter  $N_0$ , indeed  $\phi^{GP}$  (the correct

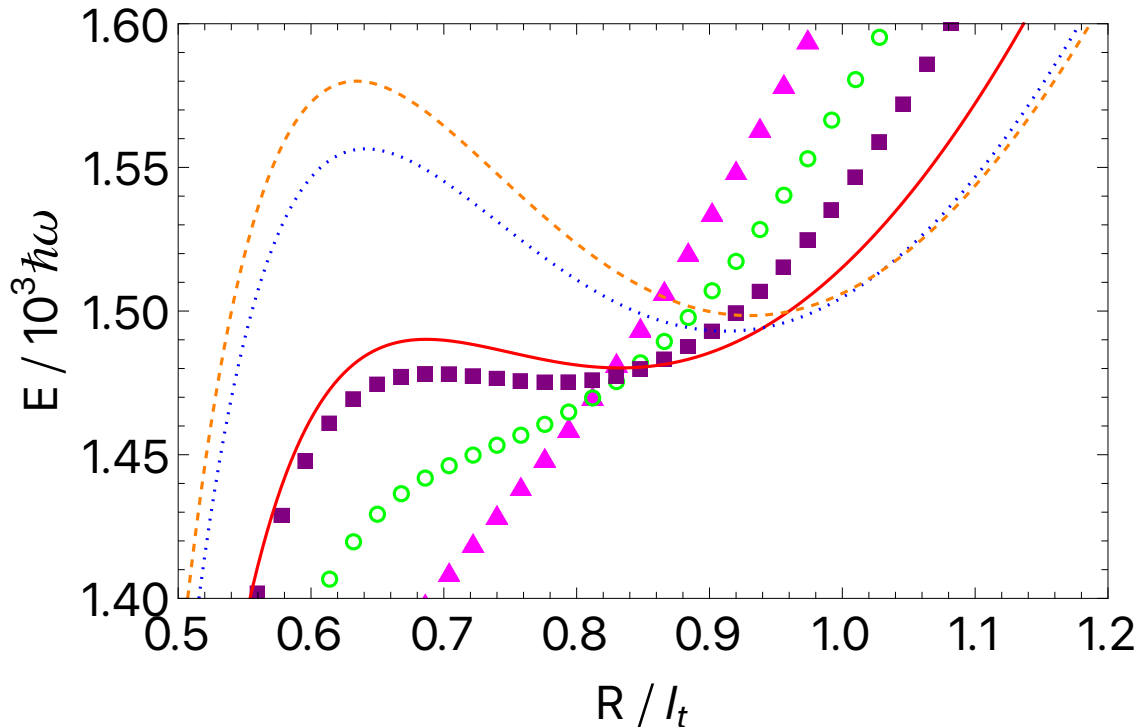


**Figure 3.9.** Adiabatic potentials with  $Q$  included for  $a_s = -4.577 \times 10^{-4} l_t$  and  $N = 1300$ ; all are single-orbital results. Orange dashed, blue dotted, and red solid curves are from  $\phi_{N_0, a_s}$  with  $N_0 = 1149.27, 1203.19,$  and  $1257.12$ . Magenta triangles, green circles, and purple squares are from  $\phi_l^s$  with  $l = 0.38, 0.43,$  and  $0.48 l_t$ .

solution for  $N = 1220$ , giving blue curve) does the best job in minimizing the local minimum of metastable condensate potential. Note now that a bright soliton orbital of length scale  $l = 0.64 l_t$  gives a potential curve that closely follows the blue curve, but when we calculate using a different soliton orbital of smaller  $l = 0.38 l_t$ , simulating a situation where the condensate happens to be more squeezed in, a completely different curve (purple squares) is obtained in which there is no local minimum. Then, if we were to perform a coupled calculation using several of these orbitals, we should obtain a curve that roughly traces out which orbital happens to give the lowest variational value at each  $R$ , consequently leading to much lower local maximum protecting the condensate.

Similarly, Fig. 3.9 shows single-orbital calculations for  $N = 1300$ . There is no  $\phi^{GP}$  for this scenario, making the soliton orbitals particularly useful for analysis. Auxiliary parameter  $N_0 = 1257.12$  is the largest it can be so that mean-field Eqn. 2.2 admits a numerical

solution; its results are shown as a red curve. If we only had access to orbitals of form  $\phi_{N_0, a_s}$ , we would mistakenly have concluded that  $N = 1300$  still somehow supports a metastable condensate (remember that the K-Harmonic approximation predicts  $N_c = 1465$ ), but the different soliton results, particularly for  $l = 0.38 l_t$  (magenta triangles), make it clear that the true correct potential curve has no local minimum to support a metastable condensate.

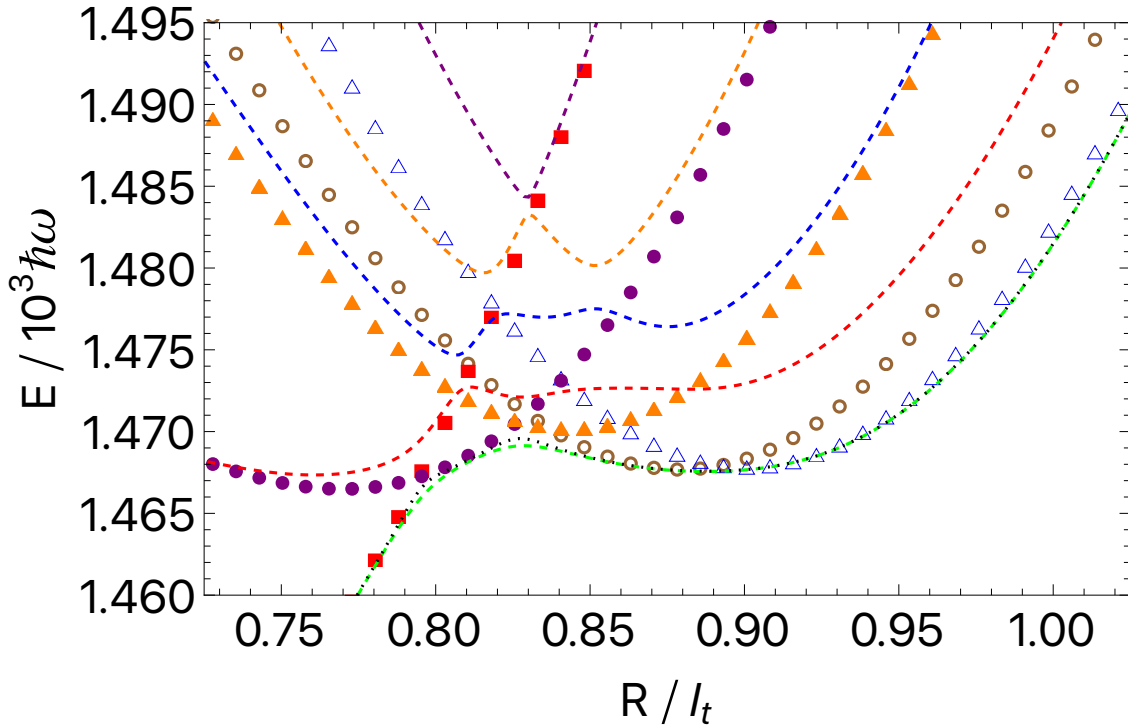


**Figure 3.10.** Adiabatic potentials for  $N = 1257$ ,  $a_s = -4.577 \times 10^{-4} l_t$ . Open brown circles and open blue triangles are  $U$  with  $Q$  included from single  $\phi_{N_0, a_s}$ , with  $N_0 = 1257$  and  $1251.51$ . Red squares, purple filled circles, and orange filled triangles are  $U$  with  $Q$  included from single  $\phi_l^s$  with  $l = 0.39, 0.44$ , and  $0.49 l_t$ . The 5 (green, red, blue, orange, and purple) dashed curves are the primitive generalized eigenvalues  $U$ , *without*  $Q$ , from coupling the above 5 orbitals. The dotted black curve *includes*  $Q$  for the lowest eigenvalue.

Examine now some of the single-particle results for  $N = 1257$  in Fig. 3.10, for which the mean-field equation says criticality of attractive condensate has been met. Once again,  $\phi^{GP}$  does the best job in minimizing the local minimum of metastable condensate; it gives the open brown circles here (the same as the red dashed curve of Fig. 3.3, which predicts a barrier height of  $\Delta E = 47.87 \hbar\omega$ ). Similar to Fig. 3.8, soliton results (red squares) hint

at much lower barrier height for the true potential. Using the 5 orbitals which give the 5 different single-orbital results of Fig. 3.10, we now couple these orbitals and obtain 5 generalized eigenvalues from Eqn. 2.23. The 5 orbitals are sufficiently distinguishable from one another that no linear dependence was detected. The 5 colored dashed curves of Fig. 3.10 give the 5 generalized eigenvalues *without* non-adiabatic correction  $Q$ , while the black dotted curve is the lowest generalized eigenvalue *with*  $Q$  included.

Fig. 3.10 is the only figure of this chapter in which the contributions of non-adiabatic correction are explicitly shown, as single-orbital calculations consistently gave negligible non-adiabatic values. The difference between the green dashed and black dotted curves is noticeable but quite small, so the adiabatic formalism is still applicable. Not shown are the higher generalized eigenvalues with  $Q$ ; the non-adiabatic correction gave very high peaks at every avoided crossing between the dashed curves, indicating breakdown of adiabatic theory.

The most important conclusion of Fig. 3.10 is that the barrier protecting the metastable condensate is much, much lower for the coupled potential (dotted black) than it is for the single- $\phi^{GP}$  potential (open brown circles), now only about  $2\hbar\omega$ . Clearly, adding more orbitals and thereby doing a better job accounting for the many-body correlations is necessary for a partially satisfactory theory of metastable condensates. The single-orbital theory would have predicted the critical number  $N_c$  to be far higher than what the mean-field theory predicts, even if the orbital used happens to be the solution of the mean-field equation; the coupled-orbital potential is now more consistent with the mean-field theory. We take the dotted black curve as black circles of Fig. 3.11 and solve for hyperradial eigenstates  $F(R)$  using Eqn. 2.11. Because the variational potential diverges as  $R^{-3}$ , the problem of Eqn. 2.11 is not well defined for range of  $R$  all the way to 0 (infinitely many nodes will appear), so a cutoff must be introduced; Fig. 3.11 chose cutoff  $R_c = 0.75 l_t$ .

States such as the magenta curve of Fig. 3.11 show up, strongly dependent on the choice of  $R_c$ , indicating collapsed states. Other states, such as the green and orange curves, do show up above the value of local minimum and below the maximum, but they also depend strongly on the value of  $R_c$ , indicating that they are fast-decaying shape resonances if they can even be taken seriously. On the other hand, the red curve with  $E = 1468.08\hbar\omega$  does appear to be mostly stable with varying  $R_c$ , indicating a credible shape resonance for the metastable

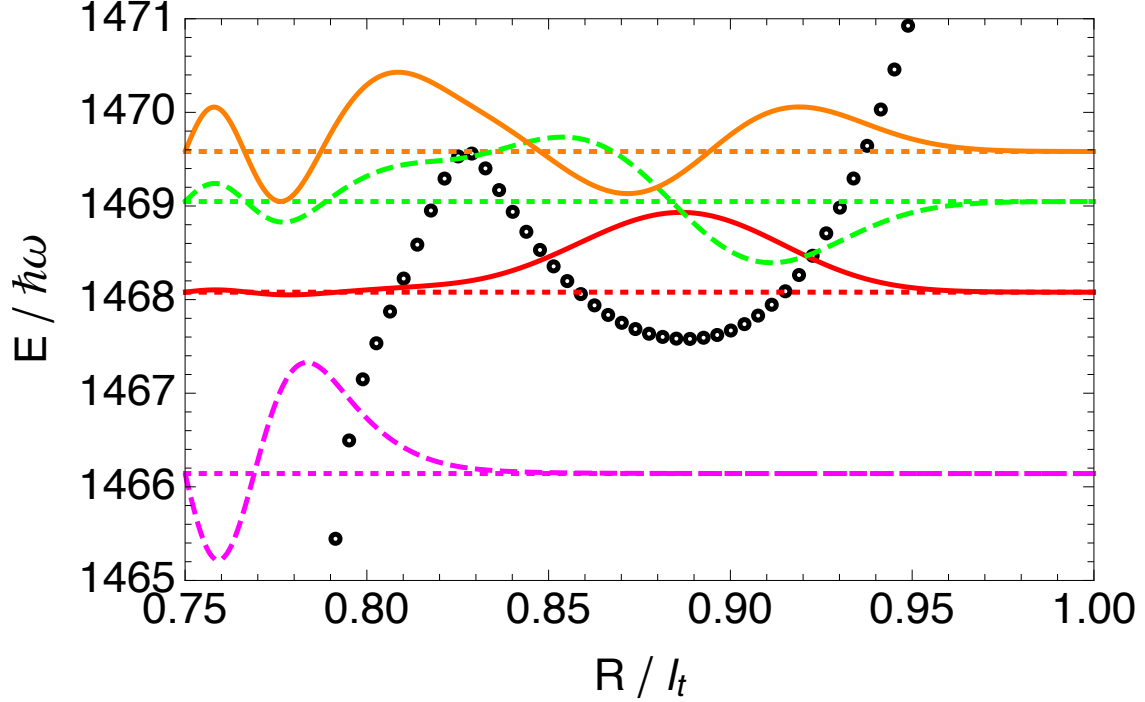


**Figure 3.11.** Hyperradial eigenstates  $F(R)$  for  $N = 1257$  and  $a_s = -4.577 \times 10^{-4} l_t$  from solving Eqn. 2.11. The potential, represented by black circles here, is the dotted black curve of Fig. 3.10. Boundary condition  $F(R_c) = 0$  at  $R_c = 0.75 l_t$  is chosen. Dotted lines denote the eigenenergies; solid and dashed curves are the corresponding wavefunctions  $F(R)$  (scaled arbitrarily). Magenta denotes a collapsed state outside the minimum well; red denotes a metastable state, while green and orange denote rapidly decaying states.

condensate. Using WKB, we estimate the tunneling lifetime for macroscopic collapse of this metastable state to be  $0.43 s$ ; using Siegert pseudostates [67], we approximate the lifetime to be roughly  $0.5 s$ .

If we are to take the state represented by the green curve of Fig. 3.11 seriously, then the difference in energy between the red and green states is about  $1\hbar\omega$ . Therefore, the first excitation frequency is lower than what the single- $\phi^{GP}$  theory predicts (see very last red circle at the bottom right of Fig. 3.6) in better agreement with the Bogoliubov prediction. But our results with the variational hyperspherical potentials cast some doubts on the validity of the Bogoliubov approximation for the second and higher excited states. Imagine a coupled-orbital potential for  $N = 1220$ , similar to the black dotted curve of Fig. 3.10, by examining the single-orbital curves of Fig. 3.8. Such a potential would have a barrier much higher

than that for  $N = 1257$ , supporting many metastable states. But as one increases  $N$ , the barrier will decrease, and the number of metastable states will decrease as a result. This physical picture is inconsistent with Bogoliubov theory, which places no limits on the number of eigenvalues of Eqn. 2.3 as  $N \rightarrow N_c$  (there are as many eigenvalues as there are orbitals in the basis), with higher excitation frequencies *increasing* as  $N$  increases.

### 3.5 Summary and Outlook

Using some choice of one independent-particle orbital ansatz, or some linear combination of such orbitals, we have successfully computed the variational adiabatic hyperspherical potentials of many bosons in a spherically-symmetric trap with zero total angular momentum. The  $3N - 1$  hyperangular degrees of freedom have been treated by a reformulation in terms of a one-dimensional complex integral, with method of steepest descent applied to handle the fast oscillations that come about as a result of large particle number. A mechanism was formulated to handle any linear dependence between orbitals if it does appear.

The single-orbital calculations, using the correct numerical solution to the mean-field Gross-Pitaevskii equation given particle number  $N$  and scattering length  $a_s$  with respect to oscillator length  $l_t$ , have been shown to minimize the local minimum of the variational potential for the Bose-Einstein condensate better than any other choice of orbital. In particular, remarkable improvement over the standard K-Harmonic approximation has been achieved in minimizing the many-body ground-state energy in agreement with mean-field theory. However, fundamental disagreements between the methods of this dissertation and Bogoliubov theory on collective monopole excitation frequencies have been observed for  $a_s > 0$ , most likely because our simple, restricted choice of ansatz does not sufficiently capture the complex many-body correlations.

A coupled many-orbital calculation did not sufficiently lower the values of excitation frequencies when  $a_s > 0$ , with persistent discrepancies from the Bogoliubov predictions, but using a combination of numerical and bright soliton orbitals, a significant reduction in barrier height of variational potential has been observed for  $a_s < 0$ . Somewhat surprisingly, even when we use the solution of the mean-field equation as the ansatz, that orbital alone gives a

variational potential with barrier far higher than that implied by mean-field theory. Several coupled orbitals, on the other hand, do reduce the barrier to a value consistent with the prediction of critical condensate number  $N_c$  from mean-field theory, with tunneling lifetime approximately  $0.5s$  for the conditions of Ref. [30].

Direct and straightforward extensions of the work of Ch. 2 and this chapter are available for the future, mainly in terms of using mean-field orbitals with non-zero angular momentum for condensate vortices, and in terms of breaking spherical symmetry for applications in quasi-1D and quasi-2D settings. However, there are several apparent issues with the methods presented here. The first is that the current method obviously breaks down for unitary Bose gas with very large scattering length, for which a regularized pseudopotential [22] would probably have to be used instead. The other is that, due to the zero-range nature of the pseudopotential, not only does the variational potential collapse with behavior  $R^{-3}$  for  $a_s < 0$ , but it is not clear whether the potential can even converge at all for finite  $R$  (along the lines of Ref. [66]). Finally, within spherical symmetry, a trap is required to obtain a sensible solution of the mean-field equation to use as an ansatz orbital, hence we may not decouple the results of variational calculations from the spherical trap and cannot investigate the large- $R$  asymptotic behavior of the hyperspherical potential within the current limitations of this theory. Therefore, we take a step back to more modest number of particles and explicitly construct a completely different ansatz that takes pair-wise correlations into account in Ch. 4 and 5, for which finite-range numerical two-body interactions may be used and for which a unitary Bose gas can be studied quite naturally.

## 4. TWO-BODY ANSATZ: INTRODUCTION AND METHOD

### 4.1 Introduction to Physics of Few Bosons

To obtain ideas on how to construct reasonable two-body ansatz functions, we now review the main results of adiabatic hyperspherical theory as it was originally applied to few particles. The idea of choosing a collective coordinate, the *hyperradius*, as a slowly-varying parameter and calculating an effective potential energy at each fixed hyperradius in a way similar to Born-Oppenheimer approximation was originally introduced by Macek [68] in the context of autoionizing states of helium. Macek defined the hyperradius  $R = \sqrt{r_1^2 + r_2^2}$  in terms of the two electron coordinates and solved the electronic Schrödinger equation at each fixed  $R$ . At large  $R$ , each adiabatic potential energy channel can be classified as either one electron bound and the other ionized, or both ionized, making  $R$  a natural coordinate to study the bound and continuum states of two electrons at once.

Since then, the adiabatic hyperspherical formalism has particularly grown as a favorite theoretical toolkit in the context of neutral ultracold atoms. In this context, with the center-of-mass degrees of freedom separated out, the hyperradius is proportional to  $\sum_{i<j}^N r_{i,j}^2$ , where  $r_{1,2}$  is the distance between particles 1 and 2. For instance, with three atoms, each adiabatic hyperspherical potential channel can be classified at large hyperradius as describing either all three particles unbound from each other, or a dimer (two bound atoms) and a free atom.

The hyperspherical formalism is well-suited for describing the intriguing phenomenon of Efimov trimers (molecules made of three atoms). Efimov first predicted [69] that at a two-body resonance (in other words, when a dimer is formed right at zero energy), an infinite number of trimers can be formed, each related to another by a peculiar geometric scaling. At large but finite negative scattering length, when the interaction is too weak to support a dimer, there still may be a large (but finite) number of trimers (called Borromean states).

Observe Fig. 4.1, taken from Ref. [70], which sketches the energies of two neighboring trimers labeled by indices  $n$  and  $n + 1$ . Within the hyperspherical formalism, it turns out [70], [71] that when  $|a_s| \rightarrow \infty$  (corresponding to the central vertical axis of Fig. 4.1), the lowest adiabatic hyperspherical potential is given by  $\frac{\hbar^2}{2mN} \left( \frac{-s_0^2 - 1/4}{\rho^2} \right)$ , where  $s_0 \approx 1.00624$  and



If the adiabatic hyperspherical potential maintains the form  $\frac{\hbar^2}{2mN} \left( \frac{-s_0^2 - 1/4}{\rho^2} \right)$  all the way to  $\rho = 0$ , as zero-range theory would imply, Eqn. 4.1 says there is not a well-defined ground state with energy  $E^{(0)}$  but a collapse to  $E \rightarrow -\infty$ , known as a “Thomas collapse” [72], but calculations with realistic finite-range potentials [73] do set a well-defined ground-state trimer, from which excited trimer energies can be deduced by Eqn. 4.1. The value of the first trimer energy, dependent on the particular two-body potential under consideration, is referred to in the literature as “setting a three-body parameter”.

For finite values of  $a_s < 0$ , the hyperspherical potential [74] exhibits a barrier and transitions to a repulsive potential for  $\rho \gg a_s$ , and for finite  $a_s > 0$ , the potential converges to a dimer threshold below  $E = 0$  at large  $\rho$ , so there will not be an infinite number of trimers as a result. Fig. 4.1 sketches a series of negative scattering length  $a_-^{(n)}$  where the  $n$ -th trimer first appears. Ref. [75] was the first experimental evidence of Efimov trimers, more than 30 years after Efimov’s original predictions. By sweeping through a range of scattering lengths using magnetic Feshbach resonance, the experimentalists detected a large enhancement of three-body recombination when  $a_s$  hit one value of  $a_-^{(n)}$ . Then three free atoms approaching each other become coupled to an excited Efimov trimer, quickly decaying into a deeply bound dimer and a free atom and energetically leaving the system.

Concerning the computation of adiabatic hyperspherical potentials of three particles, zero-range theories [7], [70] using the regularized pseudopotential (see Eqn. 1.6) often decompose the wave function into a pairwise form:  $\Phi(\rho; \Omega) = \sum_{i < j}^N \phi(\rho; r_{i,j})$ . This is called a *Faddeev decomposition* [76], [77]. In such theories, though the function  $\phi$  appears to only depend on a particular pair of particles, it is calculated by taking the influence of all  $N$  particles. A curious set of papers [78], [79] attempt to generalize the Faddeev decomposition for more than 3 particles and have claimed that an attractive  $1/\rho^2$  potential emerges for many-particle systems as well; if true, then Efimov physics for more than 3 particles would be observed. These results do not seem to be consistent with Ref. [80] that shows that  $(N - 1)$ -body resonance does not lead to an infinite number of  $N$ -body bound states when  $N > 3$ , nor to numerical results of four bosons [81] that will be discussed later, but they

did provide a motivation to try to formulate a different two-body numerical ansatz to study more than 3 bosons in this dissertation.

In contrast to a sum symmetrization of Faddeev, one may consider a product-symmetrized wave function instead, an idea that goes back to Jastrow [82]. Jastrow wave functions are frequently used in computational chemistry to handle electron correlation in Quantum Monte Carlo methods, for example [83]. A paper [84] attempted to calculate the adiabatic hyperspherical potentials by a product symmetrization of functions depending on  $r_{i,j}$  using Bethe-Peierls boundary condition, though rather aggressive approximations have been made due to difficulties in computation. We shall also consider product symmetrization when able in this dissertation.

Moving away from zero-range theories, for  $N = 3$ , adiabatic hyperspherical potentials can be computed fruitfully in terms of Smith-Whitten hyperangles (see Appendix C), in which the problem is recast into a coupled partial differential equation in two dimensions [73], [85], [86]. One highlight of such approach is the notion of Van der Waals universality [87]. One may compute the adiabatic hyperspherical potential using different strengths of two-body interaction that admit correspondingly more and more dimers but the same scattering length. One would think that deeper two-body Van der Waals potentials should lead to deeper minimum of lowest hyperspherical potential and hence set a different three-body parameter, but large non-adiabatic corrections compensate for the stronger two-body interaction and give rise to similar three-body parameters.

Because there are  $3N - 4$  hyperangular degrees of freedom that one must account for, obtaining results for 4 particles has been difficult, but a breakthrough was achieved in terms of *correlated gaussian* basis sets [59]–[61]. A milestone discovery for 4 bosons [81] is that, attached to each hyperspherical potential that converges to an Efimov trimer threshold, two related tetramer (4-body) bound states (or resonances when the associated trimer is an excited state) are found.

Finally, in the interest of extending the successes of adiabatic hyperspherical method to more particles, Diffusion Monte Carlo methods [88], [89] have been successfully applied to realistic atomic two-body interactions to compute the lowest adiabatic hyperspherical potential that converges to a cluster (in other words, not to a scattering continuum where

all  $N$  particles are unbound). Though the methods cannot be used to compute excited hyperspherical potential curves, these works promise some form of viability in tackling the problem of more than 4 bosons; we are therefore motivated to formulate ansatz approaches to describe the continuum channels of several bosons within the hyperspherical framework.

## 4.2 Method of Two-Body Ansatz

### 4.2.1 $N$ -Body Hamiltonian with Center-of-Mass Removed

Once again, we start with  $N$  identical spin-less (or spin-polarized) bosons, interacting via short-range two-body potential energies and possibly under a spherically symmetric trap. After we separate out the center-of-mass degrees of freedom and define the  $N - 1$  relative Jacobi vectors as described in Appendix A, the Hamiltonian looks as follows:

$$H_{CM} = -\frac{\hbar^2}{2mN}\nabla_{CM}^2 + \frac{1}{2}mN\omega^2 R_{CM}^2, \quad (4.2)$$

$$H = -\frac{\hbar^2}{2m}\sum_{k=1}^{N-1}\nabla_{\eta_k}^2 + \frac{1}{2}m\omega^2\sum_{k=1}^{N-1}\eta_k^2 + \sum_{i<j}^N V(r_{i,j}). \quad (4.3)$$

In this dissertation, we consider in particular two types of different finite-range interactions. One is a gaussian potential of form  $V(r_{i,j}) = \left(\frac{\hbar^2}{mr_0^2}\right)\alpha\exp\left(-\left(\frac{r_{i,j}}{r_0}\right)^2\right)$ , with a dimensionless parameter  $\alpha$  that characterizes the interaction strength. The other is a soft-core Van der Waals interaction of form  $V(r_{i,j}) = -\frac{C_6}{r_{i,j}^6 + \sigma^6} = -\left(\frac{\hbar^2}{ml_{vdw}^2}\right)\left(\frac{16l_{vdw}^6}{r_{i,j}^6 + \sigma^6}\right)$ . An auxiliary parameter  $\sigma > 0$  has been introduced to cut off the collapse near origin and determine the number of dimers, while  $l_{vdw} = \frac{1}{2}\left(\frac{mC_6}{\hbar^2}\right)^{1/4}$  is a Van der Waals length, giving a typical finite length-scale of the interaction.

Next, we define the *relative* hyperradius  $\rho = \left[\frac{1}{N}\sum_{k=1}^{N-1}\eta_k^2\right]^{1/2}$ . As discussed in Appendix A,  $\rho^2 = \frac{1}{N^2}\sum_{i<j}^N r_{i,j}^2$ ; there is a clear geometrical meaning to the hyperradius as giving a measure of the overall size of the  $N$ -particle system through the various two-body distances. This relative hyperradius  $\rho$  is related to the hyperradius  $R = \left[\frac{1}{N}\sum_{i=1}^N r_i^2\right]^{1/2}$  of Ch. 2 (defined *without* removing the center-of-mass) by the relation  $\rho^2 = R^2 - R_{CM}^2$ .

We transform the coordinate system from a Cartesian system of vectors  $\vec{\eta}_1, \dots, \vec{\eta}_{N-1}$  to  $(\rho, \Omega)$ , with  $3N - 4$  hyperangles summarily represented by  $\Omega$ . Then the relative Hamiltonian is now written:

$$H = -\frac{\hbar^2}{2mN} \left( \frac{1}{\rho^{(3N-4)/2}} \frac{\partial^2}{\partial \rho^2} \rho^{(3N-4)/2} \right) + \frac{\hbar^2}{2mN} \left( \frac{(3N-4)(3N-6)}{4\rho^2} \right) + \frac{1}{2}mN\omega^2\rho^2 + H_{ad}, \quad (4.4)$$

$$H_{ad} = \frac{\hbar^2}{2mN} \left( \frac{\Lambda^2}{\rho^2} \right) + \sum_{i<j}^N V(r_{i,j}). \quad (4.5)$$

The term proportional to  $\frac{(3N-4)(3N-6)}{4\rho^2}$  is a ‘‘mock’’ centrifugal potential, originating as a result of eliminating a first-derivative term in  $\rho$  for future convenience. The *adiabatic* (fixed-hyperradius) Hamiltonian  $H_{ad}$  is composed of an angular-momentum-like term proportional to  $\frac{\Lambda^2}{\rho^2}$  and all pairwise interactions.  $\Lambda^2$  is a ‘‘grand angular momentum operator’’ with eigenfunctions  $Y_{\lambda,\mu}(\Omega)$  (see Appendix B).

Let bra-ket notation indicate a hyperangular integration with fixed hyperradius,  $\langle \psi_a | \psi_b \rangle = \int d\Omega \psi_a \psi_b$ , with real functions. In principle, at each fixed hyperradius, there exists a complete, orthonormal set of eigenfunctions of the adiabatic Hamiltonian:  $H_{ad}\phi_\mu(\rho; \Omega) = U_\mu(\rho)\phi_\mu(\rho; \Omega)$ . Then, expanding the total wave function as  $\Psi_\nu = \sum_\mu \frac{F_{\nu,\mu}(\rho)}{\rho^{(3N-4)/2}} \phi_\mu(\rho; \Omega)$ , the Schrödinger Equation becomes (exactly with no approximation here):

$$-\frac{\hbar^2}{2mN} F''_{\nu,\mu}(\rho) + \left[ U_\mu(\rho) + \frac{\hbar^2}{2mN} \left( \frac{(3N-4)(3N-6)}{4\rho^2} \right) - \frac{\hbar^2}{2mN} Q_{\mu,\mu} + \frac{1}{2}mN\omega^2\rho^2 \right] F_{\nu,\mu}(\rho) - \frac{\hbar^2}{2mN} \sum_{\mu' \neq \mu} \left[ 2P_{\mu,\mu'} F'_{\nu,\mu'}(\rho) + Q_{\mu,\mu'} F_{\nu,\mu'}(\rho) \right] = E_\nu F_{\nu,\mu}(\rho), \quad (4.6)$$

$$P_{\mu,\mu'} = \left\langle \phi_\mu \left| \frac{\partial}{\partial \rho} \right| \phi_{\mu'} \right\rangle, \quad Q_{\mu,\mu'} = \left\langle \phi_\mu \left| \frac{\partial^2}{\partial \rho^2} \right| \phi_{\mu'} \right\rangle. \quad (4.7)$$

The complicated system of  $N$  interacting particles in  $(3N-3)$ -dimensional space has been reduced to coupled ordinary differential equations in a single coordinate. Quite often, the off-diagonal terms of derivative coupling matrices  $\underline{P}$  and  $\underline{Q}$  can be neglected to an excellent

adiabatic approximation, in which the various channels  $\mu$  may be regarded as decoupled from each other. However, this formalism is very difficult to implement in many cases, simply from the technical challenges of computing the channel functions  $\phi_\mu$  in the first place. This dissertation is therefore concerned with choices of *ansatz* for channel functions.

Suppose then that there is a (real) function  $\Phi_\mu(\rho; \Omega)$  that one may hope to reasonably approximate an actual channel function  $\phi_\mu$ . Write the total wave function as  $\Psi_{\nu, \mu} = \frac{F_{\nu, \mu}(\rho)}{\rho^{(3N-4)/2}} \frac{\Phi_\mu(\rho; \Omega)}{\sqrt{C_\mu(\rho)}}$ , where  $C_\mu(\rho) = \langle \Phi_\mu | \Phi_\mu \rangle$  is a hyperangular normalization integral. Then, the Schrödinger Equation of such a wave function, upon projection of  $\Phi_\mu$ , becomes as follows:

$$-\frac{\hbar^2}{2mN} F''_{\nu, \mu}(\rho) + \left[ U_\mu(\rho) + \frac{\hbar^2}{2mN} \left( \frac{(3N-4)(3N-6)}{4\rho^2} \right) - \frac{\hbar^2}{2mN} Q_\mu(\rho) + \frac{1}{2} mN \omega^2 \rho^2 \right] F_{\nu, \mu}(\rho) = E_{\nu, \mu} F_{\nu, \mu}(\rho), \quad (4.8)$$

$$U_\mu(\rho) = \frac{\langle \Phi_\mu | H_{ad} | \Phi_\mu \rangle}{C_\mu} = \left( \frac{\hbar^2}{2mN\rho^2} \right) \frac{1}{C_\mu} \langle \Phi_\mu | \Lambda^2 | \Phi_\mu \rangle + \left( \frac{1}{C_\mu} \right) \sum_{i < j}^N \langle \Phi_\mu | V(r_{i,j}) | \Phi_\mu \rangle, \quad (4.9)$$

$$Q_\mu(\rho) = \left\langle \frac{\Phi_\mu}{\sqrt{C_\mu}} \left| \frac{\partial^2}{\partial \rho^2} \right| \frac{\Phi_\mu}{\sqrt{C_\mu}} \right\rangle = \left( \frac{C'_\mu}{2C_\mu} \right)^2 - \left( \frac{1}{C_\mu} \right) \left\langle \frac{\partial \Phi_\mu}{\partial \rho} \left| \frac{\partial \Phi_\mu}{\partial \rho} \right\rangle. \quad (4.10)$$

Note an application of the variational principle here, that the quantity  $U_\mu$  begotten from any particular ansatz  $\Phi_\mu$  must be an upper bound on the lowest adiabatic eigenvalue:

$$\frac{\langle \Phi_\mu | H_{ad} | \Phi_\mu \rangle}{C_\mu} \geq U_0^{exact}(\rho) = \langle \phi_0 | H_{ad} | \phi_0 \rangle. \quad (4.11)$$

A finite value for the lowest adiabatic eigenvalue must exist for any  $\rho > 0$ , for a finite-range two-body interaction that is considered here. Furthermore, because the space of hyperangles is finite (for example, a typical Delves hyperangle  $\beta$  has range  $[0, \frac{\pi}{2}]$  in Appendix B), the adiabatic eigenvalue problem is in essence a bound-state problem (in other words, does not lead to a continuum of channel functions). Hence, one may optimistically search

for several different ansatz functions  $\Phi_\mu$ , each approximating one discrete channel function  $\phi_\mu$  out of many.

#### 4.2.2 $J^\pi = 0^+$ Symmetrized Hyperspherical Harmonics

Next, we consider how to construct reasonable ansatz for channel functions that describe  $N$  bosons. We restrict our attention to *zero* total orbital angular momentum and even parity, summarized by symbol  $J^\pi = 0^+$ . This must be the symmetry of the ground state of  $N$  bosons, bound or unbound, and also the symmetry of common Bose-Einstein condensates produced in laboratories; hence, it is the most accessible and promising symmetry for probing with a variational calculation.

First, examine how to construct some (but not all) fully-symmetrized hyperspherical harmonics  $Y_{\lambda,\mu}(\Omega)$  (see Appendix B for definitions of hyperspherical harmonics and Delves hyperangles) of symmetry  $J^\pi = 0^+$ . Imagine first a function  $\phi(r_{1,2})$  that only depends on the distance between particles 1 and 2. Then the action of grand angular momentum operator  $\Lambda^2$  on  $\phi(r_{1,2})$  is to differentiate only in terms of Delves hyperangle  $\beta_1$  (recall that  $r_{1,2} = \sqrt{2N}\rho \cos \beta_1$ ):

$$\begin{aligned} \Lambda^2 \phi(r_{1,2}) &= - \left( \frac{1}{\cos^2 \beta_1 \sin^{3N-7} \beta_1} \right) \frac{\partial}{\partial \beta_1} \left( \cos^2 \beta_1 \sin^{3N-7} \beta_1 \frac{\partial \phi}{\partial \beta_1}(r_{1,2}) \right) \\ &= \nu(\nu + 3N - 5) \phi(r_{1,2}). \end{aligned} \tag{4.12}$$

For an arbitrary number  $\nu$ , there are two different solutions to this eigenvalue equation, written in terms of Gauss hypergeometric function  ${}_2F_1$  [3], [90]:

$$\begin{aligned}
f_1 &= {}_2F_1\left(-\frac{\nu}{2}, \frac{\nu + 3N - 5}{2}, \frac{3N - 6}{2}, \sin^2 \beta_1\right) \\
&= \left(\frac{1}{\cos \beta_1}\right) {}_2F_1\left(\frac{-\nu - 1}{2}, \frac{\nu + 3N - 6}{2}, \frac{3N - 6}{2}, \sin^2 \beta_1\right), \tag{4.13}
\end{aligned}$$

$$\begin{aligned}
f_2 &= {}_2F_1\left(-\frac{\nu}{2}, \frac{\nu + 3N - 5}{2}, \frac{3}{2}, \cos^2 \beta_1\right) \\
&= \left(\frac{1}{\sin^{3N-8} \beta_1}\right) {}_2F_1\left(\frac{\nu + 3}{2}, \frac{-\nu - 3N + 8}{2}, \frac{3}{2}, \cos^2 \beta_1\right). \tag{4.14}
\end{aligned}$$

The function  $f_1$  is irregular (*i.e.* diverges) at  $\beta_1 = \frac{\pi}{2}$ , while  $f_2$  is irregular at  $\beta_1 = 0$ . To kill the divergence, one must choose  $\nu = 2n, n = 0, 1, \dots$ , in which case both  $f_1$  and  $f_2$  are proportional to a Jacobi polynomial  $P_n^{\left(\frac{3N-8}{2}, \frac{1}{2}\right)}(\cos 2\beta_1) = P_n^{\left(\frac{3N-8}{2}, \frac{1}{2}\right)}\left(\frac{r_{1,2}^2}{N\rho^2} - 1\right)$ .

Note now that any particle pair may be labeled (1, 2) instead, and hence the following set of functions must be *some* (but emphatically not all) of symmetrized hyperspherical harmonics of symmetry  $J^\pi = 0^+$ :

$$\Lambda^2 Y_n(\Omega) = (2n)(2n + 3N - 5)Y_n(\Omega), \tag{4.15}$$

$$Y_n(\Omega) = \sum_{i < j}^N P_n^{\left(\frac{3N-8}{2}, \frac{1}{2}\right)}\left(\frac{r_{i,j}^2}{N\rho^2} - 1\right). \tag{4.16}$$

These functions must have symmetry  $J^\pi = 0^+$  because they are rotationally invariant and invariant under parity operator. Notice that  $n = 1$  is forbidden here, because  $Y_1(\Omega) = 0$  (this can be shown by noting that  $\rho^2 = \frac{1}{N^2} \sum_{i < j}^N r_{i,j}^2$ ). This *does not prove* that  $\nu = 2$  is a forbidden eigenvalue for  $N$  non-interacting bosons of symmetry  $J^\pi = 0^+$ ; it merely says that, should  $\nu = 2$  symmetrized hyperspherical harmonics exist, it cannot be expressed in terms of  $Y_n(\Omega)$ . See Appendix D for an explicit proof that  $n = 1$  is forbidden for  $N = 3$ . Appendix D also shows that, up to  $n = 5$ , the functions  $Y_n(\Omega)$  are the correct nondegenerate symmetrized hyperspherical harmonics, and that the first two-fold degeneracy occurs for  $n = 6$ , for which  $Y_6(\Omega)$  is one of two eigenfunctions.

### 4.2.3 Construction of Explicit Two-Body Ansatz

Having examined the structure of the non-interacting eigenstates of the adiabatic Hamiltonian  $H_{ad}$ , now we consider how they might be modified by the two-body interaction.

Begin by examining the adiabatic eigenvalue equation that one wishes he could solve:

$$H_{ad} \phi_\mu(\rho; \Omega) = \left[ \frac{\hbar^2}{2mN} \left( \frac{\Lambda^2}{\rho^2} \right) + \sum_{i < j}^N V(r_{i,j}) \right] \phi_\mu(\rho; \Omega) = U_\mu(\rho) \phi_\mu(\rho; \Omega). \quad (4.17)$$

First, in order to apply the tools of scattering theory to the adiabatic hyperspherical potentials  $U(\rho)$ , one is typically interested in asymptotic behavior of the potentials at large  $\rho$ . We restrict ourselves to two-body interactions with some finite range  $r_0$ , decaying faster than  $r^{-3}$  so that the s-wave scattering length is well-defined. When  $\rho \gg r_0$ , then  $V(r_{i,j})$  is negligible except for very small parts of hyperangular space (called *coalescence regions*).

Furthermore, for typical dilute gaseous systems in experiments, one might suppose that as 2 particles interact with each other, the other  $N - 2$  particles are all far away from everyone else and act as “spectators”, to a first-order approximation. Hence, suppose for a moment that a channel function may be replaced by a function that only depends on  $r_{1,2}$ :

$$\begin{aligned} \left[ \frac{\hbar^2}{2mN} \left( \frac{\Lambda^2}{\rho^2} \right) \right] \phi(r_{1,2}) &= \left[ \frac{\hbar^2}{2mN} \left( \frac{\nu(\nu + 3N - 5)}{\rho^2} \right) \right] \phi(r_{1,2}) = - \left( \frac{\hbar^2}{2mN\rho^2} \right) \\ &\times \left( \frac{1}{\cos^2 \beta_1 \sin^{3N-7} \beta_1} \right) \frac{\partial}{\partial \beta_1} \left( \cos^2 \beta_1 \sin^{3N-7} \beta_1 \frac{\partial \phi}{\partial \beta_1}(r_{1,2}) \right), \quad r_{1,2} \gg r_0. \end{aligned} \quad (4.18)$$

Solutions to this equation for *a priori* undetermined  $\nu$  are given by the functions  $f_1$  and  $f_2$  of Equations 4.13 and 4.14.  $f_2$  is inappropriate because there is no physical reason why the wave function should diverge as  $\beta_1 \rightarrow 0$ , as  $r_{1,2}$  becomes very large. However,  $f_1$  is sensible because it has precisely the divergent behavior that one expects an s-wave function to have:  $f(r) \approx C \left( 1 - \frac{a_s}{r} \right)$ .

Next, as  $r_{1,2}$  approaches  $r_0$ , one must take  $V(r_{1,2})$  into account. In the limit  $r_{1,2} \rightarrow 0$ , the operator  $\frac{\Lambda^2}{2N\rho^2}$  approaches the form  $-\frac{1}{r^2} \frac{d}{dr} \left( r^2 \frac{d}{dr} \right)$ , familiar in two-body radial Schrödinger

Equation. Therefore, we approximate  $\phi(r_{1,2})$  as a zero-energy scattering wave function under the influence of  $V(r_{1,2})$ , as one typically assumes when using Fermi pseudopotential:

$$-\frac{\hbar^2}{mr_{1,2}^2} \frac{d}{dr_{1,2}} \left( r_{1,2}^2 \frac{d\phi}{dr_{1,2}}(r_{1,2}) \right) + V(r_{1,2})\phi(r_{1,2}) = 0, \quad r_{1,2} < r_0. \quad (4.19)$$

In summary, the following is how the two-body ansatz function  $\phi(r_{1,2})$  is constructed when fixed hyperradius is much larger than range  $r_0$  of interaction (recall once more that  $r_{1,2} = \sqrt{2N}\rho \cos \beta_1$ ):

$$\phi_\nu(r_{1,2}) = \begin{cases} \frac{u(r_{1,2})}{C_m r_{1,2}}, & r_{1,2} \leq r_c \\ f_1, & r_{1,2} > r_c \end{cases} \quad (4.20)$$

$$-\frac{\hbar^2}{m} u''(r_{1,2}) + V(r_{1,2})u(r_{1,2}) = 0. \quad (4.21)$$

Function  $u(r_{1,2})$  is the two-body zero-energy scattering wave function (multiplied by  $r_{1,2}$ ), while  $f_1$  is introduced in Equation 4.13 with as-of-yet undetermined value of  $\nu$ . We solve for  $u(r)$  numerically with boundary conditions  $u(0) = 0$ ,  $u'(0) = 1$  up to  $r = r_c$  using Numerov's method [91], [92]. A two-body matching radius  $r_c$  has been introduced here, kept fixed with varying hyperradii for simplicity.  $r_c$  must be sufficiently large so that  $u(r)$  is well represented as a linear function  $C(r - a_s)$  when  $r \geq r_c$ , but also sufficiently small that it is reasonable to approximate the operator  $\frac{\Lambda^2}{2N\rho^2}$  as  $-\frac{1}{r^2} \frac{d}{dr} \left( r^2 \frac{d}{dr} \right)$ . Also, a matching coefficient  $C_m = C_m(\rho)$  is introduced to enforce continuity of  $\phi_\nu$  at  $r_{1,2} = r_c$ . See Appendix E for more details on evaluating  $f_1$  and other quantities involving hypergeometric functions, as well as hyperangular and hyperradial derivatives of  $\phi_\nu$ .

Next, we must determine the parameters  $\nu$  in  $f_1$ . We do so by imposing a continuity of the log-derivative of  $r\phi_\nu(r)$  at  $r = r_c$ . With  $\rho$  fixed, write shorthand  $x_1 = \cos \beta_1 = \frac{r_{1,2}}{\sqrt{2N}\rho}$ . Then  $\nu = \nu(\rho)$  is a discrete parameter that satisfies the following equation at  $r_{1,2} = r_c$ ,  $x_1 = x_c = \frac{r_c}{\sqrt{2N}\rho}$ :

$$\begin{aligned}
(\sqrt{2N}\rho) \frac{u'(r_{1,2})}{u(r_{1,2})} &= \frac{\frac{d}{dx_1}(x_1 f_1)}{x_1 f_1} \\
&= \left( \frac{(\nu+1)(\nu+3N-6)}{3N-6} \right) \frac{{}_2F_1\left(\frac{-\nu}{2}, \frac{\nu+3N-5}{2}, \frac{3N-4}{2}, 1-x_1^2\right)}{{}_2F_1\left(\frac{-\nu-1}{2}, \frac{\nu+3N-6}{2}, \frac{3N-6}{2}, 1-x_1^2\right)}. \quad (4.22)
\end{aligned}$$

The parameter  $\nu$  is not quite directly related to the variational adiabatic hyperspherical potential, because Eqn. 4.9 shows that contributions from the small- $r$  part of  $\phi_\nu$  and from the two-body interactions must also be computed, but  $\nu$  gives a sense for the nodal structure of the ansatz outside the coalescence regions when all particles are far from each other.

However, as maximum allowed two-body distance given hyperradius,  $r_m = \sqrt{2N}\rho$ , starts to approach chosen matching radius  $r_c$  as one takes  $\rho$  smaller and smaller, the conditions for Eqn. 4.20 start to break down. In particular, because the range of  $r_c < r < r_m$  starts to shrink, the nodal structure of  $\phi_\nu$  for excited states starts to become unphysical; symmetrizing  $\phi_\nu$  will not lead to any sensible approximation for an excited channel function. This is one regime where the theory breaks down, but it is observed that excited potential curves exhibit repulsive  $\rho^{-2}$  behavior, and hence it is not of any interest to try to compute the excited hyperspherical potentials accurately for small  $\rho$ .

For the ground state represented by the first  $\phi_\nu$  that has nodeless  $f_1$ , when  $r_m < r_c$ , we replace  $\phi_\nu$  by an alternative ansatz constructed purely out of zero-energy numerical two-body scattering wave function:

$$\phi_a(r_{1,2}) = \frac{u(r_{1,2})}{r_{1,2}} \quad (4.23)$$

In this construction,  $\nu$  and  $C_m$  are no longer relevant. The only parameter to be tuned is the strength of the two-body interaction, which determines the number of nodes of  $u(r)$  and hence the number of dimers by Levinson's Theorem [2]. It is observed that if  $u(r)$  has a node in range  $0 < r < r_m$ , this ansatz does not give sensible results of variational calculations. Symmetrizing such  $\phi_a$  is not expected to faithfully model the nodal structure of the actual channel function. On the other hand, if  $u(r)$  is nodeless, then an ansatz constructed out of  $\phi_a$  gives a potential curve that connects smoothly to the potential curve of lowest  $\phi_\nu$  for

larger  $\rho$ . Such calculation is crucial to avoid a Thomas collapse of attractive  $\rho^{-2}$  for  $N = 3$  and give estimates for bound states of  $N$  bosons.

#### 4.2.4 Analysis of Two-Body Ansatz

To understand Eqn. 4.22 better, consider the zero-range limit, with finite range of interaction  $r_0 \rightarrow 0$ , so one may also take matching radius  $r_c \rightarrow 0$ . Then the left-hand-side of Eqn. 4.22 reaches limit  $-\frac{\sqrt{2N}\rho}{a_s}$ . Meanwhile, the right-hand-side approaches  $-2\frac{\Gamma(\frac{-\nu}{2})\Gamma(\frac{\nu+3N-5}{2})}{\Gamma(\frac{-\nu-1}{2})\Gamma(\frac{\nu+3N-6}{2})}$ . For  $N = 3$ , Eqn. 4.22 then tends to the following limit:

$$\frac{\rho}{a_s} = \frac{1}{\sqrt{6}} (\nu + 2) \frac{\sin\left(\frac{\pi}{2}(\nu + 1)\right)}{\sin\left(\frac{\pi}{2}\nu\right)}. \quad (4.24)$$

Compare with the well-known results of three-body zero-range theory (see [7] for one derivation using the Lippmann-Schwinger Equation, and beware the different convention for hyperradius with different mass scaling). With two-body interaction  $V(r)$  taken to be *regularized* pseudopotential  $\left(\frac{4\pi\hbar^2 a_s}{m}\right) \delta(\vec{r}) \frac{\partial}{\partial r} r$  (regularization introduced to deal with zero-energy wave function  $\frac{u(r)}{r} = C\left(1 - \frac{a_s}{r}\right)$  that exhibits divergent behavior), the exact adiabatic eigenvalues of  $H_{ad}$  with symmetry  $J^\pi = 0^+$  are calculated to be  $\frac{\hbar^2}{2mN} \left(\frac{\nu(\nu+4)}{\rho^2}\right)$ , where  $\nu$  is a solution of the following equation:

$$\frac{\rho}{a_s} = \frac{1}{\sqrt{6}} \frac{\left[(\nu + 2) \sin\left(\frac{\pi}{2}(\nu + 1)\right) + \frac{8}{\sqrt{3}} \sin\left(\frac{\pi}{6}(\nu + 2)\right)\right]}{\sin\left(\frac{\pi}{2}\nu\right)}. \quad (4.25)$$

Fig. 4.2 shows the right-hand-sides of Eqns. 4.24 and 4.25 for real and complex values of  $\nu$ . There are vertical asymptotes at  $\nu = 0, 2, 4, \dots$ , indicating the known hyperspherical harmonic eigenvalues of Sec. 4.2.2 when particles do not interact and  $a_s = 0$ . The asymptotes separate solutions  $\nu$  into different discrete branches. As shown in Appendix D,  $\nu = 2$  is forbidden for 3 non-interacting bosons, and Eqn. 4.25 neglects this asymptote correctly, but Eqn. 4.24 incorrectly asserts this value of  $\nu$  as a non-interacting solution. Indeed, there is a term proportional to  $\sin\left(\frac{\pi}{6}(\nu + 2)\right)$  in Eqn. 4.25 that is missing in Eqn. 4.24, and that term comes precisely from the simultaneous contribution of particle 3 as particles 1 and 2 interact with each other.

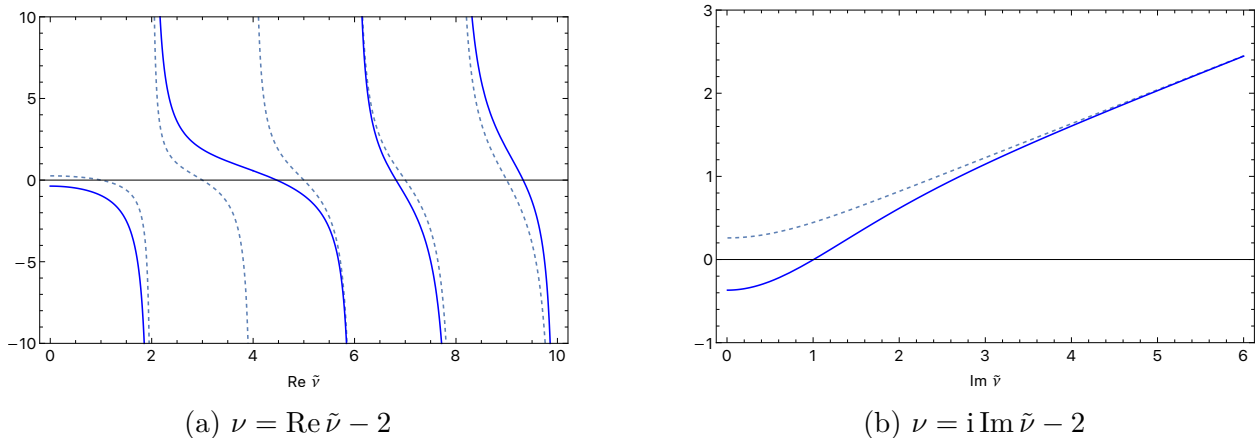


**Figure 4.2.** Right-hand-sides of Eqs. 4.25 (solid) and 4.24 (dashed), as a function of  $\tilde{\nu} = \nu + \frac{3N-5}{2} = \nu + 2$ , which is either positive real or positive imaginary.

Recall that when Eqn. 4.24 was derived by constructing ansatz  $\phi_\nu$  in Eqn. 4.20, only 2 particles were considered while the other  $N - 2$  particles were ignored. Though we shall later attempt to take all  $N$  particles into account by symmetrizing  $\phi_\nu$  in a summation as inspired by the methods of Faddeev decomposition, our theory is not the same as *exact* Faddeev decomposition [4], [76], [77], [93], which takes all  $N$  particles into account in computing a component of form  $\phi(r_{i,j})$ .

The second branch of Eqn. 4.22, corresponding to  $0 < \nu \leq 2$  in Fig. 4.2, consistently gave unreasonable results for variational hyperspherical potentials of this work. It was noted that the function  $Y_n$  in Eqn. 4.16 is 0 when  $n = 1$ , and similarly, when  $\rho \gg |a_s|$ , corresponding sum-symmetrized  $\phi_\nu$  tends to cancel itself out (this is referred to as a “spurious” solution in Faddeev decomposition). Hence the second branch shall be *ignored* in all future discussions, even though the third branch of Eqn. 4.24 may overestimate  $\nu$  compared to the second branch of Eqn. 4.25.

Also worth emphasizing again is that for the exact zero-range theory, the solutions  $\nu$  of Eqn. 4.25 directly give the adiabatic hyperspherical potentials  $\frac{\hbar^2}{2mN} \left( \frac{\nu(\nu+4)}{\rho^2} \right)$ . However, the solutions  $\nu$  obtained from the logarithmic-derivative matching condition of Eqs. 4.22 and 4.24 are not *directly* related to the variational adiabatic hyperspherical potentials  $U(\rho)$ ; they only approximately denote the nodal behavior of the ansatz function outside any coa-

lescence region where  $r_{i,j}$  vanishes. The expectation value of the grand angular momentum operator  $\Lambda^2$  must include contributions from the numerical zero-energy scattering wave function  $u(r_{i,j})$ , and the expectation value of the finite-range interactions  $V(r_{i,j})$  must also be computed in contrast to zero-range theory.

Of particular interest are the lowest solutions to Eqns. 4.24 and 4.25 when  $|a_s| \gg \rho$ . In that limit, lowest solutions  $\nu_{app}$  and  $\nu_{ex}$  to Eqns. 4.24 and 4.25, respectively, can be written as a linear expansion in  $\frac{\rho}{a_s}$ :

$$\nu_{app} \approx -1 - \frac{2\sqrt{6}}{\pi} \left( \frac{\rho}{a_s} \right) + \mathcal{O} \left( \left( \frac{\rho}{a_s} \right)^2 \right), \quad (4.26)$$

$$\nu_{ex} \approx -2 + i \left[ s_0 + 1.65317 \left( \frac{\rho}{a_s} \right) + \mathcal{O} \left( \left( \frac{\rho}{a_s} \right)^2 \right) \right], \quad s_0 \approx 1.00624. \quad (4.27)$$

In the true limit  $|a_s| \rightarrow \infty$ , exact  $\nu = -2 + is_0$  gives rise to adiabatic eigenvalue  $\frac{\hbar^2}{2mN} \left( \frac{-s_0^2 - 4}{\rho^2} \right)$  of  $H_{ad}$ , and when mock centrifugal term  $\frac{\hbar^2}{2mN} \left( \frac{15}{4\rho^2} \right)$  is added, it gives final result for the *attractive* hyperspherical potential  $\frac{\hbar^2}{2mN} \left( \frac{-s_0^2 - 1/4}{\rho^2} \right)$ ; this is the heart of “Efimov” physics of 3 bosons.

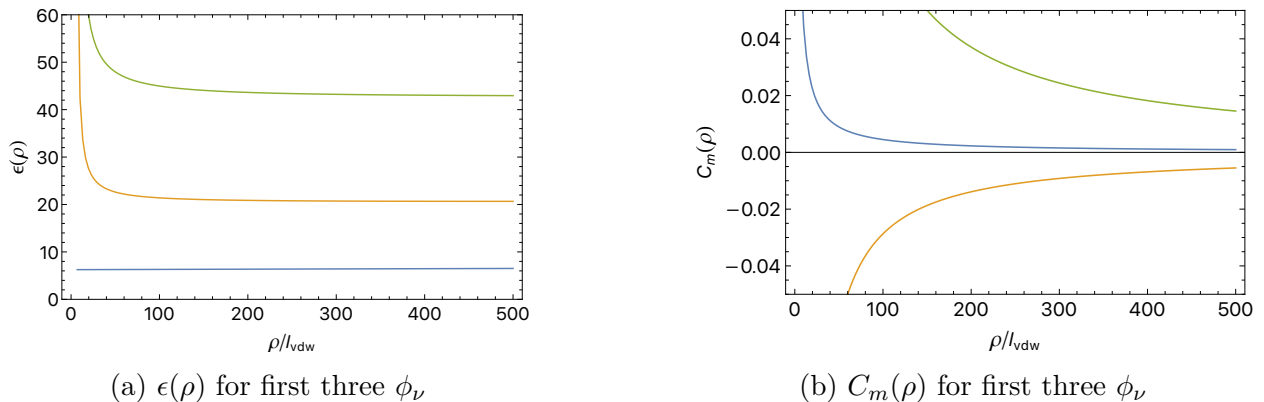


**Figure 4.3.**  $\epsilon = \tilde{\nu}^2 = \left( \nu + \frac{3N-5}{2} \right)^2$  and  $C_m$  as functions of  $\rho$ .

Fig. 4.3 shows  $\epsilon(\rho) = \tilde{\nu}^2 = \left( \nu + \frac{3N-5}{2} \right)^2$  and matching coefficient  $C_m(\rho)$  relevant for constructing  $\phi_\nu$  with  $N = 4$  bosons, soft-core Van der Waals interaction with  $\sigma = 1.6471095l_{vdw}$ , and  $a_s = -10,000l_{vdw}$ . The two-body interaction is too weak to support any dimer. Matching radius  $r_c = 15l_{vdw}$  was chosen.  $\epsilon$  and  $|C_m|$  are always observed to follow an order, with

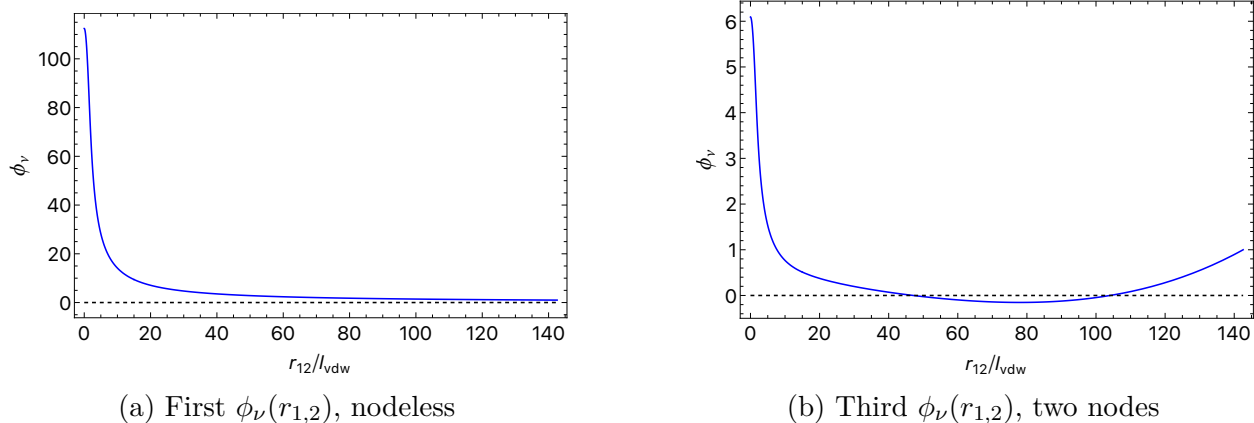


**Figure 4.4.** First and third  $\phi_\nu(r_{1,2})$  at fixed  $\rho$ .

the first ansatz having lowest values and so on. Because  $|a_s|$  is so large, values of  $\epsilon(\rho)$  remain nearly constant as functions of  $\rho$ ; when  $a_s$  is chosen to be comparable to  $\rho$ ,  $\epsilon$  changes noticeably. However, notice the steep increase of  $\epsilon$  for 2nd and 3rd ansatz at small  $\rho$ ; this is a sign of the breakdown of excited-state ansatz at small  $\rho$  that was previously discussed in Sec. 4.2.3. As  $\rho$  decreases,  $\phi_\nu$  attempts to squeeze in nodes at a shrinking range of  $r_c < r < r_m = \sqrt{2N}\rho$  in an unphysical manner.

Fig. 4.4 illustrates the first and third ansatz function  $\phi_\nu(r)$  when  $\rho = 50.41l_{vdw}$  and maximum  $r_m = \sqrt{2N}\rho = 142.6l_{vdw}$ . Parameters  $(\nu, C_m)$  for the 1st function are  $(-0.9936, 8.895 \times 10^{-3})$ ; they are  $(3.422, 0.1641)$  for the 3rd function. Note the behavior for  $r > r_c = 15l_{vdw}$ ; the first function is nodeless, while the third function has two nodes. No hyperangular normalization is applied here; the functions are initially chosen with normalization  $\phi_\nu(r_m) = 1$ . Also note the steep peak of the functions for  $r < r_c$ . In the zero-range limit, the peaks would have diverged with  $r^{-1}$  behavior, but they reach finite values due to the finite-range interactions. As  $\rho$  increases,  $\phi_\nu$  exhibits an ever taller peak at shrinking range of  $r < r_c$  (shrinking because  $r_c$  is constant but maximum  $r_m$  increases). This behavior caused great complications in performing the necessary hyperangular integration and had to be overcome.

### 4.3 Direct Hyperangular Integration

#### 4.3.1 Product and Sum Symmetrization for $N = 3$

Having constructed the two-body functions  $\phi_\nu(r_{1,2})$  and  $\phi_a(r_{1,2})$  of Eqns. 4.20 and 4.23, next we consider the necessary hyperangular integrals for implementing the formalism of Eqn. 4.8. First we consider  $N = 3$ , for which we can consider and perform computations using both *product* and *sum* symmetrization. With two-body function  $\phi$  (subscript  $\nu$  and  $a$  suppressed), we construct symmetrized ansatz functions:

$$\Phi^{(p)}(\rho; \Omega) = \prod_{i < j}^N \phi(r_{i,j}), \quad (4.28)$$

$$\Phi^{(s)}(\rho; \Omega) = \sum_{i < j}^N \phi(r_{i,j}). \quad (4.29)$$

Both Eqns. 4.28 and 4.29 are mathematically valid ways of fully symmetrizing the ansatz function to describe  $N$  bosons. The product form is inspired by the *Jastrow* wave function, and the sum form is inspired by the *Faddeev* decomposition, as discussed in Sec. 4.1.

There are 5 different types of hyperangular integrals that must be computed:

$$\begin{aligned} I_1 &= C(\rho) = \langle \Phi | \Phi \rangle, \\ I_2 &= \langle \Phi | \Lambda^2 | \Phi \rangle, \\ I_3 &= \sum_{i < j}^N \langle \Phi | V(r_{i,j}) | \Phi \rangle, \\ I_4 &= \frac{1}{2} C'(\rho) = \left\langle \Phi \left| \frac{\partial}{\partial \rho} \right| \Phi \right\rangle, \\ I_5 &= \left\langle \frac{\partial \Phi}{\partial \rho} \left| \frac{\partial \Phi}{\partial \rho} \right. \right\rangle. \end{aligned} \quad (4.30)$$

See Appendix E for details on how to compute the hyperangular and hyperradial derivatives of  $\phi(r_{i,j})$ . We proceed by using the Smith-Whitten coordinate system with 2 hyperangles  $\theta$  and  $\phi$ . (See Appendix C.1. It should be clear from context when one refers to function

$\phi_\mu$  and when one refers to coordinate  $\phi$ .) The Euler angle contribution  $\int \frac{1}{4} \sin \beta \, d\alpha \, d\beta \, d\gamma = \pi^2$  is the same for all 5 integrals and may be ignored, since final quantities of interest in Eqn. 4.8 involve  $\frac{I_2}{I_1}$  and other similar quotients.

In particular, the two-body distances are as follows:

$$\begin{aligned} r_{1,2} &= \sqrt{3}\rho\sqrt{1 + \cos(2\theta)\cos(2\phi)}, \\ r_{1,3} &= \sqrt{3}\rho\sqrt{1 + \cos(2\theta)\cos\left(2\phi - \frac{2\pi}{3}\right)}, \\ r_{2,3} &= \sqrt{3}\rho\sqrt{1 + \cos(2\theta)\cos\left(2\phi + \frac{2\pi}{3}\right)}. \end{aligned} \quad (4.31)$$

For instance, to compute  $\frac{\partial}{\partial\theta}\phi(r_{1,2})$  that appears in  $I_2$ , one needs  $\frac{\partial}{\partial\theta}r_{1,2} = -\frac{3\rho^2 \sin 2\theta \cos 2\phi}{r_{1,2}}$ . Effectively  $\Lambda^2 = -\frac{1}{\sin 4\theta} \frac{\partial}{\partial\theta} \left( \sin 4\theta \frac{\partial}{\partial\theta} \right) - \frac{1}{\cos^2 2\theta} \frac{\partial^2}{\partial\phi^2}$  in  $I_2$ . To simplify that integral, perform an integration by parts as follows:

$$\begin{aligned} I_2 &= -\int_0^{\pi/4} d\theta \int_0^{2\pi} d\phi \sin 4\theta \Phi \left( \frac{1}{\sin 4\theta} \frac{\partial}{\partial\theta} \left( \sin 4\theta \frac{\partial}{\partial\theta} \right) + \frac{1}{\cos^2 2\theta} \frac{\partial^2}{\partial\phi^2} \right) \Phi \\ &= \int_0^{\pi/4} d\theta \int_0^{2\pi} d\phi \sin 4\theta \left[ \left( \frac{\partial}{\partial\theta} \Phi \right)^2 + \frac{1}{\cos^2 2\theta} \left( \frac{\partial}{\partial\phi} \Phi \right)^2 \right]. \end{aligned} \quad (4.32)$$

Because, by virtue of the numerical two-body wave function  $u(r)$ , the ansatz function  $\phi_\nu$  or  $\phi_a$  does not diverge anywhere, the surface term  $\left[ \sin 4\theta \Phi \frac{\partial\Phi}{\partial\theta} \right]_0^{\pi/4}$  vanishes. The other surface term  $\left[ \Phi \frac{\partial\Phi}{\partial\phi} \right]_0^{2\pi}$  also vanishes because of full periodicity in angle  $\phi$ . All efforts have been made in this work to avoid second-derivatives of any kind, because the log-derivative matching condition in Eqns. 4.20 and 4.22 guarantees continuity of the first derivative of the ansatz two-body function, but *not* continuity of the second derivative.

Full ranges of angles  $\theta$  and  $\phi$  are  $[0, \frac{\pi}{4}]$  and  $[0, 2\pi]$ , but given complete particle exchange symmetry of the integrands in  $I_1$  to  $I_5$ , the range of  $\phi$  may be restricted to  $[0, \frac{\pi}{6}]$ , and hence  $\int d\Omega$  may be effectively taken to be  $\int_0^{\pi/4} d\theta \int_0^{\pi/6} d\phi \sin 4\theta$ . Symmetry factor 12 from reduction of range of  $\phi$  may be ignored because quotients of integrals are to be taken later. To prove

this assertion, one can show straightforwardly that the integrands  $I_1, \dots, I_5$  remain invariant upon the following 4 transformations:  $\phi \rightarrow \phi + \pi$ ,  $\phi \rightarrow \phi + \frac{\pi}{3}$ ,  $\phi \rightarrow \phi + \frac{2\pi}{3}$ , and  $\phi \rightarrow \frac{\pi}{3} - \phi$ .

In the restricted ranges  $\theta \in [0, \frac{\pi}{4}]$  and  $\phi \in [0, \frac{\pi}{6}]$ , there is only one coalescent point, namely where  $r_{2,3} = 0$  at  $(\theta, \phi) = (0, \frac{\pi}{6})$ . Recall that when  $\rho \gg r_0$ , the two-body ansatz function  $\phi_\nu(r)$  varies rapidly at small  $r$  comparable to  $r_0$  (see Fig. 4.4). Therefore, one must divide the domain of integration into 4 parts, with some auxiliary length scale  $\tilde{r}$ :

- Reg. I:  $0 < \theta < \frac{\tilde{r}}{\rho}$ ,  $0 < \phi < \frac{\pi}{6} - \frac{\tilde{r}}{\rho}$
- Reg. II:  $0 < \theta < \frac{\tilde{r}}{\rho}$ ,  $\frac{\pi}{6} - \frac{\tilde{r}}{\rho} < \phi < \frac{\pi}{6}$
- Reg. III:  $\frac{\tilde{r}}{\rho} < \theta < \frac{\pi}{4}$ ,  $0 < \phi < \frac{\pi}{6} - \frac{\tilde{r}}{\rho}$
- Reg. IV:  $\frac{\tilde{r}}{\rho} < \theta < \frac{\pi}{4}$ ,  $\frac{\pi}{6} - \frac{\tilde{r}}{\rho} < \phi < \frac{\pi}{6}$

$\tilde{r}$  should be about an order of magnitude greater than the range  $r_0$  of two-body interaction, indicating at which values of  $r < \tilde{r}$  the function  $\phi_\nu$  varies rapidly. It could be but need not be the same as matching radius  $r_c$  in Eqn. 4.20. Notice how the quotient  $\frac{\tilde{r}}{\rho}$  keeps shrinking as  $\rho \rightarrow \infty$ . Region II is the smallest region that covers the coalescence region of  $r_{2,3}$ . The fact that the coalescence regions may be pinpointed easily for 3 particles using the Smith-Whitten coordinates is a gift that should not be taken for granted. Such a procedure becomes far more difficult for more than 3 particles as will be apparent in the next section.

Because the integrals of this section are all two-dimensional, it is sufficient to divide each region of integration into rectangular sectors and apply nested quadrature at each sector. The usual Gauss-Legendre or more sophisticated Gauss-Kronrod quadrature may be used in each dimension, with increasing number of sectors until desired convergence is met [65].

### 4.3.2 Sum Symmetrization for $N > 3$

Next, we consider how to compute the 5 types of hyperangular integrals (see Eqns. 4.30) when there are more than 3 particles. A great deal of initial effort was invested in attempting to do computations using both product and sum symmetrized ansatz (Eqns. 4.28, 4.29) in full  $(3N - 4)$ -dimensional space using Delves hyperangles (see Appendix B). Several

candidate probability distributions were made to implement the widely-used Metropolis-Hastings algorithm (part of a wide variety of variational Monte Carlo methods [94]). Only poorly converged results could be obtained from this approach for all cases except when  $V(r) = 0$ , when ansatz  $\phi_\nu(r)$  does not vary rapidly in a small hyperangular region.

The fundamental road block was the rapidly varying behavior of the ansatz function  $\phi_\nu(r)$  when  $\rho$  is far greater than the range of two-body interaction (see Fig. 4.4). Recall that in Delves coordinates, distance between particles 1 and 2 is given by  $r_{1,2} = \sqrt{2N}\rho \cos \beta_1$ . Because the total hyperangular volume element  $d\Omega$  has factor  $\cos^2 \beta_1$ , the volume element regularizes the integrand by a factor  $r^2$  (recall  $dV = r^2 \sin \theta dr d\theta d\phi$  in usual three-dimensional problems). However, the function  $f_1$  of Eqn. 4.13 and hence the ansatz  $\phi_\nu$  roughly have a  $1/r$  divergent behavior, and the hyperangular derivative of  $\phi_\nu$  scales as  $r^{-2}$ . Though  $\phi_\nu$  does not truly diverge at any point in real space, the rapidly varying nature of the symmetrized ansatz at small localized regions of hyperangular space makes the function extremely difficult for any conventional Monte Carlo method to properly handle.

Most fortunately, the sum-symmetrized ansatz of Eqn. 4.29 has a particularly simple structure that bypasses the difficulties, so we now strictly deal with this form of ansatz for more than 3 particles. Note now that, because of exchange symmetry, the integrals  $I_1$  and  $I_2$  of Eqns. 4.30 may be decomposed into three separate terms as follows (let shorthand  $\phi_{1,2} = \phi(r_{1,2})$ ):

$$\begin{aligned}
I_1 = C(\rho) = \langle \Phi | \Phi \rangle &= \frac{1}{2} N(N-1) \int d\Omega \phi_{1,2}^2 \\
&+ N(N-1)(N-2) \int d\Omega \phi_{1,2} \phi_{1,3} \\
&+ \frac{1}{4} N(N-1)(N-2)(N-3) \int d\Omega \phi_{1,2} \phi_{3,4}, \tag{4.33}
\end{aligned}$$

$$\begin{aligned}
I_2 = \langle \Phi | \Lambda^2 | \Phi \rangle &= \frac{1}{2} N(N-1) \int d\Omega \phi_{1,2} \Lambda^2 \phi_{1,2} \\
&+ \frac{1}{2} N(N-1)(N-2) \int d\Omega \left( \phi_{1,2} \Lambda^2 \phi_{1,3} + \phi_{1,3} \Lambda^2 \phi_{1,2} \right) \\
&+ \frac{1}{8} N(N-1)(N-2)(N-3) \int d\Omega \left( \phi_{1,2} \Lambda^2 \phi_{3,4} + \phi_{3,4} \Lambda^2 \phi_{1,2} \right). \tag{4.34}
\end{aligned}$$

Integrals  $I_4$  and  $I_5$  are decomposed in a very similar manner as well. Above expressions are straightforward to show by listing all possible terms and rearranging the labels for identical particles. What this means is that for sum-symmetrization, all the terms are classified into 2-body terms involving  $r_{1,2}$  only, 3-body terms involving  $r_{1,2}$  and  $r_{1,3}$ , and 4-body terms involving  $r_{1,2}$  and  $r_{3,4}$ . Let us refer to these three terms by a second index and write  $I_1 = I_{1,1} + I_{1,2} + I_{1,3}$ , and so on.

Integral  $I_3$ , involving two-body interactions  $V(r)$ , is somewhat different and is decomposed as follows (write  $V_{1,2} = V(r_{1,2})$ ):

$$\begin{aligned}
I_3 &= \sum_{i<j}^N \langle \Phi | V(r_{i,j}) | \Phi \rangle = \frac{1}{2} N(N-1) \langle \Phi | V_{1,2} | \Phi \rangle = I_{3,1} + I_{3,2} + I_{3,3} + I_{3,4} \\
&= \frac{1}{2} N(N-1) \int d\Omega V_{1,2} \phi_{1,2}^2 \\
&\quad + N(N-1)(N-2) \int d\Omega V_{1,2} \phi_{1,3}^2 \\
&\quad + \frac{1}{4} N(N-1)(N-2)(N-3) \int d\Omega V_{1,2} \phi_{3,4}^2 \\
&\quad + \frac{1}{2} N(N-1) \int d\Omega V_{1,2} \left[ \left( \sum_{i<j}^N \phi_{i,j} \right)^2 - \sum_{i<j}^N \phi_{i,j}^2 \right]. \tag{4.35}
\end{aligned}$$

Some explanation is needed for this decomposition. First, to accurately calculate  $I_3$ , one must pay careful attention to the finite-range nature of  $V(r)$ , which is negligible for most of configuration space when  $\rho \gg r_0$ . Because  $r_{1,2} = \sqrt{2N}\rho \cos \beta_1$  only depends on one Delves hyperangle, we first express  $V$  solely in terms of  $V_{1,2}$ .

Next, because of the presence of  $V_{1,2}$ , it is not possible to decompose solely in terms of particles 1 to 4 as was done in Eqns. 4.33 and 4.34. At most 6 different particles can appear, and it is too complicated to explicitly write out all the terms. Instead, we again note that the function  $\phi_\nu(r)$  roughly scales as  $1/r$  when near a coalescence region. When we isolate out all the diagonal terms of form  $\phi_{i,j}^2$  from  $\Phi^2$ , the remainder will give a smooth integrand under the regularizing influence of volume element  $d\Omega$  (effectively of form  $r_{i,j}^2$  for every particle pair  $(i, j)$ ). This remainder gives term  $I_{3,4}$ , and the only fast-varying behavior comes from  $V_{1,2}$ .

Finally, the term  $V_{1,2} \sum_{i<j}^N \phi_{i,j}^2$  can be classified into one of three terms by shuffling the identical particle indices, giving terms  $I_{3,1}$ ,  $I_{3,2}$ , and  $I_{3,3}$ . In many ways, they can be handled in a similar fashion as integrals  $I_{1,1}$ ,  $I_{1,2}$ , and  $I_{1,3}$ .

Before we give more details about the integrals themselves, we discuss the numerical methods of integration. When the dimension of an integral is 1 or 2, it suffices to again divide into rectangular sectors and apply (nested) Gauss-Legendre or Gauss-Kronrod quadrature, as it was done in Sec. 4.3.1. However, when the dimension is 3 or higher, it is more practical to switch to a multi-dimensional method. As will be shown later, the full range of integration is divided into certain regions in order to anticipate and individually handle rapidly varying parts of integral. In each region where the integrand is expected to be smooth, usual Monte Carlo integration has been attempted first, which approximates an integral in rectangular space of vector  $\vec{X}$  with volume  $V$  by  $\int d\vec{X} f(\vec{X}) \approx \frac{V}{N} \sum_{i=1}^N f(\vec{X}_i)$ , where  $N$  is the number of randomly chosen points [94].

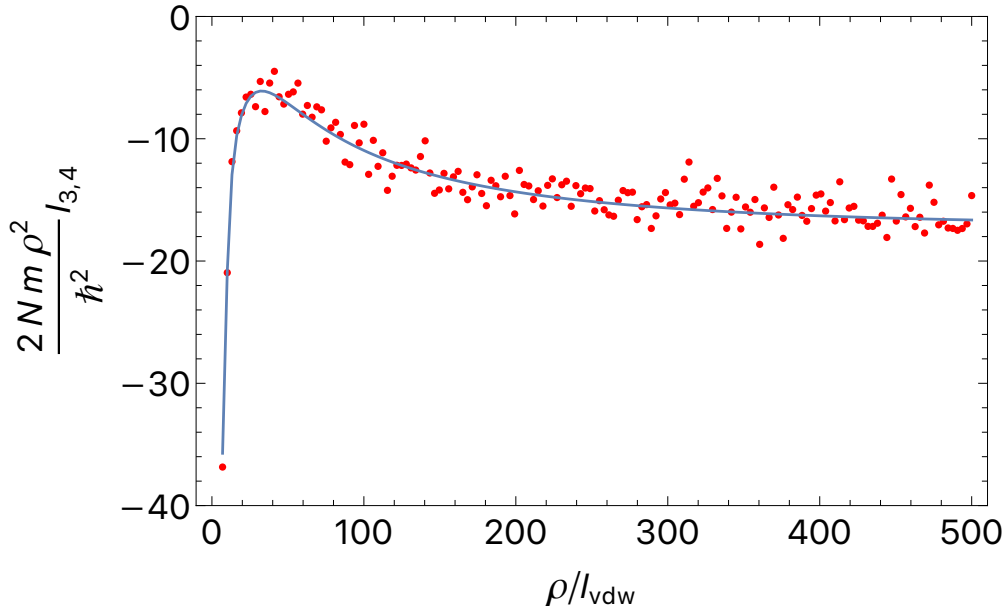


**Figure 4.5.**  $\frac{2Nm\rho^2}{\hbar^2} I_{3,4}$  for third sum-symmetrized ansatz  $\phi_\nu$ . Blue curve computed using Sobol sequences, and red dots computed from Monte Carlo method.

Fig. 4.5 shows as red dots the values of integral  $I_{3,4}$  obtained from Monte Carlo method for the sum-symmetrized third ansatz  $\phi_\nu$ , for the same conditions as in Fig. 4.3 with  $N = 4$ ,

soft-core Van der Waals interaction with  $\sigma = 1.6471095l_{vdw}$ ,  $a_s = -10,000l_{vdw}$ , and matching radius  $r_c = 15l_{vdw}$ . To deal with the short-range nature of  $V_{1,2}$ , the range of hyperangle  $\beta_1$  is split into two using parameter  $\tilde{r} = 10l_{vdw}$ , explained later; at each fixed  $\rho$ , 100,000 randomly chosen hyperangular points in 8-dimensional space are used separately for both ranges of  $\beta_1$ . Observe the not-so-optimal convergence of the results. Because terms from two different regions of space are added, and because there is a nodal structure to the ansatz function, unavoidable catastrophic cancellation occurs. The Monte Carlo method here suffers from similar pathologies as the infamous sign problem that plagues other applications of Quantum Monte Carlo methods [88], [95]. Because Monte Carlo methods fundamentally converge with error of the order of  $1/\sqrt{N}$ , with  $N$  the number of random points, computational resources required to converge the integrals to acceptable precision would be far too expensive.

Luckily, a class of alternative methods exists for multidimensional integrals in rectangular space, known as *quasi-random* methods [96]. In particular, we use Sobol sequences [97], which are designed to construct a sampling of rectangular region of  $d$ -dimensional space that is more “uniform” than a pseudorandom sampling (see Fig. 4.6 for a 2D example). Open-source codes from “[https://people.math.sc.edu/Burkardt/f\\_src/toms659/toms659.html](https://people.math.sc.edu/Burkardt/f_src/toms659/toms659.html)” are gratefully acknowledged and used to generate the Sobol sequences.

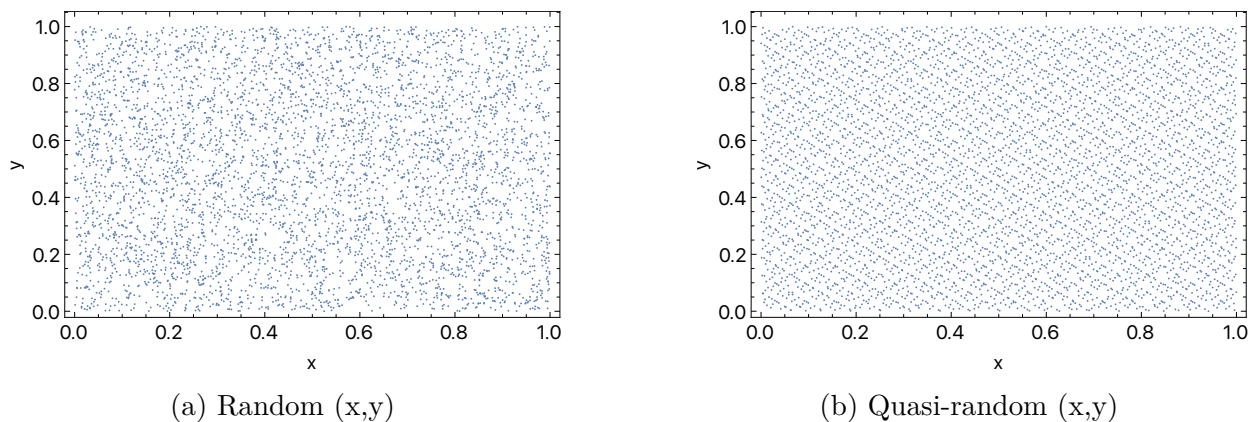


**Figure 4.6.** 5000 points (x,y) chosen randomly or from Sobol sequence.

The blue curve in Fig. 4.5 is the result of using Sobol sequences to compute the integral  $I_{3,4}$  for the same conditions as red dots previously explained. Because integration using Sobol sequences converges with error of the order of  $\frac{(\log N)^d}{N}$ , with  $d$  the number of dimensions of

space and  $N$  the number of sample points, quasi-random integration has consistently given more stable results with less noise than Monte Carlo integration. Hence, Sobol sequence is the method of choice in this dissertation for integration when dimension is 3 or higher.

## Two-Body Terms

Recall the first component of each integral that only depends on  $r_{1,2}$  (integrals  $I_4$  and  $I_5$  are very similar to  $I_1$ ):

$$I_{1,1} = \frac{1}{2}N(N-1) \int d\Omega \phi_{1,2}^2, \quad (4.36)$$

$$I_{2,1} = \frac{1}{2}N(N-1) \int d\Omega \phi_{1,2} \Lambda^2 \phi_{1,2}, \quad (4.37)$$

$$I_{3,1} = \frac{1}{2}N(N-1) \int d\Omega V_{1,2} \phi_{1,2}^2. \quad (4.38)$$

In Delves coordinates (see Appendix B),  $r_{1,2} = \sqrt{2N}\rho \cos \beta_1$  only depends on one hyperangle. The other  $3N - 5$  hyperangles are analytically integrated out, so hyperangular integration of any function  $g(r_{1,2})$  becomes:

$$\int d\Omega g(r_{1,2}) = 16 \left( \pi^{(3N-5)/2} \right) \frac{\Gamma\left(\frac{3}{2}\right)}{\Gamma\left(\frac{3}{2}(N-2)\right)} \int_0^{\pi/2} d\beta_1 \cos^2 \beta_1 \sin^{3N-7} \beta_1 g(r_{1,2}). \quad (4.39)$$

Effectively  $\Lambda^2 = -\left(\frac{1}{\cos^2 \beta_1 \sin^{3N-7} \beta_1}\right) \frac{\partial}{\partial \beta_1} \left(\cos^2 \beta_1 \sin^{3N-7} \beta_1 \frac{\partial}{\partial \beta_1}\right)$  here, so apply integration by parts to the integral involving  $\Lambda^2$  to obtain:

$$\int d\Omega \phi_{1,2} \Lambda^2 \phi_{1,2} = 16 \left( \pi^{(3N-5)/2} \right) \frac{\Gamma\left(\frac{3}{2}\right)}{\Gamma\left(\frac{3}{2}(N-2)\right)} \int_0^{\pi/2} d\beta_1 \cos^2 \beta_1 \sin^{3N-7} \beta_1 \left(\frac{\partial \phi_{1,2}}{\partial \beta_1}\right)^2. \quad (4.40)$$

For large  $\rho$ , each integral must be split into two parts. Choose a parameter  $\tilde{r}$ , roughly an order of magnitude greater than the range  $r_0$  of two-body interaction, to designate values of  $r < \tilde{r}$  where ansatz  $\phi_\nu$  varies rapidly. Then let  $\beta_c = \cos^{-1}\left(\frac{\tilde{r}}{\sqrt{2N}\rho}\right)$ , and split the range

of  $\beta_1$  into two parts:  $[0, \beta_c]$  and  $[\beta_c, \frac{\pi}{2}]$ . As  $\rho \rightarrow \infty$ ,  $\beta_c \rightarrow \frac{\pi}{2}$ , indicating an ever-shrinking coalescence region.

### Three-Body Terms

Next, recall the components of integrals that depend on distances  $r_{1,2}$  and  $r_{1,3}$ :

$$I_{1,2} = N(N-1)(N-2) \int d\Omega \phi_{1,2} \phi_{1,3}, \quad (4.41)$$

$$I_{2,2} = \frac{1}{2} N(N-1)(N-2) \int d\Omega \left( \phi_{1,2} \Lambda^2 \phi_{1,3} + \phi_{1,3} \Lambda^2 \phi_{1,2} \right), \quad (4.42)$$

$$I_{3,2} = N(N-1)(N-2) \int d\Omega V_{1,2} \phi_{1,3}^2 \quad (4.43)$$

This time, the appropriate coordinates are given in Appendix C.2 when  $N > 3$ . Integration of  $3N - 7$  hyperangles other than  $(\delta, \theta, \phi)$  gives  $\tilde{c} = 4 \left( \pi^{(3N-6)/2} \right) \frac{\Gamma(\frac{3}{2})}{\Gamma(\frac{3}{2}(N-3))}$ . First of all,  $I_{1,2}$  is calculated as follows:

$$\int d\Omega \phi_{1,2} \phi_{1,3} = 4\tilde{c} \int_0^{\pi/2} d\delta \int_0^{\pi/4} d\theta \int_{\pi/6}^{2\pi/3} d\phi \left( \sin^5 \delta \cos^{3N-10} \delta \sin 4\theta \right) \phi_{1,2} \phi_{1,3}. \quad (4.44)$$

By exchange symmetry, the range of  $\phi$  is truncated from  $[0, 2\pi]$  to  $[\frac{\pi}{6}, \frac{2\pi}{3}]$ , with symmetry factor 4 out in front. Unlike in Sec. 4.3.1, the range of  $\phi$  cannot be restricted to  $[0, \frac{\pi}{6}]$ , because  $\phi_{2,3}$  is missing in the integrand. The relevant coalescence point is when either  $\delta = 0$  (both  $r_{1,2}$  and  $r_{1,3}$  are 0), or when  $(\theta, \phi) = (0, \frac{\pi}{2})$  so that  $r_{1,2} = 0$ . It is straightforward, albeit tedious, to divide the region of integration into pieces to isolate regions around the coalescence points, similar to what was shown in Sec. 4.3.1.

Next,  $I_{2,2}$  is computed by again applying integration by parts:

$$\int d\Omega \left( \phi_{1,2} \Lambda^2 \phi_{1,3} + \phi_{1,3} \Lambda^2 \phi_{1,2} \right) = 8\tilde{c} \int_0^{\pi/2} d\delta \int_0^{\pi/4} d\theta \int_{\pi/6}^{2\pi/3} d\phi \left( \sin^5 \delta \cos^{3N-10} \delta \sin 4\theta \right) \\ \times \left[ \left( \frac{\partial \phi_{1,2}}{\partial \delta} \frac{\partial \phi_{1,3}}{\partial \delta} \right) + \frac{1}{\sin^2 \delta} \left( \frac{\partial \phi_{1,2}}{\partial \theta} \frac{\partial \phi_{1,3}}{\partial \theta} \right) + \frac{1}{\sin^2 \delta \cos^2 2\theta} \left( \frac{\partial \phi_{1,2}}{\partial \phi} \frac{\partial \phi_{1,3}}{\partial \phi} \right) \right]. \quad (4.45)$$

The same argument for particle symmetry can be applied as for  $I_{1,2}$ , with same range of  $\phi$  (again do not confuse with functions  $\phi_{1,2}$  and  $\phi_{1,3}$ ) and same coalescence points.

Finally,  $I_{3,2}$  is slightly different:

$$\int d\Omega V_{1,2} \phi_{1,3}^2 = 2\tilde{c} \int_0^{\pi/2} d\delta \int_0^{\pi/4} d\theta \int_0^{\pi} d\phi \left( \sin^5 \delta \cos^{3N-10} \delta \sin 4\theta \right) V_{1,2} \phi_{1,3}^2. \quad (4.46)$$

$I_{3,2}$  is different from all other integrals in that the range of angle  $\phi$  can only be cut in half to  $[0, \pi]$ . Relevant coalescence point is when either  $\delta = 0$  (both  $r_{1,2}$  and  $r_{1,3}$  are 0), or  $(\theta, \phi) = (0, \frac{\pi}{2})$  so  $r_{1,2} = 0$ , or  $(\theta, \phi) = (0, \frac{5\pi}{6})$  so  $r_{1,3} = 0$ . Actually,  $(\theta, \phi) = (0, \frac{5\pi}{6})$  is not really relevant because  $V_{1,2}$  would quickly become negligible at that point for large  $\rho$ .

## Four-Body Terms

Now consider the components of integrals that depend on  $r_{1,2}$  and  $r_{3,4}$ :

$$I_{1,3} = \frac{1}{4} N(N-1)(N-2)(N-3) \int d\Omega \phi_{1,2} \phi_{3,4}, \quad (4.47)$$

$$I_{2,3} = \frac{1}{8} N(N-1)(N-2)(N-3) \int d\Omega \left( \phi_{1,2} \Lambda^2 \phi_{3,4} + \phi_{3,4} \Lambda^2 \phi_{1,2} \right), \quad (4.48)$$

$$I_{3,3} = \frac{1}{4} N(N-1)(N-2)(N-3) \int d\Omega V_{1,2} \phi_{3,4}^2. \quad (4.49)$$

This is the only part of the dissertation where we make use of the H-type Jacobi tree that was introduced in Appendix A. Then relevant Jacobi vectors are  $\vec{\eta}_1 = \sqrt{\frac{1}{2}}(\vec{r}_2 - \vec{r}_1)$  and  $\vec{\eta}_2 = \sqrt{\frac{1}{2}}(\vec{r}_4 - \vec{r}_3)$ , described in terms of two Delves hyperangles  $\beta_1$  and  $\beta_2$  (see Appendix B).

Integration of other  $3N - 6$  hyperangles gives  $\tilde{c} = 64 \left( \pi^{(3N-6)/2} \right) \frac{\Gamma(\frac{3}{2})}{\Gamma(\frac{3}{2}(N-3))}$ . Any function of  $\beta_1, \beta_2$  is integrated as follows:

$$\int d\Omega g(\beta_1, \beta_2) = \tilde{c} \int_0^{\pi/2} d\beta_1 \int_0^{\pi/2} d\beta_2 \left( \cos^2 \beta_1 \sin^{3N-7} \beta_1 \right) \left( \cos^2 \beta_2 \sin^{3N-10} \beta_2 \right) g(\beta_1, \beta_2). \quad (4.50)$$

For  $I_{2,3}$ , again apply integration by parts to obtain:

$$\begin{aligned} \int d\Omega \left( \phi_{1,2} \Lambda^2 \phi_{3,4} + \phi_{3,4} \Lambda^2 \phi_{1,2} \right) &= 2\tilde{c} \int_0^{\pi/2} d\beta_1 \int_0^{\pi/2} d\beta_2 \left( \cos^2 \beta_1 \sin^{3N-7} \beta_1 \right) \\ &\times \left( \cos^2 \beta_2 \sin^{3N-10} \beta_2 \right) \left( \frac{\partial \phi_{1,2}}{\partial \beta_1} \frac{\partial \phi_{3,4}}{\partial \beta_1} \right). \end{aligned} \quad (4.51)$$

Note that only derivatives with respect to  $\beta_1$  appear, because  $\phi_{1,2}$  does not depend on  $\beta_2$ . Because  $\eta_1 = \sqrt{N}\rho \cos \beta_1$  and  $\eta_2 = \sqrt{N}\rho \sin \beta_1 \cos \beta_2$ ,  $r_{1,2}$  vanishes when  $\beta_1 = \frac{\pi}{2}$ , and  $r_{3,4}$  vanishes when  $\beta_1 = 0$  or  $\beta_2 = \frac{\pi}{2}$ .

## Many-Body Terms

Finally, recall one remaining term,  $I_{3,4}$ , for the integral involving  $V$ :

$$I_{3,4} = \frac{1}{2} N(N-1) \int d\Omega V_{1,2} \left[ \left( \sum_{i<j}^N \phi_{i,j} \right)^2 - \sum_{i<j}^N \phi_{i,j}^2 \right]. \quad (4.52)$$

Use the usual K-type Jacobi vectors of Appendix A and Delves hyperangles of Appendix B to describe this multi-dimensional system. As was discussed previously, we do not expect rapidly varying behavior from  $d\Omega \left[ \left( \sum_{i<j}^N \phi_{i,j} \right)^2 - \sum_{i<j}^N \phi_{i,j}^2 \right]$ . We need only account for the finite-range of  $V_{1,2}$  when  $\rho$  is sufficiently large. Since again  $r_{1,2} = \sqrt{2N}\rho \cos \beta_1$ , the protocol is the same as for the integrals involving only  $r_{1,2}$ . Choose a fixed parameter  $\tilde{r}$ : ansatz  $\phi_\nu$  varies rapidly when  $r < \tilde{r}$ . Let  $\beta_c = \cos^{-1} \left( \frac{\tilde{r}}{\sqrt{2N}\rho} \right)$ . Split the total volume into two parts, where the range of  $\beta_1$  is split into  $[0, \beta_c]$  and  $[\beta_c, \frac{\pi}{2}]$ , while the range of all other hyperangles remains intact.



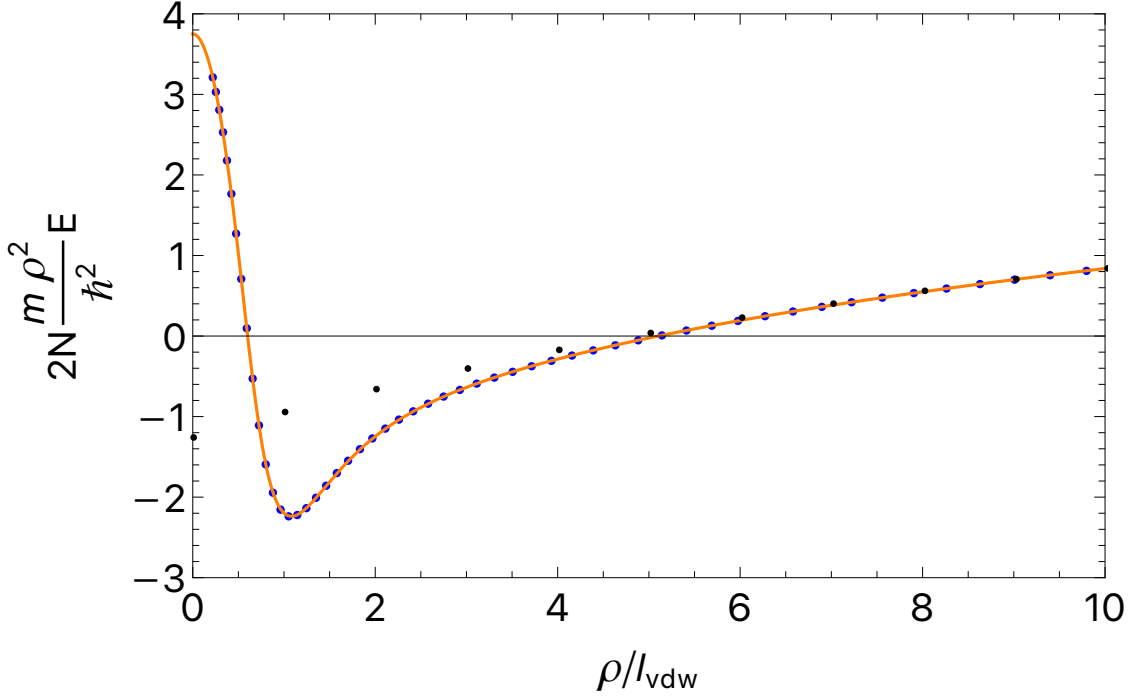


**Figure 5.2.** Coefficient of  $\frac{\hbar^2}{2mN\rho^2}$  of the lowest adiabatic potential for 3 bosons, with soft-core Van der Waals interaction,  $\sigma = 1.7180713l_{vdw}$ ,  $a_s = -10l_{vdw}$ . Black dots are from zero-range theory; blue dots are from B-spline diagonalization of  $H_{ad}$ , courtesy of Yu-Hsin Chen. Orange curve is from product symmetrization of  $\phi_a$ .

Fig. 5.1 shows the results for the lowest 4 adiabatic hyperspherical potentials of 3 bosons interacting with soft-core Van der Waals potential, with parameter  $\sigma = 1.7180713l_{vdw}$  that admits no dimer and gives  $a_s = -10l_{vdw}$ . The potentials include “mock-centrifugal” term and diagonal non-adiabatic correction  $Q$ , but with no spherical trap. Zero-range theory (black lines) and numerical diagonalization of the adiabatic Hamiltonian (blue lines), courtesy of Yu-Hsin Chen, agree well except at small values of  $\rho$ . For  $\rho \gg |a_s|$ , these coefficients converge to values  $\lambda(\lambda + 4) + \frac{15}{4}$ ,  $\lambda = 0, 4, 6, \dots$ . The red dots are from our new two-body ansatz  $\phi_\nu$ , with lowest value of  $\nu$  from Eqn. 4.22 and product symmetrization applied. They agree excellently with both zero-range and numerical diagonalization results for the lowest curve at large values of  $\rho$ . The brown dots are obtained from our ansatz  $\phi_\nu$  for 3rd and higher values of  $\nu$ , sum-symmetrized. As previously discussed, we neglect the second value of  $\nu$  that leads to a spurious solution. We consistently observe that product symmetrization of

$\phi_\nu$  with 3rd and higher values of  $\nu$  leads to poor results that do not agree with any previous theories. On the other hand, the sum-symmetrized ansatz curves agree well with excited curves from zero-range theory and numerical diagonalization, except at small values of  $\rho$  where the ansatz is known to fail.

For the same conditions as in Fig. 5.1, Fig. 5.2 shows the result for the lowest potential curve at smaller values of  $\rho$ . Excellent agreement between numerical diagonalization and our product-symmetrized ansatz function  $\phi_a$  are observed. At very small values of  $\rho$ , they reduce to the mock-centrifugal value  $\frac{15}{4}$ ; as  $\rho$  increases, they admit a potential well and then become repulsive for  $\rho \gg |a_s|$ . We observe that, even though  $\phi_\nu$  and  $\phi_a$  are two different ansatz functions, they give potential curves that connect smoothly at  $\rho = 7l_{vdw}$ . At these small values of  $\rho$ , discrepancies with zero-range theory are observed; zero-range theory predicts convergence at  $\rho = 0$  to value  $-s_0^2 - 1/4$ ,  $s_0 \approx 1.00624$ .

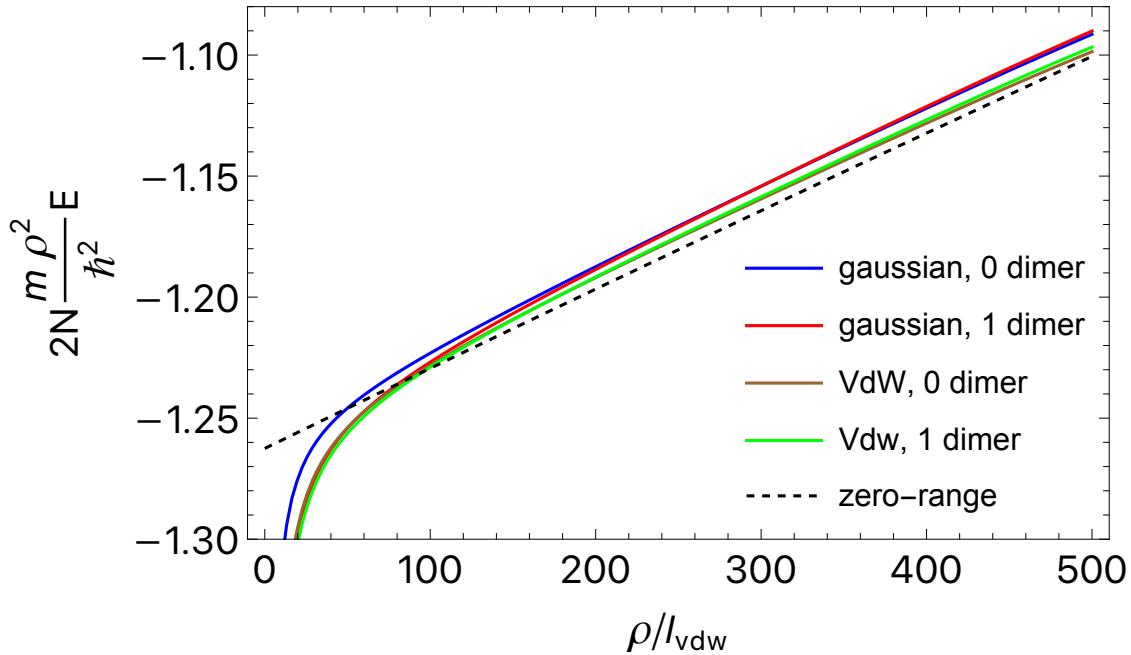


**Figure 5.3.** Comparison between zero-range theory and product-symmetrized ansatz from different finite-range interactions for the coefficient of  $\frac{\hbar^2}{2mN\rho^2}$  of the lowest hyperspherical potential,  $N = 3$ ,  $a_s = -10,000l_{vdw}$ .

We are particularly interested in what our new ansatz method predicts for the lowest hyperspherical potential curve, so Figs. 5.3 and 5.4 compare the results of zero-range theory

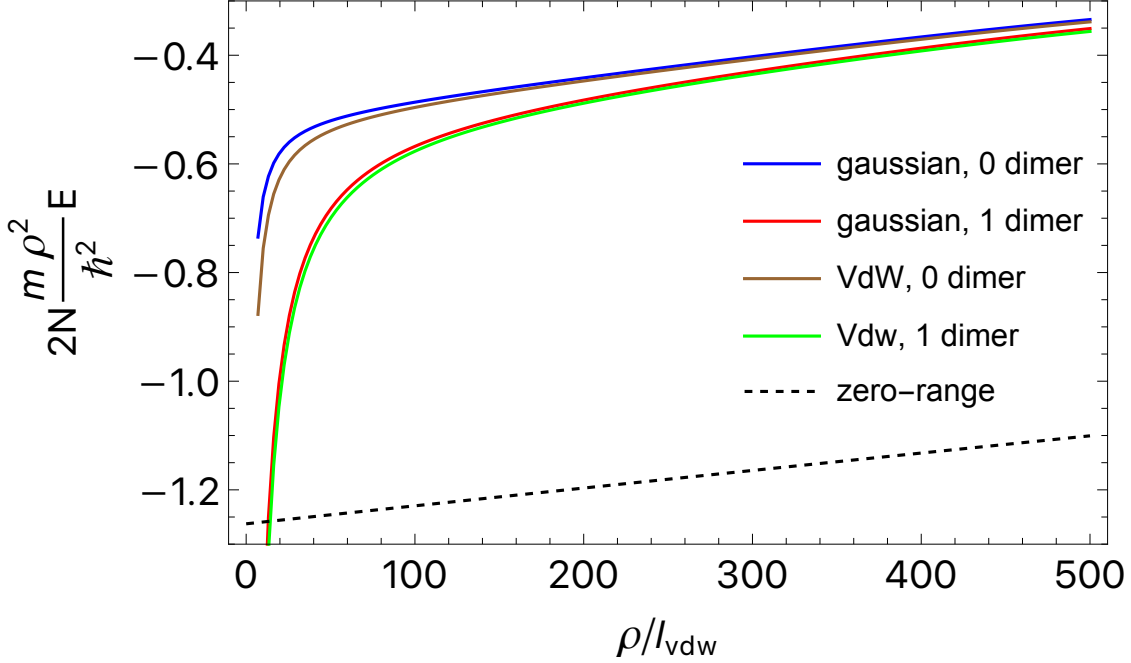


**Figure 5.4.** Comparison between zero-range theory and sum-symmetrized ansatz from different finite-range interactions for the coefficient of  $\frac{\hbar^2}{2mN\rho^2}$  of the lowest hyperspherical potential,  $N = 3$ ,  $a_s = -10,000l_{vdw}$ .

with values computed from  $\phi_\nu$  with 4 different finite-range interactions, product-symmetrized and sum-symmetrized, respectively. The finite-range interactions are either gaussians or soft-core Van der Waals potentials (same finite range  $r_0 = l_{vdw}$ ), with differently tuned strengths so that they may support either 0 or 1 deep dimer, all giving rise to the same scattering length near unitarity. Note that the zero-range result converges to value  $-s_0^2 - 1/4$ ,  $s_0 \approx 1.00624$  at  $\rho = 0$ , with a linear correction for nonzero values of  $\rho$  (see Eqn. 4.27) because the system is not at absolutely unitary limit  $|a_s| \rightarrow \infty$ .

In Fig. 5.3, excellent agreement between zero-range theory and product-symmetrized ansatz results for all 4 finite-range interactions is observed in the regime  $\rho \gg |a_s|$ , with deviations for smaller values of  $\rho$  as expected for finite-range calculations. The assumptions of zero-range theory, that the details of the finite-range interaction are irrelevant for  $\rho \gg r_0$ , are validated. On the other hand, in Fig. 5.4, results from the sum-symmetrized ansatz differ quite noticeably from zero-range predictions. It is encouraging that at least the sum-symmetrized ansatz still predicts the adiabatic hyperspherical potential to be attractive,

giving qualitatively the correct behavior. If we fit the numerical curves of Fig. 5.4 to form  $A + B\rho + \frac{C}{\rho}$ , with a linear term inspired by Eqn. 4.27 and a  $\frac{1}{\rho}$  term visually apparent, all 4 results give roughly the same value of  $A$  from -0.499 to -0.505 (well above  $-s_0^2 - 1/4$ ), and similar values of  $B$ , but very different values of  $C$ . One must not extrapolate this fit to larger  $\rho$  and claim that the adiabatic potential asymptotically behaves as  $1/\rho$ , because the linear expansion in Eqn. 4.27 is in terms of  $\frac{\rho}{a_s}$ ; asymptotically, when  $\rho \gg |a_s|$ , the hyperspherical potential will converge to “mock” centrifugal term  $\frac{\hbar^2}{2mN} \left( \frac{(3N-4)(3N-6)}{4\rho^2} \right) = \frac{\hbar^2}{2mN} \left( \frac{15}{4\rho^2} \right)$ . It is interesting to note that in Fig. 5.4, gaussian and Van der Waals potentials will give roughly the same results when they admit the same number of deep dimers.

## 5.2 Potential Curves for $N > 3$

Next, we discuss the results of sum-symmetrized ansatz for more than 3 particles. We use gaussian or soft-core Van der Waals two-body interactions that do not support any deep dimer in order to simplify the calculations.

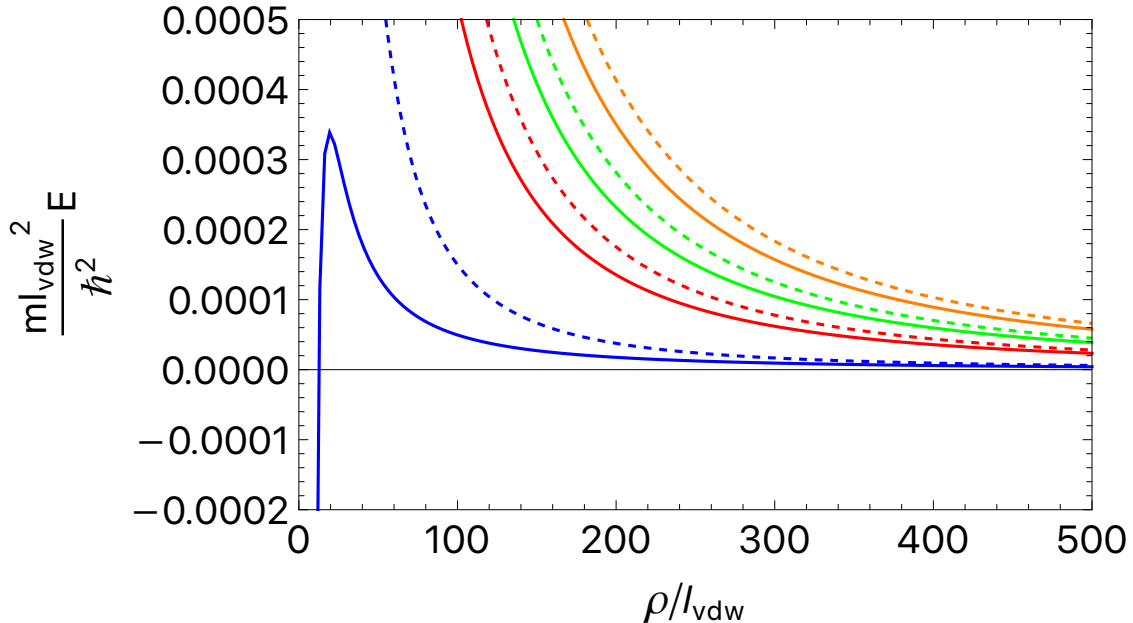


**Figure 5.5.** Variational adiabatic hyperspherical potentials for  $N = 4$ , Van der Waals potential,  $a_s = -300l_{vdw}$ . Dashed curves are non-interacting potentials with  $\lambda = 0, 4, 6$ , and  $8$ .

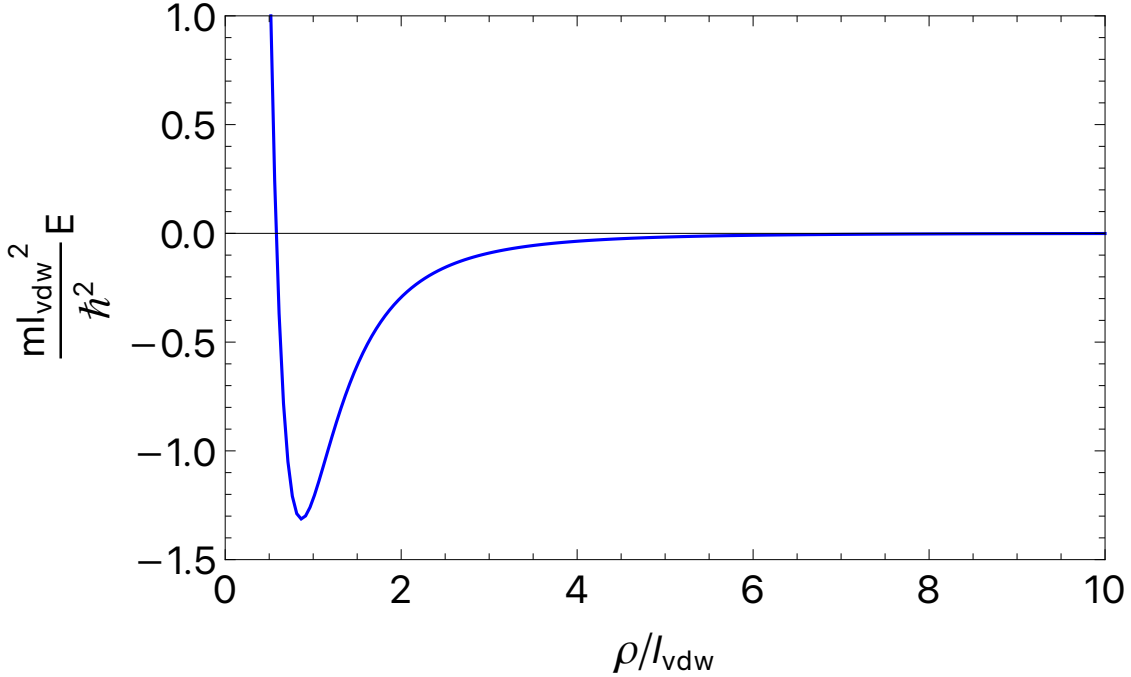


**Figure 5.6.** Lowest variational adiabatic hyperspherical potential for  $N = 4$ , Van der Waals potential,  $a_s = -300l_{vdw}$ .

Fig. 5.5 shows the results for sum-symmetrized  $\phi_\nu$  for 4 particles with soft-core Van der Waals interaction,  $a_s = -300l_{vdw}$ . The solid curves are the numerical results from the ansatz, using the 1st, 3rd, 4th, and 5th values of  $\nu$  that are solutions of the log-derivative matching condition Eqn. 4.22 (once again, the 2nd value of  $\nu$  is omitted). The dashed curves are the non-interacting potentials  $\frac{\hbar^2}{2mN\rho^2} \left( \lambda(\lambda + 3N - 5) + \frac{(3N-4)(3N-6)}{4} \right) = \frac{\hbar^2}{2mN\rho^2} (\lambda(\lambda + 7) + 12)$  with  $\lambda = 0, 4, 6, 8$ . It is clear that the mutual particle interaction made the hyperspherical potentials less repulsive relative to the non-interacting limit, but what is even more striking, perhaps, is the existence of a potential barrier and a very deep local minimum for the lowest potential curve for small values of  $\rho$ , as seen in Fig. 5.6. Fig. 5.6 used ansatz  $\phi_a$  (Eqn. 4.23) made purely of numerical two-body wave function  $u(r)$  with no reference to parameter  $\nu$ , but we verified that the potential of Fig. 5.6 connects smoothly to the lowest potential of Fig. 5.5.

We appear to obtain consistently similar shapes of the variational adiabatic hyperspherical potentials for  $N > 3$ . It is interesting to note that the shape of the lowest potential looks

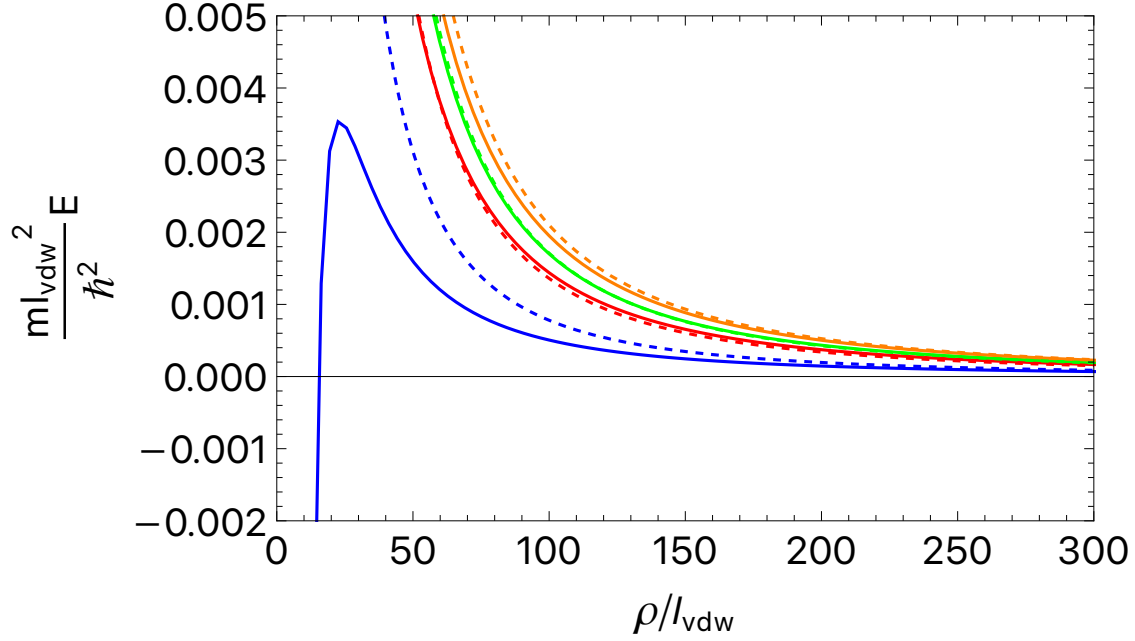


**Figure 5.7.** Variational adiabatic hyperspherical potentials for  $N = 10$ , Van der Waals potential,  $a_s = -300l_{vdw}$ . Dashed curves are non-interacting potentials with  $\lambda = 0, 4, 6$ , and  $8$ .

quite similar to what was predicted in Ref. [98] for 5 bosons, not from directly diagonalizing the adiabatic Hamiltonian but by fitting parameters to reproduce bound-state energies. Fig. 5.7 shows the results for  $N = 10$ , with the same soft-core Van der Waals potential that admits  $a_s = -300l_{vdw}$ , using sum-symmetrized ansatz  $\phi_\nu$  with 1st, 3rd, 4th, and 5th values of  $\nu$  that are solutions of the log-derivative matching Eqn. 4.22. The dashed curves are the non-interacting potentials  $\frac{\hbar^2}{2mN\rho^2} \left( \lambda(\lambda + 3N - 5) + \frac{(3N-4)(3N-6)}{4} \right) = \frac{\hbar^2}{2mN\rho^2} (\lambda(\lambda + 25) + 156)$  with  $\lambda = 0, 4, 6, 8$ . Notice how much stronger the “mock” centrifugal potential is now, compared to the case for  $N = 4$ .

Once again, the lowest potential curve is less repulsive compared to the non-interacting limit, with the appearance of a barrier and a deep local minimum near small values of  $\rho$ . However, unlike in Fig. 5.5 where the numerical excited curves all consistently are less repulsive than the non-interacting excited curves, in Fig. 5.7, ansatz results for the excited curves exhibit less obvious behavior. It is quite likely that for  $N = 10$ , there are many degenerate excited hyperspherical harmonics (eigenfunctions of  $\Lambda^2$ ) that would couple and

mix in the presence of interaction, while each of our ansatz function corresponds to only one particular hyperspherical harmonic in the non-interacting limit. Hence, the ansatz results for the excited potential curves are unlikely to be correct for large values of  $N$ . However, since there is no degeneracy for the lowest hyperspherical harmonics (a constant), we may still hope that the lowest variational hyperspherical potential gives sensible descriptions of  $N$  bosons relevant for condensate physics.

### 5.3 Comparison of Potentials for $N = 4$

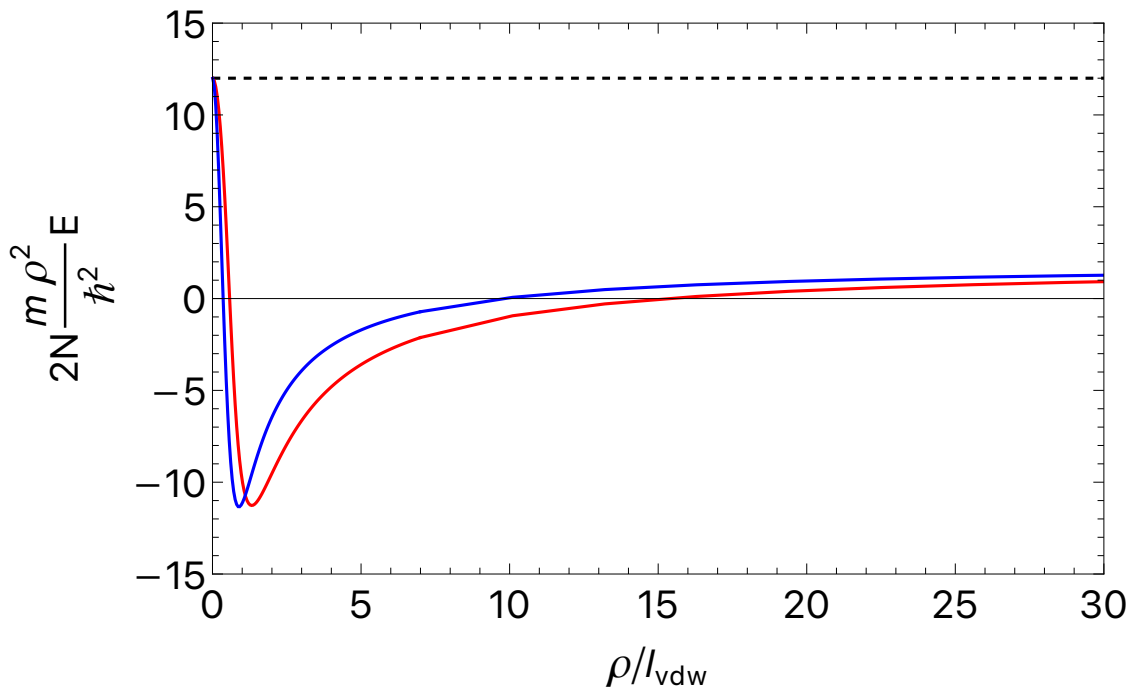


**Figure 5.8.** Coefficient of  $\frac{\hbar^2}{2mN\rho^2}$  of the lowest variational potential for  $N = 4$ , for gaussian (blue) or soft-core Van der Waals (red) interaction with same  $r_0 = l_{vdw}$ , with  $a_s = -10,000l_{vdw}$ . Black dashed line is the non-interacting limit of 12.

To better understand the physics implied by the lowest variational hyperspherical potential from our sum-symmetrized ansatz, we first examine the effect of different finite-range interactions on the potential. Fig. 5.8 shows the coefficients of  $\rho^{-2}$  for the lowest potential curve of 4 bosons, where blue curve is computed with a gaussian potential and red curve is computed with soft-core Van der Waals potential. The two interactions have the same

length scale,  $r_0 = l_{vdw}$ , and admit  $a_s = -10,000l_{vdw}$ , close to unitarity. The black dashed line is the non-interacting limit of 12.

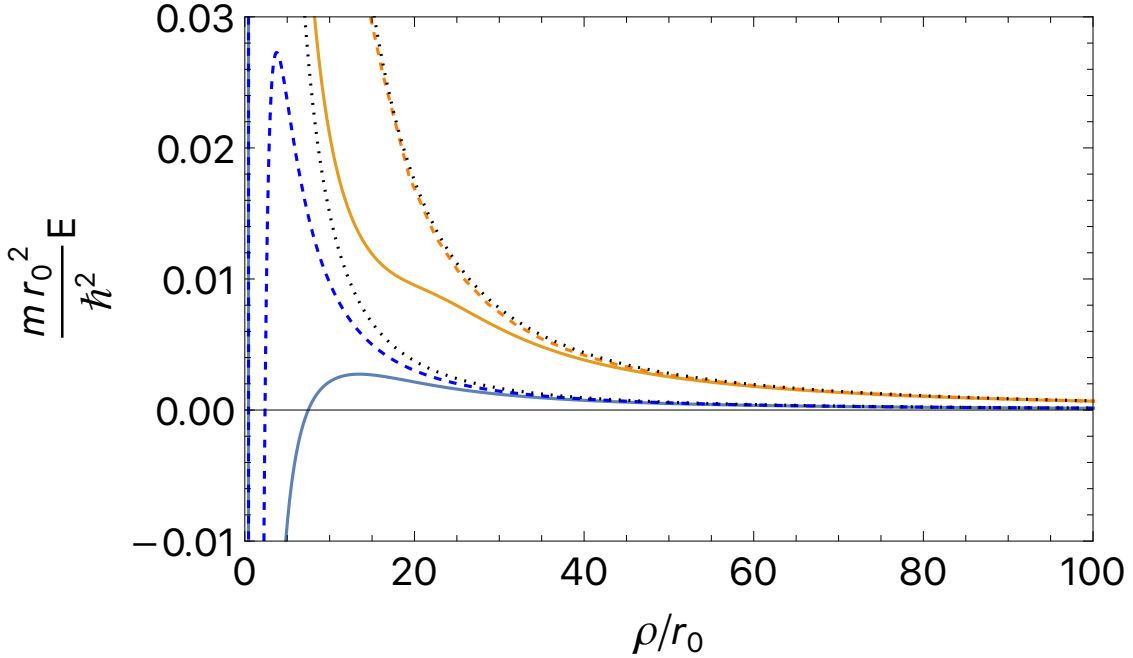


**Figure 5.9.** Comparison of lowest 2 adiabatic potentials computed by correlated gaussian basis (solid color, diagonal  $Q$  neglected, courtesy of M. Higgins) with sum symmetrized  $\phi_\nu$  (dashed color), for  $N = 4$ , using gaussian interaction with  $a_s = -4r_0$ . Black dotted lines are non-interacting potentials with  $\lambda = 0, 4$ .

Both curves begin at  $\rho = 0$  from the non-interacting limit of 12 and quickly become attractive due to the effects of interaction. The variational hyperspherical potential using gaussian interaction has a local minimum about twice as deep as that of potential from Van der Waals interaction; the potential from gaussian interaction also has a barrier about twice as high as that of the potential from Van der Waals interaction. These values of variational potential at small  $\rho$  imply different values of binding energies for the first tetramer. Ref. [99] says the gaussian interaction admits the first tetramer at  $a_s = -1.96r_0$  and the first trimer at  $a_s = -4.245r_0$ ; for Van der Waals interaction with different choices of small- $r$  cutoff, the first trimer occurs close to  $a_s = -10l_{vdw}$  [87]. However, at large  $\rho$ , both blue and red curves approximately converge to the same constant value. Once again fitting these curves at large  $\rho > 10r_0$  to a form  $A + B\rho + \frac{C}{\rho}$ , gaussian interaction gives  $A = 1.86$  and soft-core

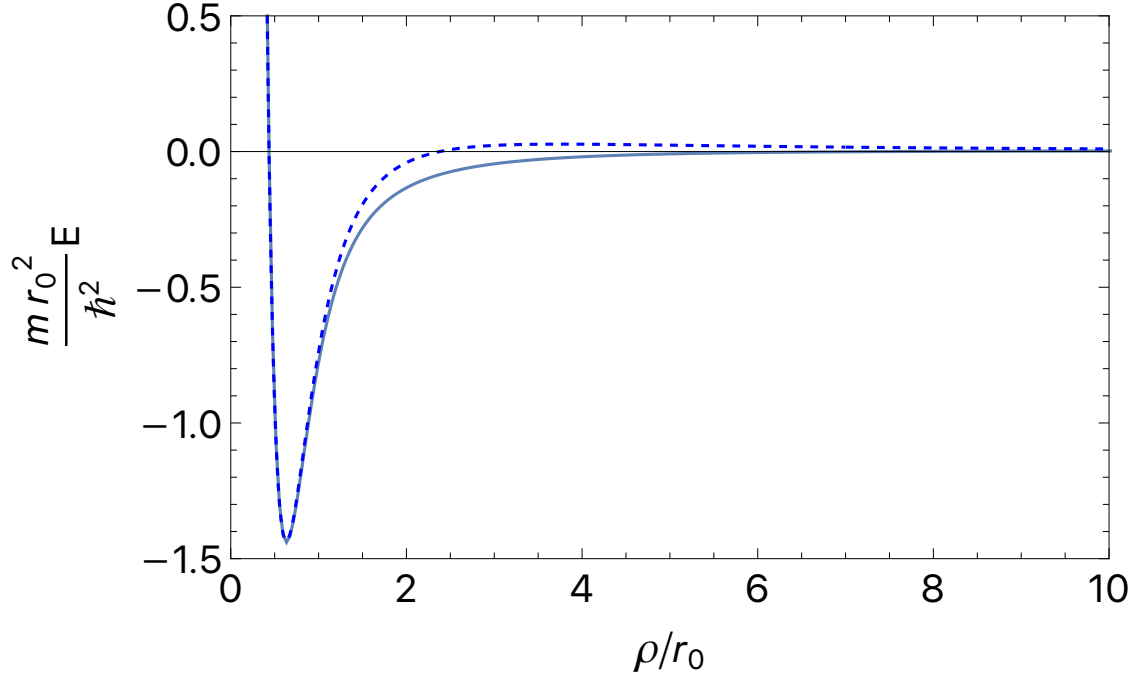


**Figure 5.10.** Comparison of lowest adiabatic potential computed by correlated gaussian basis (solid,  $Q$  neglected, courtesy of M. Higgins) with sum symmetrized  $\phi_a$  (dashed), for  $N = 4$ , using gaussian interaction with  $a_s = -4r_0$ .

Van der Waals gives  $A = 1.85$ . Our theory therefore predicts asymptotically an effectively repulsive  $\rho^{-2}$  potential for 4 unitary bosons without an external trap, in disagreement with the prediction of Ref. [78].

Next, in Fig. 5.9, we compare the 2 lowest adiabatic hyperspherical potentials for 4 bosons with gaussian interaction,  $a_s = -4r_0$ , using correlated gaussian diagonalization procedure (solid color, courtesy of Michael Higgins) and using our sum-symmetrized ansatz  $\phi_\nu$  (dashed color). Black dotted lines are the two lowest non-interacting potentials with  $\lambda = 0$  and 4. Because the first trimer occurs at  $a_s = -4.245r_0$  [99], there is no bound cluster threshold for a potential to converge to; therefore, our ansatz must provide an upper bound on the correct lowest hyperspherical potential. Because  $a_s$  is small, the second potential from our ansatz is hardly different from the non-interacting limit, while the first potential has the characteristic peak and minimum as discussed previously.

Now observe the results obtained by diagonalizing  $H_{ad}$  using correlated gaussians. The lowest potential has a barrier far lower than that predicted by our ansatz. An analysis

of  $N = 3$  hyperspherical potential for  $a_s = -4r_0$  reveals that while there is no trimer, a shape resonance occurs at  $E \approx 5 \times 10^{-3} \frac{\hbar^2}{mr_0^2}$ . Indeed, in that energy range, there is a broad avoided crossing between the solid blue and orange curves; the orange curve crosses over from  $\lambda = 0$  non-interacting potential to  $\lambda = 4$  non-interacting potential. Meanwhile, our ansatz approach does correctly describe the local minimum of the lowest potential curve, as seen in Fig. 5.10. Our ansatz predicts one tetramer at  $E = -0.364 \frac{\hbar^2}{mr_0^2}$ ; the correlated gaussian potential gives tetramer  $E = -0.399 \frac{\hbar^2}{mr_0^2}$ .

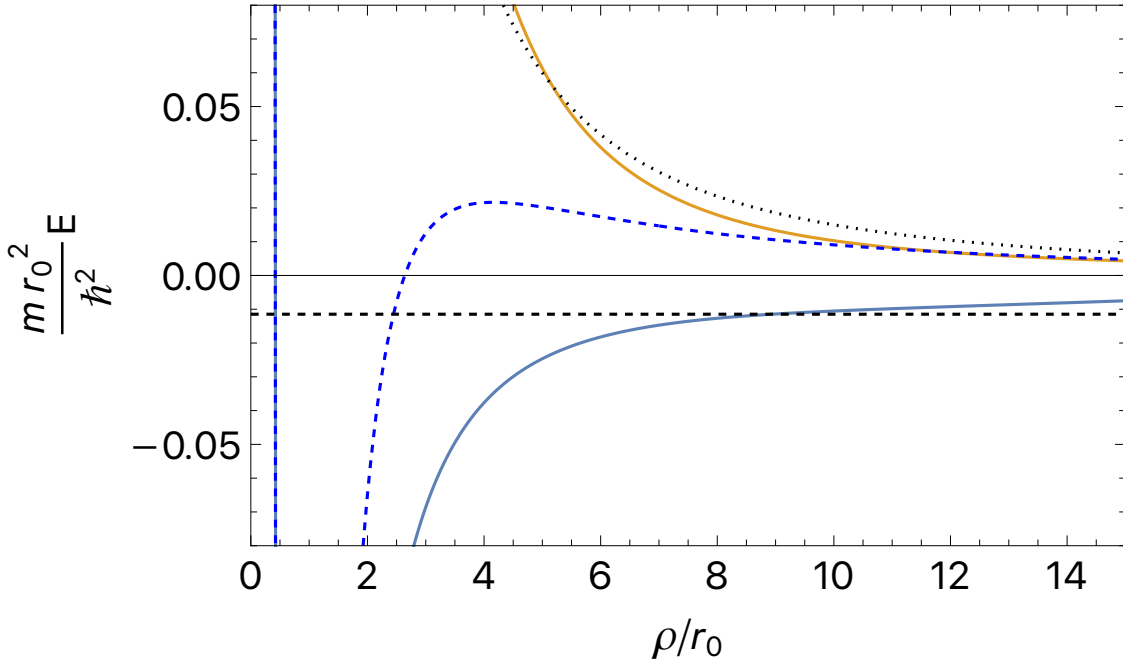


**Figure 5.11.** Comparison of lowest 2 adiabatic potentials computed by correlated gaussian basis (solid color, diagonal  $Q$  neglected, courtesy of M. Higgins) with lowest sum symmetrized  $\phi_\nu$  potential (dashed blue), for  $N = 4$ , using gaussian interaction with  $a_s = -5r_0$ . Black dotted line is non-interacting potential with  $\lambda = 0$ . Black dashed line is the trimer threshold at  $E = -0.01147 \frac{\hbar^2}{mr_0^2}$ .

Consider next the results of Fig. 5.11, which show the adiabatic hyperspherical potentials of 4 bosons with  $a_s = -5r_0$ . Now the interaction is strong enough to support one trimer at  $E = -0.01147 \frac{\hbar^2}{mr_0^2}$ , designated as a horizontal black dashed line. The blue solid curve from correlated gaussian diagonalization approximately approaches the trimer threshold, even though we believe the calculations are not quite converged. This time, our ansatz

potential closely follows the lowest curve down to the local minimum, but then it crosses over to the second potential (solid orange) given by correlated gaussians, converging at the continuum threshold. Indeed, our ansatz functions  $\phi_\nu$  were never designed to model any kind of a cluster state, but suited for interacting, unbound particles instead (or universal dimers if  $a_s > 0$ ). Our ansatz potential predicts one tetramer at  $E = -0.504 \frac{\hbar^2}{mr_0^2}$ ; the correlated gaussian potential (solid blue) predicts *two* tetramers at  $E = -0.536 \frac{\hbar^2}{mr_0^2}$  and  $E = -0.023 \frac{\hbar^2}{mr_0^2}$ , consistent with the predictions of Ref. [81].

#### 5.4 Asymptotic Potentials of Unitary Bosons

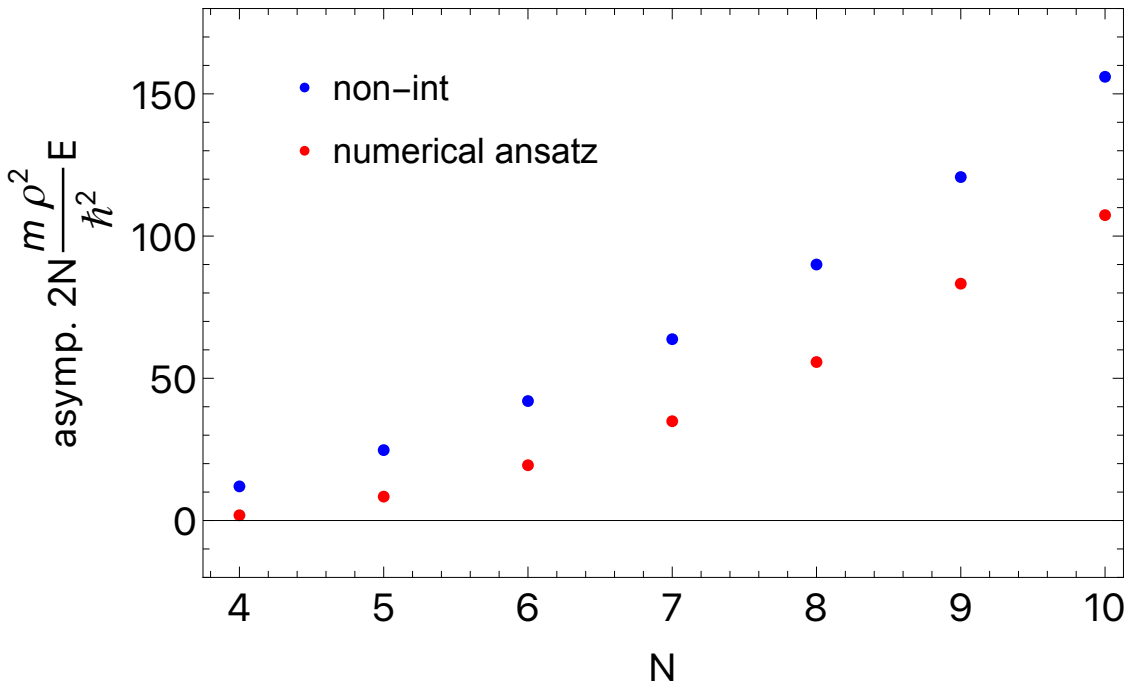


**Figure 5.12.** Asymptotic values of coefficients of  $\frac{\hbar^2}{2mN\rho^2}$  for the lowest ansatz variational potential (red) near unitarity, compared with “mock” centrifugal non-interacting coefficient  $\frac{(3N-4)(3N-6)}{4}$  (blue).

Finally, we present new results that predict the asymptotic form of the adiabatic hyperspherical potentials for unitary Bose gas of modest particle numbers. These results are compared with the well-known “mock” centrifugal potential  $\frac{\hbar^2}{2mN\rho^2} \left( \frac{(3N-4)(3N-6)}{4} \right)$ , which ef-

fectively keeps  $N$  non-interacting bosons far from each other in the absence of a central trap.

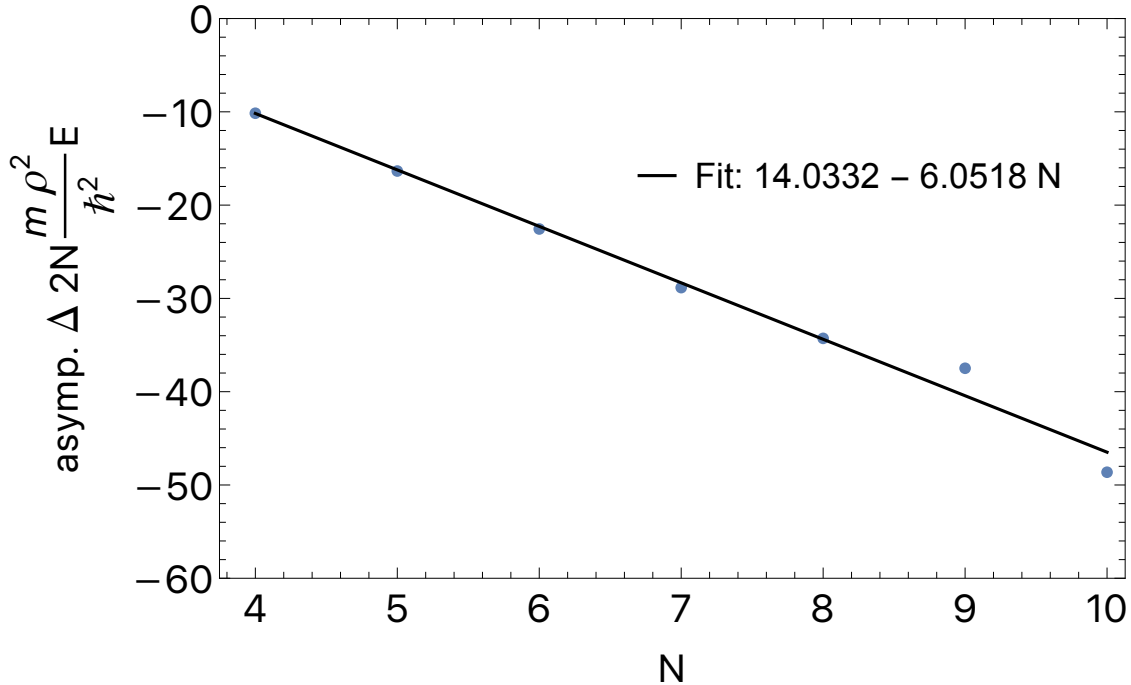


**Figure 5.13.** Difference between the two asymptotic coefficient values of Fig. 5.12, compared with a linear fit.

Fig. 5.12 shows our results for the asymptotic coefficients (red dots) of  $\rho^{-2}$  of the lowest variational adiabatic hyperspherical potential of  $N$  bosons in comparison with the “mock”-centrifugal values (blue dots)  $\frac{(3N-4)(3N-6)}{4}$ . We obtained these results by computing the lowest sum-symmetrized ansatz for each  $N$  with a soft-core Van der Waals interaction that is tuned to give  $a_s = -10,000l_{vdw}$ . Then, for values of  $\rho$  from 7 to  $500l_{vdw}$ , we fit the potentials multiplied by  $2N(\rho/l_{vdw})^2$  to a form  $A + B\rho + \frac{C}{\rho}$  to extract the coefficient  $A$ . We again emphasize that the fitting function is not to be directly extrapolated for large  $\rho$ . The linear term in  $\rho$  is merely a correction to account for the finite value of  $a_s$  (see Eqn. 4.27).

Fig. 5.13 shows the difference between our unitary values and the “mock”-centrifugal values for the coefficients; they are reasonably well described by a linear fit. The noticeable deviation of values for  $N = 9$  and  $10$  from the linear fit is probably due to the potentials

being not quite converged. Again, our predictions disagree with the prediction of Ref. [78], which claims that the unitary value of coefficient is attractive and scales as  $N^2$ .

## 5.5 Summary and Outlook

In the previous Ch. 4 and this chapter, we have explored a new method to approximately compute the variational adiabatic hyperspherical potentials that converge to the scattering continuum for particle numbers up to 10, treating quite a different regime from the Diffusion Monte Carlo results of D. Blume [88], [89] for the lowest potential that converges to a cluster state. Based on the known methods of Faddeev decomposition, we constructed a numerical two-body function that explicitly takes the zero-energy scattering boundary condition into account and approximately solves the adiabatic Hamiltonian outside the coalescence region.

For  $N = 3$ , we performed both sum-symmetrization and product-symmetrization, akin to the methods of Faddeev and Jastrow, and verified that product-symmetrized wavefunction does a superior job of describing the lowest hyperspherical potential that leads to Efimov trimers, because all three particles must simultaneously act on one another for a trimer to form. For the product-symmetrized ansatz, we verified the assumptions of zero-range theory, that the microscopic details of two-body interaction are irrelevant to a good degree for ultracold atoms.

For  $N > 4$ , we only treated sum-symmetrization due to computational constraints, but we obtain reasonable pictures for how the hyperspherical potentials are modified from the non-interacting limit due to pairwise interaction. We observe that the small-hyperradius behavior of the variational potential, and hence the local well and barrier, are dependent on the particular two-body interaction under consideration. In particular, we have compared our ansatz results with the results of direct adiabatic Hamiltonian diagonalization using correlated gaussians for  $N = 4$ . We observed how our ansatz ignores the realistic avoided-crossing structures of the hyperspherical potentials if there is a shape resonance for a trimer; if a real trimer can be supported by the two-body interaction, then our ansatz variational potential diabatically crosses over from the lowest to the 1st excited potential obtained by diagonalization.

Finally, we present new results on the asymptotic behavior of  $N > 3$  unitary bosons, which partially verify the results of Ref. [80] that there is no true Efimov effect for more than 3 bosons. We obtain repulsive  $\rho^{-2}$  asymptotic potentials for unitary bosons, though there is a linear, negative discrepancy from the non-interacting limit for the coefficient of  $\rho^{-2}$  in disagreement with a result in literature [78].

The materials of previous Ch. 4 and this chapter are not yet published, and we still have much work to do to verify our initial findings and build on new results. In particular, we would like to understand the behavior of our ansatz potentials in the presence of a spherical trap and compare with mean-field theory for modest number of bosons. We are currently working to verify and compare our unitary Bose gas results with correlated gaussian predictions for  $N = 4$ . Finally, we are working to fully map out the predictions of our methodology in the regime where an  $N$ -th bound state first appears, in order to look for any possible universal relations between the values of scattering length where such clusters emerge.

## REFERENCES

- [1] L. S. Rodberg and R. M. Thaler, *Introduction to the Quantum Theory of Scattering*, 1st. New York: Academic Press, 1967.
- [2] H. Friedrich, *Scattering Theory*. Springer Berlin Heidelberg, 2015, ISBN: 9783662485262.
- [3] G. Arfken, H. Weber, and F. Harris, *Mathematical Methods for Physicists: A Comprehensive Guide*. Elsevier Science, 2011, ISBN: 9780123846556. [Online]. Available: <https://books.google.com/books?id=JOpHkJF-qcwC>.
- [4] E. Braaten and H.-W. Hammer, “Universality in few-body systems with large scattering length,” *Physics Reports*, vol. 428, no. 5, pp. 259–390, 2006, ISSN: 0370-1573. DOI: <https://doi.org/10.1016/j.physrep.2006.03.001>. [Online]. Available: <https://www.sciencedirect.com/science/article/pii/S0370157306000822>.
- [5] E. Fermi, “Sopra lo spostamento per pressione delle righe elevate delle serie spettrali,” *Il Nuovo Cimento (1924-1942)*, vol. 11, no. 3, p. 157, 1934, ISSN: 1827-6121. DOI: [10.1007/BF02959829](https://doi.org/10.1007/BF02959829). [Online]. Available: <https://doi.org/10.1007/BF02959829>.
- [6] K. Huang, *Statistical Mechanics*, 2nd. John Wiley and Sons, 1987.
- [7] S. T. Rittenhouse, N. P. Mehta, and C. H. Greene, “Green’s functions and the adiabatic hyperspherical method,” *Phys. Rev. A*, vol. 82, p. 022706, 2 Aug. 2010. DOI: [10.1103/PhysRevA.82.022706](https://doi.org/10.1103/PhysRevA.82.022706). [Online]. Available: <https://link.aps.org/doi/10.1103/PhysRevA.82.022706>.
- [8] C. Chin, R. Grimm, P. Julienne, and E. Tiesinga, “Feshbach resonances in ultracold gases,” *Rev. Mod. Phys.*, vol. 82, pp. 1225–1286, 2 Apr. 2010. DOI: [10.1103/RevModPhys.82.1225](https://doi.org/10.1103/RevModPhys.82.1225). [Online]. Available: <https://link.aps.org/doi/10.1103/RevModPhys.82.1225>.
- [9] M. H. Anderson, J. R. Ensher, M. R. Matthews, C. E. Wieman, and E. A. Cornell, “Observation of bose-einstein condensation in a dilute atomic vapor,” *Science*, vol. 269, no. 5221, pp. 198–201, 1995, ISSN: 0036-8075. DOI: [10.1126/science.269.5221.198](https://doi.org/10.1126/science.269.5221.198). eprint: <https://science.sciencemag.org/content/269/5221/198.full.pdf>. [Online]. Available: <https://science.sciencemag.org/content/269/5221/198>.
- [10] K. B. Davis, M. O. Mewes, M. R. Andrews, *et al.*, “Bose-einstein condensation in a gas of sodium atoms,” *Phys. Rev. Lett.*, vol. 75, pp. 3969–3973, 22 Nov. 1995. DOI: [10.1103/PhysRevLett.75.3969](https://doi.org/10.1103/PhysRevLett.75.3969). [Online]. Available: <https://link.aps.org/doi/10.1103/PhysRevLett.75.3969>.

- [11] C. C. Bradley, C. A. Sackett, J. J. Tollett, and R. G. Hulet, “Evidence of bose-einstein condensation in an atomic gas with attractive interactions,” *Phys. Rev. Lett.*, vol. 75, pp. 1687–1690, 9 Aug. 1995. DOI: [10.1103/PhysRevLett.75.1687](https://doi.org/10.1103/PhysRevLett.75.1687). [Online]. Available: <https://link.aps.org/doi/10.1103/PhysRevLett.75.1687>.
- [12] B. D. Esry, C. H. Greene, and J. P. Burke, “Recombination of three atoms in the ultracold limit,” *Phys. Rev. Lett.*, vol. 83, pp. 1751–1754, 9 Aug. 1999. DOI: [10.1103/PhysRevLett.83.1751](https://doi.org/10.1103/PhysRevLett.83.1751). [Online]. Available: <https://link.aps.org/doi/10.1103/PhysRevLett.83.1751>.
- [13] T. Weber, J. Herbig, M. Mark, H.-C. Nägerl, and R. Grimm, “Three-body recombination at large scattering lengths in an ultracold atomic gas,” *Phys. Rev. Lett.*, vol. 91, p. 123 201, 12 Sep. 2003. DOI: [10.1103/PhysRevLett.91.123201](https://doi.org/10.1103/PhysRevLett.91.123201). [Online]. Available: <https://link.aps.org/doi/10.1103/PhysRevLett.91.123201>.
- [14] D. S. Jin, J. R. Ensher, M. R. Matthews, C. E. Wieman, and E. A. Cornell, “Collective excitations of a bose-einstein condensate in a dilute gas,” *Phys. Rev. Lett.*, vol. 77, pp. 420–423, 3 Jul. 1996. DOI: [10.1103/PhysRevLett.77.420](https://doi.org/10.1103/PhysRevLett.77.420). [Online]. Available: <https://link.aps.org/doi/10.1103/PhysRevLett.77.420>.
- [15] J. Steinhauer, R. Ozeri, N. Katz, and N. Davidson, “Excitation spectrum of a bose-einstein condensate,” *Phys. Rev. Lett.*, vol. 88, p. 120 407, 12 Mar. 2002. DOI: [10.1103/PhysRevLett.88.120407](https://doi.org/10.1103/PhysRevLett.88.120407). [Online]. Available: <https://link.aps.org/doi/10.1103/PhysRevLett.88.120407>.
- [16] S. E. Pollack, D. Dries, R. G. Hulet, *et al.*, “Collective excitation of a bose-einstein condensate by modulation of the atomic scattering length,” *Phys. Rev. A*, vol. 81, p. 053 627, 5 May 2010. DOI: [10.1103/PhysRevA.81.053627](https://doi.org/10.1103/PhysRevA.81.053627). [Online]. Available: <https://link.aps.org/doi/10.1103/PhysRevA.81.053627>.
- [17] D. Blume and C. H. Greene, “Fermi pseudopotential approximation: Two particles under external confinement,” *Phys. Rev. A*, vol. 65, p. 043 613, 4 Apr. 2002. DOI: [10.1103/PhysRevA.65.043613](https://doi.org/10.1103/PhysRevA.65.043613). [Online]. Available: <https://link.aps.org/doi/10.1103/PhysRevA.65.043613>.
- [18] F. Dalfovo, S. Giorgini, L. P. Pitaevskii, and S. Stringari, “Theory of bose-einstein condensation in trapped gases,” *Rev. Mod. Phys.*, vol. 71, pp. 463–512, 3 Apr. 1999. DOI: [10.1103/RevModPhys.71.463](https://doi.org/10.1103/RevModPhys.71.463). [Online]. Available: <https://link.aps.org/doi/10.1103/RevModPhys.71.463>.
- [19] A. J. Leggett, “Bose-einstein condensation in the alkali gases: Some fundamental concepts,” *Rev. Mod. Phys.*, vol. 73, pp. 307–356, 2 Apr. 2001. DOI: [10.1103/RevModPhys.73.307](https://doi.org/10.1103/RevModPhys.73.307). [Online]. Available: <https://link.aps.org/doi/10.1103/RevModPhys.73.307>.

- [20] T. D. Lee, K. Huang, and C. N. Yang, “Eigenvalues and eigenfunctions of a bose system of hard spheres and its low-temperature properties,” *Phys. Rev.*, vol. 106, pp. 1135–1145, 6 Jun. 1957. DOI: [10.1103/PhysRev.106.1135](https://doi.org/10.1103/PhysRev.106.1135). [Online]. Available: <https://link.aps.org/doi/10.1103/PhysRev.106.1135>.
- [21] J. von Stecher and C. H. Greene, “Renormalized mean-field theory for a two-component fermi gas with  $s$ -wave interactions,” *Phys. Rev. A*, vol. 75, p. 022716, 2 Feb. 2007. DOI: [10.1103/PhysRevA.75.022716](https://doi.org/10.1103/PhysRevA.75.022716). [Online]. Available: <https://link.aps.org/doi/10.1103/PhysRevA.75.022716>.
- [22] Y. Ding and C. H. Greene, “Renormalized contact interaction in degenerate unitary bose gases,” *Phys. Rev. A*, vol. 95, p. 053602, 5 May 2017. DOI: [10.1103/PhysRevA.95.053602](https://doi.org/10.1103/PhysRevA.95.053602). [Online]. Available: <https://link.aps.org/doi/10.1103/PhysRevA.95.053602>.
- [23] P. Bader, S. Blanes, and F. Casas, “Solving the schrödinger eigenvalue problem by the imaginary time propagation technique using splitting methods with complex coefficients,” *The Journal of Chemical Physics*, vol. 139, no. 12, p. 124117, 2013. DOI: [10.1063/1.4821126](https://doi.org/10.1063/1.4821126). eprint: <https://doi.org/10.1063/1.4821126>. [Online]. Available: <https://doi.org/10.1063/1.4821126>.
- [24] R. Haberman, *Applied Partial Differential Equations: With Fourier Series and Boundary Value Problems*, ser. Featured Titles for Partial Differential Equations. PEARSON, 2013, ISBN: 9780321797056. [Online]. Available: <https://books.google.com/books?id=hGNwLgEACAAJ>.
- [25] E. A. Donley, N. R. Claussen, S. L. Cornish, J. L. Roberts, E. A. Cornell, and C. E. Wieman, “Dynamics of collapsing and exploding bose–einstein condensates,” *Nature*, vol. 412, no. 6844, pp. 295–299, 2001. DOI: [10.1038/35085500](https://doi.org/10.1038/35085500). [Online]. Available: <https://doi.org/10.1038/35085500>.
- [26] V. M. Pérez-García, H. Michinel, J. I. Cirac, M. Lewenstein, and P. Zoller, “Low energy excitations of a bose-einstein condensate: A time-dependent variational analysis,” *Phys. Rev. Lett.*, vol. 77, pp. 5320–5323, 27 Dec. 1996. DOI: [10.1103/PhysRevLett.77.5320](https://doi.org/10.1103/PhysRevLett.77.5320). [Online]. Available: <https://link.aps.org/doi/10.1103/PhysRevLett.77.5320>.
- [27] V. M. Pérez-García, H. Michinel, J. I. Cirac, M. Lewenstein, and P. Zoller, “Dynamics of bose-einstein condensates: Variational solutions of the gross-pitaevskii equations,” *Phys. Rev. A*, vol. 56, pp. 1424–1432, 2 Aug. 1997. DOI: [10.1103/PhysRevA.56.1424](https://doi.org/10.1103/PhysRevA.56.1424). [Online]. Available: <https://link.aps.org/doi/10.1103/PhysRevA.56.1424>.
- [28] A. Gammal, T. Frederico, and L. Tomio, “Critical number of atoms for attractive bose-einstein condensates with cylindrically symmetrical traps,” *Phys. Rev. A*, vol. 64, p. 055602, 5 Oct. 2001. DOI: [10.1103/PhysRevA.64.055602](https://doi.org/10.1103/PhysRevA.64.055602). [Online]. Available: <https://link.aps.org/doi/10.1103/PhysRevA.64.055602>.

- [29] A. Gammal, L. Tomio, and T. Frederico, “Critical numbers of attractive bose-einstein condensed atoms in asymmetric traps,” *Phys. Rev. A*, vol. 66, p. 043619, 4 Oct. 2002. DOI: [10.1103/PhysRevA.66.043619](https://link.aps.org/doi/10.1103/PhysRevA.66.043619). [Online]. Available: <https://link.aps.org/doi/10.1103/PhysRevA.66.043619>.
- [30] C. C. Bradley, C. A. Sackett, and R. G. Hulet, “Bose-einstein condensation of lithium: Observation of limited condensate number,” *Phys. Rev. Lett.*, vol. 78, pp. 985–989, 6 Feb. 1997. DOI: [10.1103/PhysRevLett.78.985](https://link.aps.org/doi/10.1103/PhysRevLett.78.985). [Online]. Available: <https://link.aps.org/doi/10.1103/PhysRevLett.78.985>.
- [31] C. A. Sackett, J. M. Gerton, M. Welling, and R. G. Hulet, “Measurements of collective collapse in a bose-einstein condensate with attractive interactions,” *Phys. Rev. Lett.*, vol. 82, pp. 876–879, 5 Feb. 1999. DOI: [10.1103/PhysRevLett.82.876](https://link.aps.org/doi/10.1103/PhysRevLett.82.876). [Online]. Available: <https://link.aps.org/doi/10.1103/PhysRevLett.82.876>.
- [32] J. O. Andersen, “Theory of the weakly interacting bose gas,” *Rev. Mod. Phys.*, vol. 76, pp. 599–639, 2 Jul. 2004. DOI: [10.1103/RevModPhys.76.599](https://link.aps.org/doi/10.1103/RevModPhys.76.599). [Online]. Available: <https://link.aps.org/doi/10.1103/RevModPhys.76.599>.
- [33] B. D. Esry, “Hartree-fock theory for bose-einstein condensates and the inclusion of correlation effects,” *Phys. Rev. A*, vol. 55, pp. 1147–1159, 2 Feb. 1997. DOI: [10.1103/PhysRevA.55.1147](https://link.aps.org/doi/10.1103/PhysRevA.55.1147). [Online]. Available: <https://link.aps.org/doi/10.1103/PhysRevA.55.1147>.
- [34] S. Stringari, “Collective excitations of a trapped bose-condensed gas,” *Phys. Rev. Lett.*, vol. 77, pp. 2360–2363, 12 Sep. 1996. DOI: [10.1103/PhysRevLett.77.2360](https://link.aps.org/doi/10.1103/PhysRevLett.77.2360). [Online]. Available: <https://link.aps.org/doi/10.1103/PhysRevLett.77.2360>.
- [35] F. Chevy, V. Bretin, P. Rosenbusch, K. W. Madison, and J. Dalibard, “Transverse breathing mode of an elongated bose-einstein condensate,” *Phys. Rev. Lett.*, vol. 88, p. 250402, 25 Jun. 2002. DOI: [10.1103/PhysRevLett.88.250402](https://link.aps.org/doi/10.1103/PhysRevLett.88.250402). [Online]. Available: <https://link.aps.org/doi/10.1103/PhysRevLett.88.250402>.
- [36] P. A. Ruprecht, M. J. Holland, K. Burnett, and M. Edwards, “Time-dependent solution of the nonlinear schrödinger equation for bose-condensed trapped neutral atoms,” *Phys. Rev. A*, vol. 51, pp. 4704–4711, 6 Jun. 1995. DOI: [10.1103/PhysRevA.51.4704](https://link.aps.org/doi/10.1103/PhysRevA.51.4704). [Online]. Available: <https://link.aps.org/doi/10.1103/PhysRevA.51.4704>.
- [37] M. Edwards, P. A. Ruprecht, K. Burnett, R. J. Dodd, and C. W. Clark, “Collective excitations of atomic bose-einstein condensates,” *Phys. Rev. Lett.*, vol. 77, pp. 1671–1674, 9 Aug. 1996. DOI: [10.1103/PhysRevLett.77.1671](https://link.aps.org/doi/10.1103/PhysRevLett.77.1671). [Online]. Available: <https://link.aps.org/doi/10.1103/PhysRevLett.77.1671>.

- [38] P. A. Ruprecht, M. Edwards, K. Burnett, and C. W. Clark, “Probing the linear and nonlinear excitations of bose-condensed neutral atoms in a trap,” *Phys. Rev. A*, vol. 54, pp. 4178–4187, 5 Nov. 1996. DOI: [10.1103/PhysRevA.54.4178](https://doi.org/10.1103/PhysRevA.54.4178). [Online]. Available: <https://link.aps.org/doi/10.1103/PhysRevA.54.4178>.
- [39] F. Dalfovo and S. Stringari, “Bosons in anisotropic traps: Ground state and vortices,” *Phys. Rev. A*, vol. 53, pp. 2477–2485, 4 Apr. 1996. DOI: [10.1103/PhysRevA.53.2477](https://doi.org/10.1103/PhysRevA.53.2477). [Online]. Available: <https://link.aps.org/doi/10.1103/PhysRevA.53.2477>.
- [40] H. Shi and W.-M. Zheng, “Bose-einstein condensation in an atomic gas with attractive interactions,” *Phys. Rev. A*, vol. 55, pp. 2930–2934, 4 Apr. 1997. DOI: [10.1103/PhysRevA.55.2930](https://doi.org/10.1103/PhysRevA.55.2930). [Online]. Available: <https://link.aps.org/doi/10.1103/PhysRevA.55.2930>.
- [41] M. Olshanii, “Atomic scattering in the presence of an external confinement and a gas of impenetrable bosons,” *Phys. Rev. Lett.*, vol. 81, pp. 938–941, 5 Aug. 1998. DOI: [10.1103/PhysRevLett.81.938](https://doi.org/10.1103/PhysRevLett.81.938). [Online]. Available: <https://link.aps.org/doi/10.1103/PhysRevLett.81.938>.
- [42] T. Kinoshita, T. Wenger, and D. S. Weiss, “A quantum newton’s cradle,” *Nature*, vol. 440, no. 7086, pp. 900–903, 2006. DOI: [10.1038/nature04693](https://doi.org/10.1038/nature04693). [Online]. Available: <https://doi.org/10.1038/nature04693>.
- [43] L. Khaykovich, F. Schreck, G. Ferrari, *et al.*, “Formation of a matter-wave bright soliton,” *Science*, vol. 296, no. 5571, pp. 1290–1293, 2002, ISSN: 0036-8075. DOI: [10.1126/science.1071021](https://doi.org/10.1126/science.1071021).
- [44] K. E. Strecker, G. B. Partridge, A. G. Truscott, and R. G. Hulet, “Formation and propagation of matter-wave soliton trains,” *Nature*, vol. 417, no. 6885, pp. 150–153, 2002. DOI: [10.1038/nature747](https://doi.org/10.1038/nature747). [Online]. Available: <https://doi.org/10.1038/nature747>.
- [45] H. Lee and C. H. Greene, “Orbital variational adiabatic hyperspherical method applied to bose-einstein condensates,” *Phys. Rev. A*, vol. 103, p. 023 325, 2 Feb. 2021. DOI: [10.1103/PhysRevA.103.023325](https://doi.org/10.1103/PhysRevA.103.023325). [Online]. Available: <https://link.aps.org/doi/10.1103/PhysRevA.103.023325>.
- [46] T. K. Das and B. Chakrabarti, “Potential harmonics expansion method for trapped interacting bosons: Inclusion of two-body correlation,” *Phys. Rev. A*, vol. 70, p. 063 601, 6 Dec. 2004. DOI: [10.1103/PhysRevA.70.063601](https://doi.org/10.1103/PhysRevA.70.063601). [Online]. Available: <https://link.aps.org/doi/10.1103/PhysRevA.70.063601>.
- [47] B. Chakrabarti, A. Kundu, and T. K. Das, “A finite number of trapped interacting bosons: An approximate many-body calculation,” *Journal of Physics B: Atomic, Molecular and Optical Physics*, vol. 38, no. 14, pp. 2457–2466, Jun. 2005. DOI: [10.1088/0953-4075/38/14/010](https://doi.org/10.1088/0953-4075/38/14/010). [Online]. Available: <https://doi.org/10.1088/0953-4075/38/14/010>.

- [48] M. Viviani, A. Kievsky, and S. Rosati, “Calculation of the  $\alpha$ -particle ground state within the hyperspherical harmonic basis,” *Phys. Rev. C*, vol. 71, p. 024006, 2 Feb. 2005. DOI: [10.1103/PhysRevC.71.024006](https://doi.org/10.1103/PhysRevC.71.024006). [Online]. Available: <https://link.aps.org/doi/10.1103/PhysRevC.71.024006>.
- [49] L. E. Marcucci, A. Kievsky, L. Girlanda, S. Rosati, and M. Viviani, “ $N-d$  Elastic scattering using the hyperspherical harmonics approach with realistic local and nonlocal interactions,” *Phys. Rev. C*, vol. 80, p. 034003, 3 Sep. 2009. DOI: [10.1103/PhysRevC.80.034003](https://doi.org/10.1103/PhysRevC.80.034003). [Online]. Available: <https://link.aps.org/doi/10.1103/PhysRevC.80.034003>.
- [50] J. L. Bohn, B. D. Esry, and C. H. Greene, “Effective potentials for dilute bose-einstein condensates,” *Phys. Rev. A*, vol. 58, pp. 584–597, 1 Jul. 1998. DOI: [10.1103/PhysRevA.58.584](https://doi.org/10.1103/PhysRevA.58.584). [Online]. Available: <https://link.aps.org/doi/10.1103/PhysRevA.58.584>.
- [51] Y. E. Kim and A. L. Zubarev, “Equivalent linear two-body method for many-body problems,” *Journal of Physics B: Atomic, Molecular and Optical Physics*, vol. 33, no. 1, pp. 55–69, Dec. 1999. DOI: [10.1088/0953-4075/33/1/306](https://doi.org/10.1088/0953-4075/33/1/306). [Online]. Available: <https://doi.org/10.1088%2F0953-4075%2F33%2F1%2F306>.
- [52] D. Kushibe, M. Mutou, T. Morishita, S. Watanabe, and M. Matsuzawa, “Aspects of hyperspherical adiabaticity in an atomic-gas bose-einstein condensate,” *Phys. Rev. A*, vol. 70, p. 063617, 6 Dec. 2004. DOI: [10.1103/PhysRevA.70.063617](https://doi.org/10.1103/PhysRevA.70.063617). [Online]. Available: <https://link.aps.org/doi/10.1103/PhysRevA.70.063617>.
- [53] S. T. Rittenhouse, M. J. Cavagnero, J. von Stecher, and C. H. Greene, “Hyperspherical description of the degenerate fermi gas:  $s$ -wave interactions,” *Phys. Rev. A*, vol. 74, p. 053624, 5 Nov. 2006. DOI: [10.1103/PhysRevA.74.053624](https://doi.org/10.1103/PhysRevA.74.053624). [Online]. Available: <https://link.aps.org/doi/10.1103/PhysRevA.74.053624>.
- [54] S. T. Rittenhouse, M. J. Cavagnero, and C. H. Greene, “Collective coordinate description of anisotropically trapped degenerate fermi gases,” *The Journal of Physical Chemistry A*, vol. 113, no. 52, pp. 15016–15023, 2009, PMID: 19899802. DOI: [10.1021/jp9051006](https://doi.org/10.1021/jp9051006). eprint: <https://doi.org/10.1021/jp9051006>. [Online]. Available: <https://doi.org/10.1021/jp9051006>.
- [55] E. J. Halperin and J. L. Bohn, “Hyperspherical approach to dipolar droplets beyond the mean-field limit,” *Phys. Rev. A*, vol. 104, p. 033324, 3 Sep. 2021. DOI: [10.1103/PhysRevA.104.033324](https://doi.org/10.1103/PhysRevA.104.033324). [Online]. Available: <https://link.aps.org/doi/10.1103/PhysRevA.104.033324>.
- [56] A. W. Weiss, “Configuration interaction in simple atomic systems,” *Phys. Rev.*, vol. 122, pp. 1826–1836, 6 Jun. 1961. DOI: [10.1103/PhysRev.122.1826](https://doi.org/10.1103/PhysRev.122.1826). [Online]. Available: <https://link.aps.org/doi/10.1103/PhysRev.122.1826>.

- [57] C. Cramer, *Essentials of Computational Chemistry: Theories and Models*. Wiley, 2005, ISBN: 9780470091838. [Online]. Available: <https://books.google.com/books?id=BKJcbvzI0RsC>.
- [58] D. Frame, R. He, I. Ipsen, D. Lee, D. Lee, and E. Rrapaj, “Eigenvector continuation with subspace learning,” *Phys. Rev. Lett.*, vol. 121, p. 032 501, 3 Jul. 2018. DOI: [10.1103/PhysRevLett.121.032501](https://link.aps.org/doi/10.1103/PhysRevLett.121.032501). [Online]. Available: <https://link.aps.org/doi/10.1103/PhysRevLett.121.032501>.
- [59] J. von Stecher and C. H. Greene, “Correlated gaussian hyperspherical method for few-body systems,” *Phys. Rev. A*, vol. 80, p. 022 504, 2 Aug. 2009. DOI: [10.1103/PhysRevA.80.022504](https://link.aps.org/doi/10.1103/PhysRevA.80.022504). [Online]. Available: <https://link.aps.org/doi/10.1103/PhysRevA.80.022504>.
- [60] K. M. Daily and C. H. Greene, “Extension of the correlated gaussian hyperspherical method to more particles and dimensions,” *Phys. Rev. A*, vol. 89, p. 012 503, 1 Jan. 2014. DOI: [10.1103/PhysRevA.89.012503](https://link.aps.org/doi/10.1103/PhysRevA.89.012503). [Online]. Available: <https://link.aps.org/doi/10.1103/PhysRevA.89.012503>.
- [61] Y. Suzuki and K. Varga, “Constrained correlated-gaussians for hyperspherical calculations,” *Few-Body Systems*, vol. 60, no. 1, p. 3, 2018. DOI: [10.1007/s00601-018-1470-z](https://doi.org/10.1007/s00601-018-1470-z). [Online]. Available: <https://doi.org/10.1007/s00601-018-1470-z>.
- [62] J. Wang, “Hyperspherical approach to quantal three-body theory,” Ph.D. dissertation, Boulder, 2012.
- [63] D. Bressanini and P. J. Reynolds, “Generalized variational principle for excited states using nodes of trial functions,” *Phys. Rev. E*, vol. 84, p. 046 705, 4 Oct. 2011. DOI: [10.1103/PhysRevE.84.046705](https://link.aps.org/doi/10.1103/PhysRevE.84.046705). [Online]. Available: <https://link.aps.org/doi/10.1103/PhysRevE.84.046705>.
- [64] P. Morse and H. Feshbach, *Methods of Theoretical Physics*, ser. International series in pure and applied physics. McGraw-Hill, 1953. [Online]. Available: <https://books.google.com/books?id=l8ENAQAIAAJ>.
- [65] J. Stoer and R. Bulirsch, *Introduction to Numerical Analysis*, ser. Texts in applied mathematics. Springer-Verlag, 1993, ISBN: 9780387978789. [Online]. Available: <https://books.google.com/books?id=yYyYQgAACAAJ>.
- [66] B. D. Esry and C. H. Greene, “Validity of the shape-independent approximation for bose-einstein condensates,” *Phys. Rev. A*, vol. 60, pp. 1451–1462, 2 Aug. 1999. DOI: [10.1103/PhysRevA.60.1451](https://link.aps.org/doi/10.1103/PhysRevA.60.1451). [Online]. Available: <https://link.aps.org/doi/10.1103/PhysRevA.60.1451>.

- [67] R. Santra, J. M. Shainline, and C. H. Greene, “Siegert pseudostates: Completeness and time evolution,” *Phys. Rev. A*, vol. 71, p. 032 703, 3 Mar. 2005. DOI: [10.1103/PhysRevA.71.032703](https://doi.org/10.1103/PhysRevA.71.032703). [Online]. Available: <https://link.aps.org/doi/10.1103/PhysRevA.71.032703>.
- [68] J. Macek, “Properties of autoionizing states of he,” *Journal of Physics B: Atomic and Molecular Physics*, vol. 1, no. 5, pp. 831–843, Sep. 1968. DOI: [10.1088/0022-3700/1/5/309](https://doi.org/10.1088/0022-3700/1/5/309). [Online]. Available: <https://doi.org/10.1088/0022-3700/1/5/309>.
- [69] V. Efimov, “Energy levels arising from resonant two-body forces in a three-body system,” *Physics Letters B*, vol. 33, no. 8, pp. 563–564, 1970, ISSN: 0370-2693. DOI: [https://doi.org/10.1016/0370-2693\(70\)90349-7](https://doi.org/10.1016/0370-2693(70)90349-7). [Online]. Available: <https://www.sciencedirect.com/science/article/pii/0370269370903497>.
- [70] P. Naidon and S. Endo, “Efimov physics: A review,” *Reports on Progress in Physics*, vol. 80, no. 5, p. 056 001, Mar. 2017. DOI: [10.1088/1361-6633/aa50e8](https://doi.org/10.1088/1361-6633/aa50e8). [Online]. Available: <https://doi.org/10.1088/1361-6633/aa50e8>.
- [71] C. H. Greene, P. Giannakeas, and J. Pérez-Ríos, “Universal few-body physics and cluster formation,” *Rev. Mod. Phys.*, vol. 89, p. 035 006, 3 Aug. 2017. DOI: [10.1103/RevModPhys.89.035006](https://doi.org/10.1103/RevModPhys.89.035006). [Online]. Available: <https://link.aps.org/doi/10.1103/RevModPhys.89.035006>.
- [72] L. H. Thomas, “The interaction between a neutron and a proton and the structure of  $H^3$ ,” *Phys. Rev.*, vol. 47, pp. 903–909, 12 Jun. 1935. DOI: [10.1103/PhysRev.47.903](https://doi.org/10.1103/PhysRev.47.903). [Online]. Available: <https://link.aps.org/doi/10.1103/PhysRev.47.903>.
- [73] B. D. Esry, C. D. Lin, and C. H. Greene, “Adiabatic hyperspherical study of the helium trimer,” *Phys. Rev. A*, vol. 54, pp. 394–401, 1 Jul. 1996. DOI: [10.1103/PhysRevA.54.394](https://doi.org/10.1103/PhysRevA.54.394). [Online]. Available: <https://link.aps.org/doi/10.1103/PhysRevA.54.394>.
- [74] J. P. D’Incao, “Few-body physics in resonantly interacting ultracold quantum gases,” *Journal of Physics B: Atomic, Molecular and Optical Physics*, vol. 51, no. 4, p. 043 001, Jan. 2018. DOI: [10.1088/1361-6455/aaa116](https://doi.org/10.1088/1361-6455/aaa116). [Online]. Available: <https://doi.org/10.1088/1361-6455/aaa116>.
- [75] T. Kraemer, M. Mark, P. Waldburger, *et al.*, “Evidence for efimov quantum states in an ultracold gas of caesium atoms,” *Nature*, vol. 440, no. 7082, pp. 315–318, 2006. DOI: [10.1038/nature04626](https://doi.org/10.1038/nature04626). [Online]. Available: <https://doi.org/10.1038/nature04626>.
- [76] L. Faddeev, “Scattering theory for a three-particle system,” in *Fifty Years of Mathematical Physics: Selected Works of Ludwig Faddeev*, World Scientific, 2016, pp. 37–42.
- [77] D. V. Fedorov and A. S. Jensen, “Efimov effect in coordinate space faddeev equations,” *Phys. Rev. Lett.*, vol. 71, pp. 4103–4106, 25 Dec. 1993. DOI: [10.1103/PhysRevLett.71.4103](https://doi.org/10.1103/PhysRevLett.71.4103). [Online]. Available: <https://link.aps.org/doi/10.1103/PhysRevLett.71.4103>.

- [78] O. Sørensen, D. V. Fedorov, and A. S. Jensen, “Correlated trapped bosons and the many-body efimov effect,” *Phys. Rev. Lett.*, vol. 89, p. 173002, 17 Oct. 2002. DOI: [10.1103/PhysRevLett.89.173002](https://doi.org/10.1103/PhysRevLett.89.173002). [Online]. Available: <https://link.aps.org/doi/10.1103/PhysRevLett.89.173002>.
- [79] O. Sørensen, D. V. Fedorov, and A. S. Jensen, “Two-body correlations in n-body boson systems,” *Phys. Rev. A*, vol. 66, p. 032507, 3 Sep. 2002. DOI: [10.1103/PhysRevA.66.032507](https://doi.org/10.1103/PhysRevA.66.032507). [Online]. Available: <https://link.aps.org/doi/10.1103/PhysRevA.66.032507>.
- [80] R. D. Amado and F. C. Greenwood, “There is no efimov effect for four or more particles,” *Phys. Rev. D*, vol. 7, pp. 2517–2519, 8 Apr. 1973. DOI: [10.1103/PhysRevD.7.2517](https://doi.org/10.1103/PhysRevD.7.2517). [Online]. Available: <https://link.aps.org/doi/10.1103/PhysRevD.7.2517>.
- [81] J. von Stecher, J. P. D’Incao, and C. H. Greene, “Signatures of universal four-body phenomena and their relation to the efimov effect,” *Nature Physics*, vol. 5, no. 6, pp. 417–421, 2009. DOI: [10.1038/nphys1253](https://doi.org/10.1038/nphys1253). [Online]. Available: <https://doi.org/10.1038/nphys1253>.
- [82] R. Jastrow, “Many-body problem with strong forces,” *Phys. Rev.*, vol. 98, pp. 1479–1484, 5 Jun. 1955. DOI: [10.1103/PhysRev.98.1479](https://doi.org/10.1103/PhysRev.98.1479). [Online]. Available: <https://link.aps.org/doi/10.1103/PhysRev.98.1479>.
- [83] C. J. Umrigar, K. G. Wilson, and J. W. Wilkins, “Optimized trial wave functions for quantum monte carlo calculations,” *Phys. Rev. Lett.*, vol. 60, pp. 1719–1722, 17 Apr. 1988. DOI: [10.1103/PhysRevLett.60.1719](https://doi.org/10.1103/PhysRevLett.60.1719). [Online]. Available: <https://link.aps.org/doi/10.1103/PhysRevLett.60.1719>.
- [84] M. W. C. Sze, A. G. Sykes, D. Blume, and J. L. Bohn, “Hyperspherical lowest-order constrained-variational approximation to resonant bose-einstein condensates,” *Phys. Rev. A*, vol. 97, p. 033608, 3 Mar. 2018. DOI: [10.1103/PhysRevA.97.033608](https://doi.org/10.1103/PhysRevA.97.033608). [Online]. Available: <https://link.aps.org/doi/10.1103/PhysRevA.97.033608>.
- [85] H. Suno, B. D. Esry, C. H. Greene, and J. P. Burke, “Three-body recombination of cold helium atoms,” *Phys. Rev. A*, vol. 65, p. 042725, 4 Apr. 2002. DOI: [10.1103/PhysRevA.65.042725](https://doi.org/10.1103/PhysRevA.65.042725). [Online]. Available: <https://link.aps.org/doi/10.1103/PhysRevA.65.042725>.
- [86] Y.-H. Chen and C. H. Greene, *Efimov physics implications at p-wave fermionic unitarity*, 2021. arXiv: [2109.13311](https://arxiv.org/abs/2109.13311) [[physics.atom-ph](https://arxiv.org/abs/2109.13311)].
- [87] J. Wang, J. P. D’Incao, B. D. Esry, and C. H. Greene, “Origin of the three-body parameter universality in efimov physics,” *Phys. Rev. Lett.*, vol. 108, p. 263001, 26 Jun. 2012. DOI: [10.1103/PhysRevLett.108.263001](https://doi.org/10.1103/PhysRevLett.108.263001). [Online]. Available: <https://link.aps.org/doi/10.1103/PhysRevLett.108.263001>.

- [88] D. Blume and C. H. Greene, “Monte carlo hyperspherical description of helium cluster excited states,” *The Journal of Chemical Physics*, vol. 112, no. 18, pp. 8053–8067, 2000. DOI: [10.1063/1.481404](https://doi.org/10.1063/1.481404). eprint: <https://doi.org/10.1063/1.481404>. [Online]. Available: <https://doi.org/10.1063/1.481404>.
- [89] D. Blume and C. H. Greene, “Vibrationally excited states and fragmentation geometries of neon and argon clusters,  $n=3-6$ , using hyperspherical coordinates,” *The Journal of Chemical Physics*, vol. 113, no. 10, pp. 4242–4249, 2000. DOI: [10.1063/1.1288385](https://doi.org/10.1063/1.1288385). eprint: <https://doi.org/10.1063/1.1288385>. [Online]. Available: <https://doi.org/10.1063/1.1288385>.
- [90] M. Abramowitz and I. A. Stegun, *Handbook of Mathematical Functions with Formulas, Graphs, and Mathematical Tables*, ninth Dover printing, tenth GPO printing. New York: Dover, 1964.
- [91] E. Hairer, S. Nørsett, and G. Wanner, *Solving Ordinary Differential Equations I: Non-stiff Problems*, ser. Springer Series in Computational Mathematics. Springer Berlin Heidelberg, 2010, ISBN: 9783642081583. [Online]. Available: <https://books.google.com/books?id=65ffYgEACAAJ>.
- [92] J. L. M. Quiroz González and D. Thompson, “Getting started with numerov’s method,” *Computers in Physics*, vol. 11, no. 5, pp. 514–515, 1997. DOI: [10.1063/1.168593](https://doi.org/10.1063/1.168593). eprint: <https://aip.scitation.org/doi/pdf/10.1063/1.168593>. [Online]. Available: <https://aip.scitation.org/doi/abs/10.1063/1.168593>.
- [93] E. Nielsen, D. Fedorov, A. Jensen, and E. Garrido, “The three-body problem with short-range interactions,” *Physics Reports*, vol. 347, no. 5, pp. 373–459, 2001, ISSN: 0370-1573. DOI: [https://doi.org/10.1016/S0370-1573\(00\)00107-1](https://doi.org/10.1016/S0370-1573(00)00107-1). [Online]. Available: <https://www.sciencedirect.com/science/article/pii/S0370157300001071>.
- [94] C. Robert and G. Casella, *Monte Carlo Statistical Methods*, ser. Springer Texts in Statistics. Springer New York, 2005, ISBN: 9780387212395. [Online]. Available: <https://books.google.com/books?id=HfhGAXn5GugC>.
- [95] D. Hangleiter, I. Roth, D. Nagaj, and J. Eisert, “Easing the monte carlo sign problem,” *Science Advances*, vol. 6, no. 33, eabb8341, 2020. DOI: [10.1126/sciadv.abb8341](https://doi.org/10.1126/sciadv.abb8341). eprint: <https://www.science.org/doi/pdf/10.1126/sciadv.abb8341>. [Online]. Available: <https://www.science.org/doi/abs/10.1126/sciadv.abb8341>.
- [96] H. Niederreiter, *Random Number Generation and Quasi-Monte Carlo Methods*, ser. CBMS-NSF Regional Conference Series in Applied Mathematics. Society for Industrial and Applied Mathematics, 1992, ISBN: 9781611970081.

- [97] H. Niederreiter, “Low-discrepancy and low-dispersion sequences,” *Journal of Number Theory*, vol. 30, no. 1, pp. 51–70, 1988, ISSN: 0022-314X. DOI: [https://doi.org/10.1016/0022-314X\(88\)90025-X](https://doi.org/10.1016/0022-314X(88)90025-X). [Online]. Available: <https://www.sciencedirect.com/science/article/pii/0022314X8890025X>.
- [98] A. Zenesini, B. Huang, M. Berninger, *et al.*, “Resonant five-body recombination in an ultracold gas of bosonic atoms,” *New Journal of Physics*, vol. 15, no. 4, p. 043 040, Apr. 2013. DOI: [10.1088/1367-2630/15/4/043040](https://doi.org/10.1088/1367-2630/15/4/043040). [Online]. Available: <https://doi.org/10.1088/1367-2630/15/4/043040>.
- [99] S. Moszkowski, S. Fleck, A. Kriek, L. Theußl, J.-M. Richard, and K. Varga, “Binding three or four bosons without bound subsystems,” *Phys. Rev. A*, vol. 62, p. 032 504, 3 Aug. 2000. DOI: [10.1103/PhysRevA.62.032504](https://doi.org/10.1103/PhysRevA.62.032504). [Online]. Available: <https://link.aps.org/doi/10.1103/PhysRevA.62.032504>.
- [100] K. M. Daily, “Hyperspherical asymptotics of a system of four charged particles,” *Few-Body Systems*, vol. 56, no. 11, pp. 809–822, 2015. DOI: [10.1007/s00601-015-0979-7](https://doi.org/10.1007/s00601-015-0979-7). [Online]. Available: <https://doi.org/10.1007/s00601-015-0979-7>.
- [101] J. Avery, *Hyperspherical Harmonics: Applications in Quantum Theory*, ser. Reidel Texts in the Mathematical Sciences. Springer Netherlands, 1989, ISBN: 9780792301653. [Online]. Available: <https://books.google.com/books?id=Fj9BCEjUYWgC>.
- [102] L. Delves, “Effective range expansion of the scattering matrix,” *Nuclear Physics*, vol. 8, pp. 358–373, 1958, ISSN: 0029-5582. DOI: [https://doi.org/10.1016/0029-5582\(58\)90162-7](https://doi.org/10.1016/0029-5582(58)90162-7). [Online]. Available: <https://www.sciencedirect.com/science/article/pii/0029558258901627>.
- [103] L. Delves, “Tertiary and general-order collisions,” *Nuclear Physics*, vol. 9, no. 3, pp. 391–399, 1958, ISSN: 0029-5582. DOI: [https://doi.org/10.1016/0029-5582\(58\)90372-9](https://doi.org/10.1016/0029-5582(58)90372-9). [Online]. Available: <https://www.sciencedirect.com/science/article/pii/0029558258903729>.
- [104] L. Delves, “Tertiary and general-order collisions (ii),” *Nuclear Physics*, vol. 20, pp. 275–308, 1960, ISSN: 0029-5582. DOI: [https://doi.org/10.1016/0029-5582\(60\)90174-7](https://doi.org/10.1016/0029-5582(60)90174-7). [Online]. Available: <https://www.sciencedirect.com/science/article/pii/0029558260901747>.
- [105] F. T. Smith, “A symmetric representation for three-body problems. i. motion in a plane,” *Journal of Mathematical Physics*, vol. 3, no. 4, pp. 735–748, 1962. DOI: [10.1063/1.1724275](https://doi.org/10.1063/1.1724275). eprint: <https://doi.org/10.1063/1.1724275>. [Online]. Available: <https://doi.org/10.1063/1.1724275>.
- [106] R. C. Whitten and F. T. Smith, “Symmetric representation for three-body problems. ii. motion in space,” *Journal of Mathematical Physics*, vol. 9, no. 7, pp. 1103–1113, 1968. DOI: [10.1063/1.1664683](https://doi.org/10.1063/1.1664683). eprint: <https://doi.org/10.1063/1.1664683>. [Online]. Available: <https://doi.org/10.1063/1.1664683>.

- [107] B. R. Johnson, “On hyperspherical coordinates and mapping the internal configurations of a three body system,” *The Journal of Chemical Physics*, vol. 73, no. 10, pp. 5051–5058, 1980. DOI: [10.1063/1.439983](https://doi.org/10.1063/1.439983). eprint: <https://doi.org/10.1063/1.439983>. [Online]. Available: <https://doi.org/10.1063/1.439983>.
- [108] B. R. Johnson, “The classical dynamics of three particles in hyperspherical coordinates,” *The Journal of Chemical Physics*, vol. 79, no. 4, pp. 1906–1915, 1983. DOI: [10.1063/1.445969](https://doi.org/10.1063/1.445969). eprint: <https://doi.org/10.1063/1.445969>. [Online]. Available: <https://doi.org/10.1063/1.445969>.
- [109] B. R. Johnson, “The quantum dynamics of three particles in hyperspherical coordinates,” *The Journal of Chemical Physics*, vol. 79, no. 4, pp. 1916–1925, 1983. DOI: [10.1063/1.445970](https://doi.org/10.1063/1.445970). eprint: <https://doi.org/10.1063/1.445970>. [Online]. Available: <https://doi.org/10.1063/1.445970>.
- [110] J. J. Sakurai and J. Napolitano, *Modern Quantum Mechanics*, 2nd ed. Cambridge University Press, 2017. DOI: [10.1017/9781108499996](https://doi.org/10.1017/9781108499996).
- [111] J. Taylor, *Classical Mechanics*. University Science Books, 2005, ISBN: 9781891389221. [Online]. Available: <https://books.google.com/books?id=P1kCtNr-pJsC>.
- [112] S. T. Rittenhouse, J. von Stecher, J. P. D’Incao, N. P. Mehta, and C. H. Greene, “The hyperspherical four-fermion problem,” *Journal of Physics B: Atomic, Molecular and Optical Physics*, vol. 44, no. 17, p. 172001, Aug. 2011. DOI: [10.1088/0953-4075/44/17/172001](https://doi.org/10.1088/0953-4075/44/17/172001). [Online]. Available: <https://doi.org/10.1088/0953-4075/44/17/172001>.
- [113] W. Press, S. Teukolsky, W. Vetterling, and B. Flannery, *Numerical Recipes 3rd Edition: The Art of Scientific Computing*. Cambridge University Press, 2007, ISBN: 9780521880688. [Online]. Available: <https://books.google.com/books?id=1aAOdzK3FegC>.

## A. JACOBI VECTORS OF $N$ PARTICLES

Consider  $N$  identical particles with position vectors  $\vec{r}_i$ . If one were to remove the center of mass  $\vec{R}_{CM} = \frac{1}{N} \sum_{i=1}^N \vec{r}_i$ , then one must choose a particular ‘‘Jacobi tree’’ of  $N - 1$  relative Jacobi vectors. Though different mass scaling conventions exist in certain applications with a fixed number of particles [71], here we modify an alternate convention [84] that is more easily generalizable for variable number of identical particles.

Before we proceed, it helps to first note that, because  $\left(\sum_{i=1}^N \vec{r}_i\right)^2 = \sum_{i=1}^N r_i^2 + 2 \sum_{i<j}^N \vec{r}_i \cdot \vec{r}_j$  and  $\sum_{i<j}^N r_{i,j}^2 = (N-1) \sum_{i=1}^N r_i^2 - 2 \sum_{i<j}^N \vec{r}_i \cdot \vec{r}_j$ , therefore  $\sum_{i=1}^N r_i^2 = \frac{1}{N} \sum_{i<j}^N r_{i,j}^2 + NR_{CM}^2$ .

Unless otherwise stated, this dissertation employs the following default, natural choice of Jacobi tree (referred to as the K-type in the context of 4 particles in Ref. [100]) with Jacobi vectors

$$\vec{\eta}_k = \sqrt{\frac{k}{k+1}} \left( \vec{r}_{k+1} - \frac{1}{k} \sum_{j=1}^k \vec{r}_j \right), \quad k = 1, \dots, N-1. \quad (\text{A.1})$$

For example,  $\vec{\eta}_1 = \sqrt{\frac{1}{2}} (\vec{r}_2 - \vec{r}_1)$ , and  $\vec{\eta}_2 = \sqrt{\frac{2}{3}} \left( \vec{r}_3 - \frac{1}{2} (\vec{r}_1 + \vec{r}_2) \right)$ . Generally,  $\vec{\eta}_k$  connects particle  $k+1$  with the center of mass of particles  $1, \dots, k$ . Then one may define a transformation matrix  $\underline{M}$  of dimension  $(N, N-1)$  as follows:

$$M_{i,j} = \begin{cases} -\sqrt{\frac{1}{j(j+1)}}, & i \leq j \\ \sqrt{\frac{j}{j+1}}, & i = j+1 \\ 0, & i > j+1 \end{cases} \quad (\text{A.2})$$

$$\begin{pmatrix} \vec{r}_1 - \vec{R}_{CM} \\ \vdots \\ \vec{r}_N - \vec{R}_{CM} \end{pmatrix} = \underline{M} \begin{pmatrix} \vec{\eta}_1 \\ \vdots \\ \vec{\eta}_{N-1} \end{pmatrix}, \quad \begin{pmatrix} \vec{\eta}_1 \\ \vdots \\ \vec{\eta}_{N-1} \end{pmatrix} = \underline{M}^T \begin{pmatrix} \vec{r}_1 \\ \vdots \\ \vec{r}_N \end{pmatrix} \quad (\text{A.3})$$

Notice that  $\underline{M}^T \underline{M} = \underline{1}_{N-1}$  but  $\underline{M} \underline{M}^T \neq \underline{1}_N$ . Any pairwise distance  $r_{i,j}$  can be written in terms of Jacobi vectors and does not depend on the center of mass. Indeed, letting  $\eta_{k,l}, l = 1, 2, 3$  be a Cartesian component of  $\vec{\eta}_k$ , then

$$r_{i,j}^2 = \sum_{l=1}^3 \left( \sum_{k=1}^{N-1} (M_{i,k} - M_{j,k}) \eta_{k,l} \right)^2. \quad (\text{A.4})$$

On the other hand, it became necessary to also construct a generalization of the H-type Jacobi tree in Ref. [100] (relevant for describing two dimers moving asymptotically far from each other) by the following alternate definitions of Jacobi vectors, only for  $N > 3$ :

$$\vec{\eta}_1 = \sqrt{\frac{1}{2}} (\vec{r}_2 - \vec{r}_1), \quad (\text{A.5})$$

$$\vec{\eta}_k = \sqrt{\frac{k-1}{k}} \left( \vec{r}_{k+2} - \frac{1}{k-1} \sum_{j=3}^{k+1} \vec{r}_j \right), \quad k = 2, \dots, N-2 \quad (\text{A.6})$$

$$\vec{\eta}_{N-1} = \sqrt{\frac{2(N-2)}{N}} \left( \left( \frac{1}{N-2} \sum_{j=3}^N \vec{r}_j \right) - \frac{1}{2} (\vec{r}_1 + \vec{r}_2) \right) \quad (\text{A.7})$$

For example, if  $N = 4$ , then  $\vec{\eta}_2 = \sqrt{\frac{1}{2}} (\vec{r}_4 - \vec{r}_3)$  and  $\vec{\eta}_3 = \frac{1}{2} (\vec{r}_3 + \vec{r}_4 - \vec{r}_1 - \vec{r}_2)$ . In words,  $\vec{\eta}_2, \dots, \vec{\eta}_{N-2}$  constitute a K-type Jacobi tree of the subsystem of particles 3 to  $N$ , while the last Jacobi vector gives the distances between the centers of mass of particles (1, 2) and (3, ...,  $N$ ).

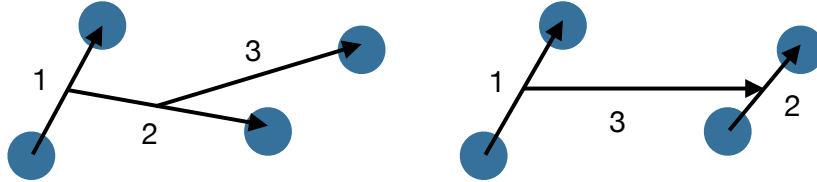


**Figure A.1.** Illustration of the K-type and H-type Jacobi trees for 4 particles.

For both Jacobi trees, the following can be proved by straightforward manipulation:

1.  $d^3\vec{r}_1 \cdots d^3\vec{r}_N = (N^{3/2} d^3\vec{R}_{CM}) d^3\vec{\eta}_1 \cdots d^3\vec{\eta}_{N-1}$
2.  $\sum_{i=1}^N \nabla_i^2 = \frac{1}{N} \nabla_{CM}^2 + \sum_{k=1}^{N-1} \nabla_{\eta_k}^2$
3.  $\sum_{k=1}^{N-1} \eta_k^2 = \sum_{i=1}^N r_i^2 - NR_{CM}^2 = \frac{1}{N} \sum_{i<j}^N r_{i,j}^2$

Hence, the 3 *CM* degrees of freedom may be unambiguously separated from a Hamiltonian of  $N$  bosons with pairwise interactions and a central trapping potential. Later, when we define the *hyperradius*  $\rho = \left( \frac{1}{N} \sum_{k=1}^{N-1} \eta_k^2 \right)^{1/2}$  as proportional to the radius of a hypersphere residing in a  $(3N - 3)$ -dimensional space of Jacobi vectors (the choice of  $\frac{1}{N}$  in the definition is mere convention), it is clear that the hyperradius is related to pairwise distances  $r_{i,j}$  and thus gives an overall size of the gaseous system. Finally, the hyperradius does not depend on the Jacobi tree, and the same set of  $3N - 4$  hyperangles may be used to describe the Jacobi vectors of either tree, conveniently resulting in the same functional form of the Laplacian.

## B. DELVES HYPERANGLES

Building on Appendix A, one may now move away from a Cartesian system by defining the hyperradius  $\rho = \left( \frac{1}{N} \sum_{k=1}^{N-1} \eta_k^2 \right)^{1/2}$ . What remains is to choose a particular set of  $3N - 4$  hyperangles  $\Omega$  that describe all possible configurations of Jacobi vectors, given fixed hyperradius.

Then in the Hamiltonian of  $N$  bosons, the trap term proportional to  $\sum_{k=1}^{N-1} \eta_k^2$  only depends on the hyperradius, while the Laplacian of Jacobi vectors must be of form

$$\begin{aligned} \sum_{k=1}^{N-1} \nabla_{\eta_k}^2 &= \frac{1}{N} \left[ \frac{1}{\rho^{3N-4}} \frac{\partial}{\partial \rho} \left( \rho^{3N-4} \frac{\partial}{\partial \rho} \right) - \frac{\Lambda^2}{\rho^2} \right] \\ &= \frac{1}{N} \left[ \frac{1}{\rho^{(3N-4)/2}} \frac{\partial^2}{\partial \rho^2} \left( \rho^{(3N-4)/2} \right) - \frac{(3N-4)(3N-6)}{4\rho^2} - \frac{\Lambda^2}{\rho^2} \right]. \end{aligned} \quad (\text{B.1})$$

The operator  $\Lambda^2$  is a “grand angular momentum operator”, operating on the  $3N - 4$  hyperangles with the eigenvalue equation  $\Lambda^2 Y_{\lambda,\mu}(\Omega) = \lambda(\lambda + 3N - 5) Y_{\lambda,\mu}(\Omega)$ . For  $N = 2$ , the eigenvalue equation reduces to the usual spherical harmonic differential equation. The functions  $Y_{\lambda,\mu}(\Omega)$  are called *hyperspherical harmonics* [101], forming a complete, orthonormal basis in a hypersphere of fixed hyperradius. They are identified by non-negative integer quantum number  $\lambda$  and a set of quantum numbers  $\mu$  that distinguish the different degenerate states. Indeed they are the adiabatic channel eigenfunctions of interest in this dissertation when the particles do not interact.

At a first glance, the simplest and most easily generalizable set of coordinates can be constructed by first considering the  $N - 1$  pair of spherical coordinates  $(\theta_i, \phi_i)$  for each Jacobi vector (of either K-type or H-type tree in Appendix A). Of course,  $\theta_i \in [0, \pi]$  and  $\phi_i \in [0, 2\pi]$ , with definition  $\tan \theta_i = \sqrt{\eta_{i,x}^2 + \eta_{i,y}^2} / \eta_{i,z}$  and  $\tan \phi_i = \eta_{i,y} / \eta_{i,x}$ . Then the remaining  $N - 2$  hyperangles  $\beta_i \in [0, \frac{\pi}{2}]$  are defined from the norms  $\eta_i$  of Jacobi vectors as follows:

$$\begin{aligned}
\eta_1 &= \sqrt{N}\rho \cos \beta_1, \\
\eta_2 &= \sqrt{N}\rho \sin \beta_1 \cos \beta_2, \\
&\vdots \\
\eta_{N-2} &= \sqrt{N}\rho \sin \beta_1 \cdots \sin \beta_{N-3} \cos \beta_{N-2}, \\
\eta_{N-1} &= \sqrt{N}\rho \sin \beta_1 \cdots \sin \beta_{N-3} \sin \beta_{N-2}.
\end{aligned} \tag{B.2}$$

Hyperangles of such construction were first introduced by Delves [102]–[104], and their utility lies in formal simplicity and ease of generalization for  $N$  particles. It follows that the grand angular momentum operator for  $N > 2$  takes the following form:

$$\Lambda^2 = - \sum_{l=1}^{N-2} \left[ C_l \left( \frac{1}{\cos^2 \beta_l \sin^{3N-4-3l} \beta_l} \right) \frac{\partial}{\partial \beta_l} \left( \cos^2 \beta_l \sin^{3N-4-3l} \beta_l \frac{\partial}{\partial \beta_l} \right) \right] + \sum_{k=1}^{N-1} \left[ \frac{L_k^2}{x_k^2} \right], \tag{B.3}$$

$$C_l = \begin{cases} 1, & l = 1 \\ \prod_{k=1}^{l-1} \sin^{-2} \beta_k, & l > 1 \end{cases} \tag{B.4}$$

$$L_k^2 = - \frac{1}{\sin \theta_k} \frac{\partial}{\partial \theta_k} \left( \sin \theta_k \frac{\partial}{\partial \theta_k} \right) - \frac{1}{\sin^2 \theta_k} \frac{\partial^2}{\partial \phi_k^2}, \tag{B.5}$$

$$x_k = \frac{\eta_k}{\sqrt{N}\rho}. \tag{B.6}$$

Furthermore, the differentials are:

$$d^3 \vec{\eta}_1 \cdots d^3 \vec{\eta}_{N-1} = \left( N^{(3N-3)/2} \rho^{3N-4} d\rho \right) d\Omega, \tag{B.7}$$

$$d\Omega = \left( \prod_{k=1}^{N-2} \cos^2 \beta_k \sin^{3N-4-3k} \beta_k d\beta_k \right) \left( \prod_{l=1}^{N-1} \sin \theta_l d\theta_l d\phi_l \right), \tag{B.8}$$

and total hyperangular volume  $\Omega = \int d\Omega = 4 \left( \pi^{(3N-4)/2} \right) \Gamma \left( \frac{3}{2} \right) / \Gamma \left( \frac{3}{2}(N-1) \right)$ .

## C. SMITH-WHITTEN HYPERANGLES

### C.1 Three Particles

Though the Delves hyperangles, introduced in Appendix B, are easy to construct for a general number of particles, they are often not the most convenient set of hyperangles to do numerical computation with. For instance, certain three-body works [73], [85], [86] make use of a different coordinate system, called the Smith-Whitten hyperangles [105]–[109], where the 5 hyperangles are separated into 3 *external* Euler angles and 2 *internal* hyperangles.

Recall first a conventional definition of Euler angles  $(\alpha, \beta, \gamma)$  [110], [111]; one may rotate using these angles to go from lab-frame axes  $(\hat{x}, \hat{y}, \hat{z})$  to rotating body-frame axes  $(\hat{e}_1, \hat{e}_2, \hat{e}_3)$ .

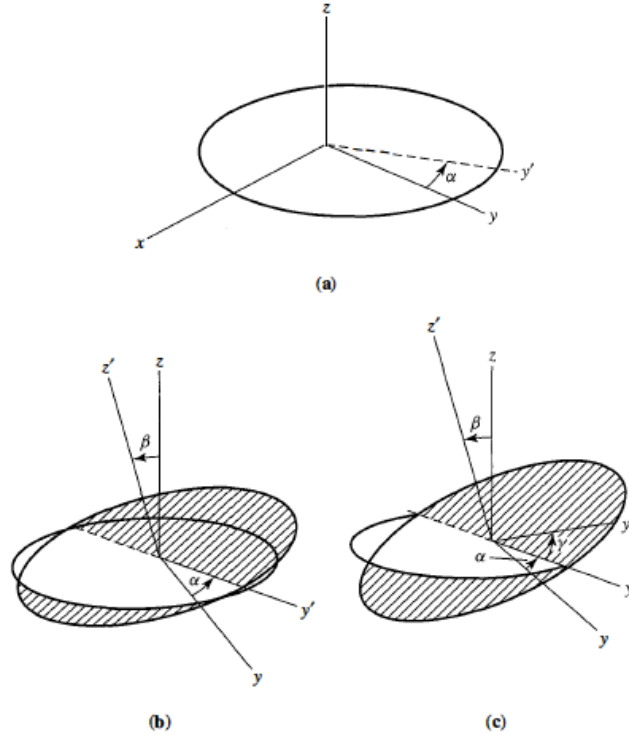


**Figure C.1.** Illustration of the Euler angles  $(\alpha, \beta, \gamma)$ . Taken from Figure 3.4 of Ref. [110].

The range of angles  $\alpha$  and  $\gamma$  is  $[0, 2\pi]$ , while the range of  $\beta$  is  $[0, \pi]$ . Note now that at any instant in time, there exists a plane on which three bodies reside. Define a vector  $\vec{A} = \frac{\sqrt{3}}{2}(\vec{\eta}_1 \times \vec{\eta}_2)$ , with K-type Jacobi vectors described in Appendix A. The norm of  $\vec{A}$  is equal to the area of triangle spanned by the three bodies; define the body-frame so that  $\hat{e}_3$  and  $\vec{A}$  point in the same direction (this defines the Euler angles  $\alpha$  and  $\beta$ ).

We follow Ref. [107] and define  $\gamma$  so that in the body-frame ( $\hat{e}_1, \hat{e}_2, \hat{e}_3$ ), the moment-of-inertia tensor component  $I_{x,y}$  is 0; also, we choose which is  $\hat{e}_1$  and which is  $\hat{e}_2$  by choosing to have  $I_{y,y} \geq I_{x,x}$ . Then in the body-frame, the components of Jacobi vectors are defined as follows with two internal hyperangles  $\theta$  and  $\phi$ :

$$\begin{aligned}\eta_{1,x} &= \sqrt{3}\rho \cos \theta \cos \phi, \\ \eta_{1,y} &= -\sqrt{3}\rho \sin \theta \sin \phi, \\ \eta_{2,x} &= \sqrt{3}\rho \cos \theta \sin \phi, \\ \eta_{2,y} &= \sqrt{3}\rho \sin \theta \cos \phi.\end{aligned}\tag{C.1}$$

When  $\theta = 0$ , all 3 particles lie on the same line; when  $\theta = \frac{\pi}{4}$ , the 3 particles form an equilateral triangle. Because the norm of vector  $\vec{A}$  is proportional to  $\sin 2\theta$ , the range of  $\theta$  is restricted to  $[0, \frac{\pi}{4}]$ . As for the range of  $\phi$ , letting it take the full range of  $[0, 2\pi]$  causes an ambiguity that a transformation  $\gamma \rightarrow \gamma + \pi$ ,  $\phi \rightarrow \phi + \pi$  leads to the same particle configuration; we now choose ranges  $\phi \in [0, 2\pi]$  and  $\gamma \in [0, \pi]$ .

Most importantly, the two-body distances are now expressed solely in terms of the internal hyperangles, regardless of the frame of reference:

$$\begin{aligned}r_{1,2} &= \sqrt{3}\rho \sqrt{1 + \cos(2\theta) \cos(2\phi)}, \\ r_{1,3} &= \sqrt{3}\rho \sqrt{1 + \cos(2\theta) \cos\left(2\phi - \frac{2\pi}{3}\right)}, \\ r_{2,3} &= \sqrt{3}\rho \sqrt{1 + \cos(2\theta) \cos\left(2\phi + \frac{2\pi}{3}\right)}.\end{aligned}\tag{C.2}$$

Also,  $d\Omega = (\sin 4\theta d\theta d\phi)(\frac{1}{4} \sin \beta d\alpha d\beta d\gamma)$ , and  $\Omega = \int d\Omega = \pi^3$ .

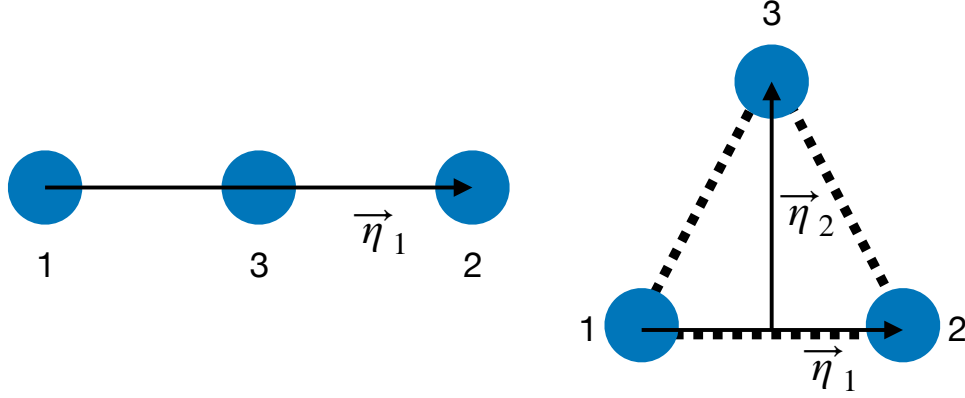


**Figure C.2.** Illustration of Smith-Whitten coordinates  $(\theta, \phi) = (0, 0)$  and  $(\frac{\pi}{4}, 0)$ .

Next, consider the total angular momentum  $\vec{J} = -i\vec{\eta}_1 \times \vec{\nabla}_{\eta_1} - i\vec{\eta}_2 \times \vec{\nabla}_{\eta_2}$ . In body-frame, the components of  $\vec{J} = J_x \hat{e}_1 + J_y \hat{e}_2 + J_z \hat{e}_3$  are given by [109]:

$$\begin{aligned} J_x &= -i \left[ -\frac{\cos \gamma}{\sin \beta} \frac{\partial}{\partial \alpha} + \sin \gamma \frac{\partial}{\partial \beta} + \frac{\cos \gamma}{\tan \beta} \frac{\partial}{\partial \gamma} \right], \\ J_y &= -i \left[ \frac{\sin \gamma}{\sin \beta} \frac{\partial}{\partial \alpha} + \cos \gamma \frac{\partial}{\partial \beta} - \frac{\sin \gamma}{\tan \beta} \frac{\partial}{\partial \gamma} \right], \\ J_z &= -i \frac{\partial}{\partial \gamma}. \end{aligned} \quad (\text{C.3})$$

Finally, the grand angular momentum operator  $\Lambda^2$  takes the following form with Smith-Whitten coordinates:

$$\Lambda^2 = -\frac{1}{\sin 4\theta} \frac{\partial}{\partial \theta} \left( \sin 4\theta \frac{\partial}{\partial \theta} \right) - \frac{1}{\cos^2 2\theta} \left( \frac{\partial}{\partial \phi} + i \sin 2\theta J_z \right)^2 + \frac{J_x^2}{\sin^2 \theta} + \frac{J_y^2}{\cos^2 \theta} + J_z^2. \quad (\text{C.4})$$

Then by expansion in terms of Wigner D-functions, the fixed-hyperradius adiabatic Schrödinger's equation becomes a two-dimensional coupled partial differential equation in

terms of  $\theta$  and  $\phi$ . For total  $J^\pi = 0^+$  of interest in this dissertation, with *ansatz* functions only dependent on two-body distances  $r_{i,j}$ , the Euler angles are ultimately irrelevant, and hence one may take  $\Lambda^2 = -\frac{1}{\sin 4\theta} \frac{\partial}{\partial \theta} \left( \sin 4\theta \frac{\partial}{\partial \theta} \right) - \frac{1}{\cos^2 2\theta} \frac{\partial^2}{\partial \phi^2}$ .

## C.2 More than Three Particles

Unfortunately, the Smith-Whitten coordinate system discussed above is specialized for  $N = 3$  with no obvious means to generalize for more particles. For 4 particles, there exists a scheme to again separate out the 3 Euler angles and deal with 5 internal hyperangles [112], but that is not of interest here. Among  $N > 3$  particles, only the Euler angles of particles 1 to 3, described by K-type Jacobi vectors  $\vec{\eta}_1$  and  $\vec{\eta}_2$  in Appendix A, shall be considered in this work.

To do so, introduce a new hyperangle  $\delta \in [0, \frac{\pi}{2}]$ , defined by the relations  $\eta_1^2 + \eta_2^2 = N\rho^2 \sin^2 \delta$  and  $\eta_3^2 + \dots + \eta_{N-1}^2 = N\rho^2 \cos^2 \delta$ . Once again, with the body-frame of particles 1, 2, and 3 defined the same as above, now define the components of Jacobi vectors  $\vec{\eta}_1$  and  $\vec{\eta}_2$  in that body-frame as follows:

$$\begin{aligned}
\eta_{1,x} &= \sqrt{N}\rho \sin \delta \cos \theta \cos \phi, \\
\eta_{1,y} &= -\sqrt{N}\rho \sin \delta \sin \theta \sin \phi, \\
\eta_{2,x} &= \sqrt{N}\rho \sin \delta \cos \theta \sin \phi, \\
\eta_{2,y} &= \sqrt{N}\rho \sin \delta \sin \theta \cos \phi.
\end{aligned} \tag{C.5}$$

The only crucial difference from the definitions of Equations C.1 is the introduction of  $\sin \delta$ . As for the remaining Jacobi vectors  $\vec{\eta}_3, \dots, \vec{\eta}_{N-1}$ , define their own hyperangles in the manner of Delves as described in Appendix B. More specifically, if  $N = 4$ , then there are additional two spherical angles  $(\theta_3, \phi_3)$  for  $\vec{\eta}_3$ , while norm  $\eta_3 = \sqrt{4}\rho \cos \delta$ . If  $N > 4$ , there are  $N - 3$  pairs of spherical angles  $(\theta_3, \phi_3), \dots, (\theta_{N-1}, \phi_{N-1})$ , while the norms of Jacobi vectors are related as follows:

$$\begin{aligned}
\eta_3 &= (\sqrt{N}\rho \cos \delta) \cos \beta_3, \\
\eta_4 &= (\sqrt{N}\rho \cos \delta) \sin \beta_3 \cos \beta_4, \\
&\vdots \\
\eta_{N-2} &= (\sqrt{N}\rho \cos \delta) \sin \beta_3 \cdots \sin \beta_{N-3} \cos \beta_{N-2}, \\
\eta_{N-1} &= (\sqrt{N}\rho \cos \delta) \sin \beta_3 \cdots \sin \beta_{N-3} \sin \beta_{N-2}.
\end{aligned} \tag{C.6}$$

The differential volume element takes the following form:

$$\begin{aligned}
d\Omega &= (\sin^5 \delta \cos^{3N-10} \delta d\delta) (\sin 4\theta d\theta d\phi) \left( \frac{1}{4} \sin \beta d\alpha d\beta d\gamma \right) \\
&\times \left[ \prod_{k=3}^{N-2} \cos^2 \beta_k \sin^{3N-3k-4} \beta_k d\beta_k \right] \times \left[ \prod_{l=3}^{N-1} \sin \theta_l d\theta_l d\phi_l \right].
\end{aligned} \tag{C.7}$$

If  $N = 4$ ,  $\beta_k$  is not defined so replace the terms involving  $\beta_k$  by 1 in Eqn. C.7. Integrating over the various terms in  $d\Omega$  except  $(\delta, \theta, \phi)$  gives  $4 \left( \pi^{(3N-6)/2} \right) \Gamma \left( \frac{3}{2} \right) / \Gamma \left( \frac{3}{2}(N-3) \right)$ .

Most importantly, the two-body distances amongst particles 1, 2, and 3 only depend on *three* hyperangles, similar to Eqn. C.2 for  $N = 3$  but with  $\sin \delta$  inserted:

$$\begin{aligned}
r_{1,2} &= \sqrt{N}\rho \sin \delta \sqrt{1 + \cos(2\theta) \cos(2\phi)}, \\
r_{1,3} &= \sqrt{N}\rho \sin \delta \sqrt{1 + \cos(2\theta) \cos\left(2\phi - \frac{2\pi}{3}\right)}, \\
r_{2,3} &= \sqrt{N}\rho \sin \delta \sqrt{1 + \cos(2\theta) \cos\left(2\phi + \frac{2\pi}{3}\right)}.
\end{aligned} \tag{C.8}$$

Finally, though the full form of grand angular momentum operator is more complicated, because this dissertation is concerned with functions depending only on  $(\delta, \theta, \phi)$ , one may take the operator to *effectively* be as follows:

$$\begin{aligned}
\Lambda^2 = & - \left( \frac{1}{\sin^5 \delta \cos^{3N-10} \delta} \right) \frac{\partial}{\partial \delta} \left( \sin^5 \delta \cos^{3N-10} \delta \frac{\partial}{\partial \delta} \right) \\
& + \frac{1}{\sin^2 \delta} \left[ - \frac{1}{\sin 4\theta} \frac{\partial}{\partial \theta} \left( \sin 4\theta \frac{\partial}{\partial \theta} \right) - \frac{1}{\cos^2 2\theta} \frac{\partial^2}{\partial \phi^2} \right].
\end{aligned} \tag{C.9}$$

## D. THREE-BODY HYPERSPHERICAL HARMONICS

In Section 4.2.2, functions  $Y_n(\Omega)$  (see Equation 4.16) are shown to be some, but not all, of the symmetrized hyperspherical harmonics of symmetry  $J^\pi = 0^+$ , governing the physics of  $N$  non-interacting bosons. Here we explicitly compute some of the symmetrized hyperspherical harmonics for  $N = 3$  and compare with  $Y_n$  for pedagogic purposes.

It is helpful to recall again the expressions for two-body distances in terms of Smith-Whitten hyperangles (see Appendix C):

$$\begin{aligned} r_{1,2} &= \sqrt{3}\rho\sqrt{1 + \cos(2\theta)\cos(2\phi)}, \\ r_{1,3} &= \sqrt{3}\rho\sqrt{1 + \cos(2\theta)\cos\left(2\phi - \frac{2\pi}{3}\right)}, \\ r_{2,3} &= \sqrt{3}\rho\sqrt{1 + \cos(2\theta)\cos\left(2\phi + \frac{2\pi}{3}\right)}. \end{aligned} \tag{D.1}$$

For  $N = 3$ , the functions  $Y_n$  take the following form:

$$\begin{aligned} Y_n(\Omega) &= \sum_{i < j}^3 P_n^{(\frac{1}{2}, \frac{1}{2})} \left( \frac{r_{i,j}^2}{3\rho^2} - 1 \right) \\ &= P_n^{(\frac{1}{2}, \frac{1}{2})} \left( \cos(2\theta)\cos(2\phi) \right) + P_n^{(\frac{1}{2}, \frac{1}{2})} \left( \cos(2\theta)\cos\left(2\phi - \frac{2\pi}{3}\right) \right) \\ &\quad + P_n^{(\frac{1}{2}, \frac{1}{2})} \left( \cos(2\theta)\cos\left(2\phi + \frac{2\pi}{3}\right) \right). \end{aligned} \tag{D.2}$$

On the other hand, for symmetry  $J^\pi = 0^+$ , as explained in Appendix C, the Euler angles are irrelevant and only two hyperangles  $(\theta, \phi)$  must be considered. Then the hyperspherical harmonic eigenvalue equation becomes:

$$\begin{aligned} \Lambda^2 Y_{\nu,\mu}(\Omega) &= \left[ -\frac{1}{\sin 4\theta} \frac{\partial}{\partial \theta} \left( \sin 4\theta \frac{\partial}{\partial \theta} \right) - \frac{1}{\cos^2 2\theta} \frac{\partial^2}{\partial \phi^2} \right] Y_{\nu,\mu}(\Omega) \\ &= \nu(\nu + 4) Y_{\nu,\mu}(\Omega). \end{aligned} \tag{D.3}$$

It was noted in Appendix C that a coordinate transformation  $\gamma \rightarrow \gamma + \pi$ ,  $\phi \rightarrow \phi + \pi$  leads to the same particle configuration; because the functions of interest here do not depend on  $\gamma$ , one must impose a periodic boundary condition as  $\phi \rightarrow \phi + \pi$ . After also imposing regularity as  $\theta \rightarrow 0$  and  $\theta \rightarrow \frac{\pi}{4}$ , the hyperspherical harmonics *before* symmetrization are (disregard normalization):

$$Y_\nu^{n,m}(\Omega) = \cos^{|m|}(2\theta) P_n^{(0,|m|)}(\cos 4\theta) \exp(2im\phi). \quad (\text{D.4})$$

The eigenvalue is given by  $\nu = 4n + 2|m|$ , with  $n = 0, 1, \dots$  and  $m$  any integer.

Next, it can be shown by straightforward algebra [105] that to fully symmetrize  $Y_\nu^{n,m}$ , one need only generate and add up 6 terms, each with  $\phi$  replaced by one of the following:  $(\phi, -\phi, \frac{2\pi}{3} - \phi, -\frac{2\pi}{3} - \phi, \phi - \frac{2\pi}{3}, \phi + \frac{2\pi}{3})$ . Positive and negative  $m$  give the same symmetrized functions, so only treat  $m \geq 0$ . Also,  $m$  must be a multiple of 3 or the symmetrized function becomes 0.

The following table summarizes, up to  $\nu = 12$ , each possible pairs  $(n, m)$  and their corresponding symmetrized functions (normalization ignored):

$\nu$	$(n, m)$	$Y_\nu^{n,m}$
0	(0,0)	1
2	n.a.	0
4	(1,0)	$\cos 4\theta$
6	(0,3)	$\cos^3 2\theta \cos 6\phi$
8	(2,0)	$3 \cos^2 4\theta - 1$
10	(1,3)	$\cos^3 2\theta (5 \cos 4\theta - 3) \cos 6\phi$
12	(3,0)	$5 \cos^3 4\theta - 3 \cos 4\theta$
	(0,6)	$\cos^6 2\theta \cos 12\phi$

**Table D.1.** Summary of Symmetrized Hyperspherical Harmonics for  $N = 3$ ,  $J^\pi = 0^+$ .

Notice that to have  $\nu = 2$ ,  $(n, m)$  must be  $(0, 1)$ , which gives symmetrized  $Y_\nu^{n,m} = 0$ , proving that  $\nu = 2$  really is forbidden for  $N = 3$ ,  $J^\pi = 0^+$  [74]. Up to  $\nu = 10$ , there is no degeneracy, and each symmetrized  $Y_\nu^{n,m}$  is the same as corresponding  $Y_n$  of Eqn. D.2 up to a constant. The first degeneracy occurs for  $\nu = 12$ . The function  $Y_6$  of Section 4.2.2, given by Eqn. D.2, is one of two linear combinations of  $Y_{12}^{3,0}$  and  $Y_{12}^{0,6}$ .

## E. EVALUATION OF TWO-BODY ANSATZ

In Section 4.2.3, an explicitly constructed two-body ansatz function  $\phi_\nu(r_{1,2})$  was introduced in Equation 4.20, as well as a defining equation for parameter  $\nu$  (Eqn. 4.22), which both use a Gauss hypergeometric function  ${}_2F_1$ . This appendix gives more details on evaluating a hypergeometric function, as well as information regarding hyperangular and hyperradial derivatives of  $\phi_\nu(r_{1,2})$ . Ref. [90] gives a more complete background on the general theory and applications of hypergeometric functions.

We are concerned with functions  ${}_2F_1(a, b, c, z)$ , where  $0 \leq z \leq 1$ ,  $c > 0$ , and  $(a, b)$  are either real or complex conjugates so that  $a + b$  and  $ab$  are real. The Gauss power series is defined for  $|z| < 1$ :

$${}_2F_1(a, b, c, z) = \sum_{n=0}^{\infty} \frac{(a)_n (b)_n}{(c)_n n!} z^n = 1 + \frac{ab}{c} z + \frac{a(a+1)b(b+1)}{c(c+1)2!} z^2 + \dots \quad (\text{E.1})$$

The series converges on the closed disk  $|z| \leq 1$  when  $c - a - b > 0$ , converges on the open disk  $|z| < 1$  when  $-1 < c - a - b \leq 0$ , and diverges when  $c - a - b \leq -1$ . Whenever a hypergeometric function appears, we apply various known transformations (see [90]) so that not only  $c - a - b > 0$  to ensure convergence of power series, but also  $z \leq \frac{1}{2}$  so that the power series converges quickly and can be easily implemented numerically. Each term of the power series is computed and added cumulatively until desired convergence criterion is met.

For example, when  $c > a + b$ , the following transformation may be used when  $z > \frac{1}{2}$  to speed convergence, depending on the value of  $c$ :

$$\begin{aligned} c < 1 : F(a, b, c, z) &= \frac{\Gamma(c)\Gamma(c-a-b)}{\Gamma(c-a)\Gamma(c-b)} F(a, b, a+b-c+1, 1-z) \\ &+ (1-z)^{c-a-b} \frac{\Gamma(c)\Gamma(a+b-c)}{\Gamma(a)\Gamma(b)} F(c-a, c-b, c-a-b+1, 1-z), \end{aligned} \quad (\text{E.2})$$

$$c \geq 1 : F(a, b, c, z) = \frac{1}{z^{c-1}} \left[ \frac{\Gamma(c)\Gamma(c-a-b)}{\Gamma(c-a)\Gamma(c-b)} F(a-c+1, b-c+1, a+b-c+1, 1-z) \right. \\ \left. + (1-z)^{c-a-b} \frac{\Gamma(c)\Gamma(a+b-c)}{\Gamma(a)\Gamma(b)} F(1-a, 1-b, c-a-b+1, 1-z) \right]. \quad (\text{E.3})$$

Now, in Eqn. 4.20 for the ansatz  $\phi_\nu(r_{i,j})$  defined piecewise, the function  $f_1$  is a hypergeometric function with argument  $z = 1 - x_{i,j}^2 = 1 - \frac{r_{i,j}^2}{2N\rho^2}$ . When  $(i, j) = (1, 2)$ , then  $x_{1,2} = \frac{r_{1,2}}{\sqrt{2N\rho}} = \cos \beta_1$ , depending on only one Delves hyperangle. But for other particle pairs,  $x_{i,j} = \frac{r_{i,j}}{\sqrt{2N\rho}}$  ranges from 0 to 1 and is a more complicated combination of various hyperangles. At any rate, if  $\alpha$  is one of  $3N - 4$  hyperangles  $\Omega$ , one computes the hyperangular derivative of  $\phi_\nu$  as follows (omit indices  $i, j$  in  $r$  and  $x$  for clarity):

$$\frac{\partial \phi_\nu}{\partial \alpha} = \frac{\partial x}{\partial \alpha} \frac{\partial \phi_\nu}{\partial x} = \begin{cases} \frac{\sqrt{2N\rho}}{C_m} \left( \frac{\partial x}{\partial \alpha} \right) \frac{d}{dr} \left( \frac{u(r)}{r} \right), & r \leq r_c \\ \left( \frac{\partial x}{\partial \alpha} \right) \frac{\partial f_1}{\partial x}, & r > r_c \end{cases} \quad (\text{E.4})$$

$$\frac{\partial f_1}{\partial x} = \frac{1}{x^2} \left( \frac{\nu(\nu + 3N - 5)}{3N - 6} \right) F \left( \frac{-\nu - 1}{2}, \frac{\nu + 3N - 6}{2}, \frac{3N - 4}{2}, 1 - x^2 \right). \quad (\text{E.5})$$

Recall that matching coefficient  $C_m$  and parameter  $\nu$  only depend on  $\rho$ . The term  $\frac{\partial x_{i,j}}{\partial \alpha}$  can be treated separately on a case-by-case basis, while  $\frac{d}{dr} \left( \frac{u(r)}{r} \right)$  and  $\frac{\partial f_1}{\partial x_{i,j}}$  are computed straightforwardly.

One must also compute the *hyperradial* derivative of  $\phi_\nu$  in order to compute the diagonal non-adiabatic correction  $Q$ . This time,  $x_{i,j}$  in  $f_1$  is treated as constant, while one must consider the hyperradial derivatives of  $C_m(\rho)$  and  $\epsilon(\rho) = (\tilde{\nu}(\rho))^2$ , which are estimated by differentiating a cubic-spline interpolation formula [113].  $\tilde{\nu} = \nu + \frac{3N-5}{2}$  is either positive real or purely imaginary  $iy, y \geq 0$ .  $\epsilon$  is always real and more appropriate for differentiation than  $\nu$ . Then one treats the hyperradial derivative of  $\phi_\nu$  as follows:

$$\frac{\partial \phi_\nu}{\partial \rho} = \begin{cases} -\frac{C'_m(\rho)}{(C_m(\rho))^2} \left( \frac{u(r)}{r} \right) + \frac{1}{C_m(\rho)} \left( \frac{r}{\rho} \right) \frac{d}{dr} \left( \frac{u(r)}{r} \right), & r \leq r_c \\ \frac{\partial f_1}{\partial \rho}, & r > r_c \end{cases} \quad (\text{E.6})$$

When  $1 - x^2 \leq \frac{1}{2}$ , the function  $\frac{\partial f_1}{\partial \rho}$  can be written as follows:

$$\begin{aligned}\frac{\partial f_1}{\partial \rho} &= \frac{\epsilon'(\rho)}{x} \frac{\partial}{\partial \epsilon} \left[ F \left( -\frac{\tilde{\nu}}{2} + \frac{3N-7}{4}, \frac{\tilde{\nu}}{2} + \frac{3N-7}{4}, \frac{3N-6}{2}, 1-x^2 \right) \right] \\ &= -\frac{\epsilon'(\rho)}{4x} \tilde{F} \left( -\frac{\tilde{\nu}}{2} + \frac{3N-7}{4}, \frac{\tilde{\nu}}{2} + \frac{3N-7}{4}, \frac{3N-6}{2}, 1-x^2 \right),\end{aligned}\quad (\text{E.7})$$

$$\tilde{F}(a, b, c, z) = \frac{1}{a-b} \left( \frac{\partial}{\partial b} - \frac{\partial}{\partial a} \right) F(a, b, c, z). \quad (\text{E.8})$$

$\tilde{F}(a, b, c, z)$  is a newly defined function for the purposes here, symmetric under the exchange of  $a$  and  $b$ . Evaluate the following power series, well-defined when  $c > a + b$  and original  $F(a, b, c, z)$  has convergent power series:

$$\tilde{F}(a, b, c, z) = \sum_{n=1}^{\infty} \left[ \sum_{l=0}^{n-1} \frac{1}{(a+l)(b+l)} \right] \frac{(a)_n (b)_n}{(c)_n n!} z^n. \quad (\text{E.9})$$

When  $1 - x^2 > \frac{1}{2}$ , above expression for  $\frac{\partial f_1}{\partial \rho}$  is not desirable because the power series of  $\tilde{F}(a, b, c, z)$  converges slowly. In that case, begin with the original expression for  $f_1$  in Eqn. 4.13, transform it using either Eqn. E.2 or E.3, differentiate with respect to  $\epsilon$ , then put appropriate terms together in terms of functions  $F$  and  $\tilde{F}$ , now with  $z = x^2$  so that the power series of  $F$  and  $\tilde{F}$  converge quickly.

## VITA

Hyunwoo Lee

Ph.D. Physics, Purdue University, December 2021

B.S. Physics and Mathematics, The University of Texas at Austin, May 2015

Publications:

*(Undecided title on materials of Chapters 4 and 5, to be published soon)*

Orbital variational adiabatic hyperspherical method applied to Bose-Einstein condensates

Hyunwoo Lee and Chris H. Greene

Phys. Rev. A **103**, 023325 (2021)

Anisotropic blockade using pendular long-range Rydberg molecules

Matthew T. Eiles, Hyunwoo Lee, Jesús Pérez-Ríos, and Chris H. Greene

Phys. Rev. A **95**, 052708 (2017)

Stabilization of the Simplest Criegee Intermediate from the Reaction between Ozone and Ethylene: A High-Level Quantum Chemical and Kinetic Analysis of Ozonolysis

Thanh Lam Nguyen, Hyunwoo Lee, Devin A. Matthews, Michael C. McCarthy, and John F. Stanton

J. Phys. Chem. A **119**, 5524 (2015)

High-Accuracy Estimates for the Vinylidene-Acetylene Isomerization Energy and the Ground State Rotational Constants of :C=CH<sub>2</sub>

Hyunwoo Lee, Joshua H. Baraban, Robert W. Field, and John F. Stanton

J. Phys. Chem. A **117**, 11679 (2013)

Contributed Talks and Posters:

Variational Adiabatic Hyperspherical Treatment of Bose-Einstein Condensates

APS Division of Atomic, Molecular and Optical Physics 2021

An Improved Many-Body Ansatz for a Hypervectorial Description of Bose-Einstein Condensates

APS Division of Atomic, Molecular and Optical Physics 2020

Adiabatic Theory of Three Bosons under Transverse Confinement using Hypervectorial Coordinates

APS Division of Atomic, Molecular and Optical Physics 2019

Details and Observables of Three-Dimensional Scattering between Two Rydberg Polaritons

APS Division of Atomic, Molecular and Optical Physics 2018